Chapter 10
Carbon-Based Field Emitters: Properties and Applications

Nikolay V. Egorov and Evgeny P. Sheshin

Abstract Field emission is one of the most promising areas of vacuum nano- and microelectronics. This chapter reviews current achievements and problems in studying carbon-based field emitters. It is a detailed elaboration of topics partly addressed in the authors' textbook "Field Emission Electronics". The review is multipartite. The first part gives general information about carbon-based materials, describing their structures, manufacturing methods for field emission cathodes, and basic features. The second part considers and analyzes some special modern electron emission theory that applies to field emission from carbon-based materials. This is followed by results on the field emission properties of different forms of carbon-based materials. The last part features applications and technological devices using carbon-based field emission cathodes, including descriptions of devices and their design, and prospects for further development. Here, the authors pay particular attention to their own papers on these topics.

10.1 Introduction: General Information on Carbon-Based Materials

Development of stable field electron emission (FE) cathodes is one of the most pressing problems of today's electronics. Such cathodes have many advantages in comparison with other kinds of free-electron emitters: thermal stability, exponential slope of current–voltage characteristics, low sensitivity to external radiation, etc. The materials used to manufacture FE cathodes have been diverse, including (a) refractory metals such as tungsten, molybdenum, rhenium, and platinum, (b) transition metals such as chromium, niobium, and hafnium, and (c) semiconductor materials. However,

---

N. V. Egorov (✉)
Saint Petersburg State University, St. Petersburg, Russia
e-mail: n.v.egorov@spbu.ru

E. P. Sheshin
Moscow Institute of Physics and Technology, Dolgoprudny, Russia
e-mail: sheshin.ep@mipt.ru

G. Gaertner et al. (eds.), *Modern Developments in Vacuum Electron Sources*,
Topics in Applied Physics 135, https://doi.org/10.1007/978-3-030-47291-7_10

the materials for FE cathodes also need to have specific properties, such as low and stable electronic work-function values, and high values of mechanical robustness and of electrical and thermal conductivity [1, 2]. Soon after the first reports on FE from carbon-based materials appeared in the early 1970s, their advantages became quite obvious. This article considers the most popular and well-known carbon-based materials used in FE cathodes.

The great variety of carbon-based materials includes many able to function as FE cathodes. A classification of such materials is shown in Fig. 10.1.

Three different combinations of σ- and π-bonds result in three electronic states for carbon atoms: (i) sp^3 hybridization with a tetrahedral arrangement of four σ-bonds, established as a result of interaction between one s-electron and three p-electrons (this corresponds to the ideal diamond structure); (ii) sp^2 hybridization characterized by three σ-bonds, and a π-bond that is localized in the plane perpendicular to the σ-bonds (this state corresponds to the graphite structure); and (iii) sp^2 hybridization with two σ-bonds and two π-bonds (this corresponds to the so-called carbine structure, with linear polymeric chains of type "—C = C—C = C—" or type " = C = C = C = ").

Research and quantitative assessment of the distribution of these bonds can be quite fruitful when studying the origins of the properties of different carbon-based materials.

In the sp^2 hybridization state, carbon atoms form layered structures. A layer (base-plane) consists of a continuous series of regular hexagons with carbon atoms

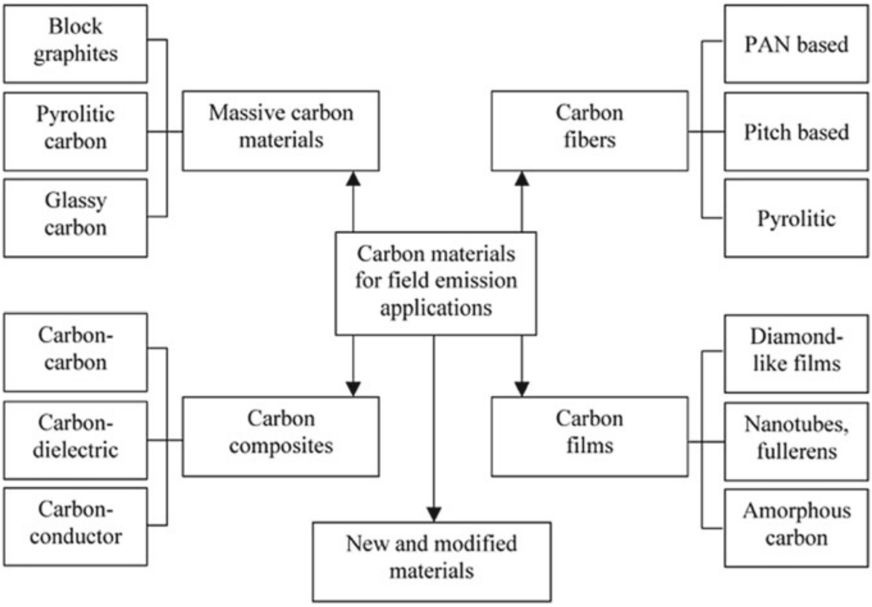

Fig. 10.1 Classification of the types of carbon material that are of interest in the production of field emission cathodes (compare [3])

at the vertices. The shortest distance between the atoms in the plane is equal to the hexagon side and amounts to 1.417 Å. Graphite consists of a continuous series of layers parallel to the base-plane. The carbon atoms in this layer are connected with three σ-bonds of equal value. Additional bonds are established by π-electrons with somewhat overlapping orbitals. Collectivization of π-electrons in the graphite layer gives a metallic nature to its electrical and optical properties. Different sources range the binding energy between the carbon atoms in the plane from 340 to 420 kJ/mol (3.5 to 4.4 eV), while the binding energy between the layers does not exceed 42 to 84 kJ/mol (0.44 to 0.87 eV) (see [4]).

The sequence pattern defines the type of ideal crystal lattice of graphite, i.e., hexagonal or rhombohedral (Fig. 10.2).

When the layers alternate ab, ab, ab, carbon atoms in each layer settle down only over the centers of regular hexagons in the next layer. This is a hexagonal structure with four carbon atoms in a unit cell. The interlayer distance in ideal graphite is 3.354 Å. The unit cell of a graphite hexagonal structure is a right-angle prism with a regular rhombus in its base.

The abc, abc layer sequence results in a rhombohedral lattice of graphite. Unlike the hexagonal one, it is three-layered. At temperatures above 2000 °C, the rhombohedral packing turns into the hexagonal one. Both structures of ideal graphite should be considered as infinite grids of hexagons located in parallel layers. In practical terms, these grids are finite in man-made graphites.

Real graphites differ from ideal structures by having different defects. Failures in the sequence of layers cause packing defects. A large number of such defects result

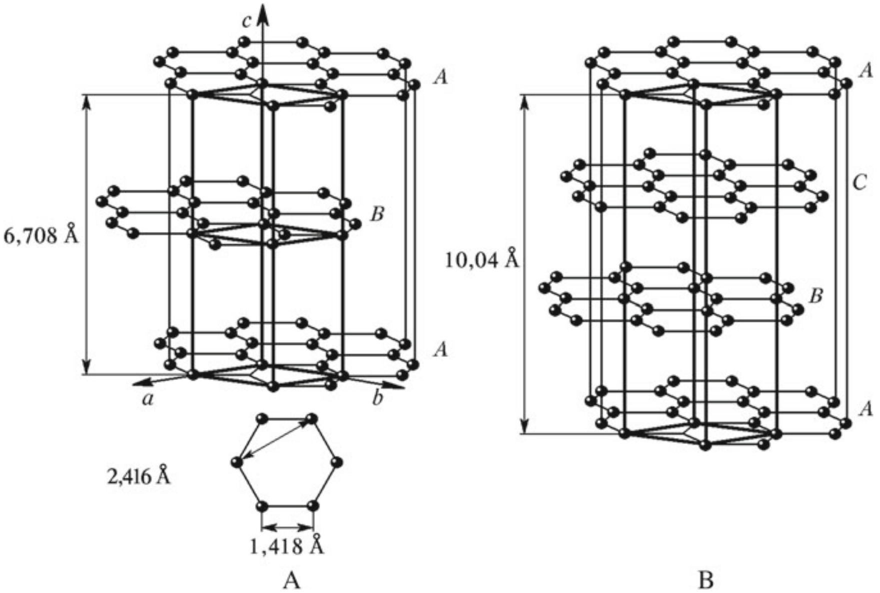

Fig. 10.2 The structures of hexagonal (left) and rhombohedral (right) graphite

in a complete disorder in terms of vertical configuration, though the parallelism of layers is preserved. This kind of defective structure is usually referred to as a *turbostratic* structure. The interlayer distance in the turbostratic structure is 3.44 Å.

The second type of defects is those in the lattice bonds. Such defects can be caused by the presence of foreign atoms, such as hydrogen, oxygen, and nitrogen, or of carbon atoms in different valence states. Defects in the graphite structure can also arise when alien elements enter the interlayer space. In sufficiently high concentration, they cause development of interstitial compounds.

Carbon-based materials are divided into graphitizing and non-graphitizing ones. Particularly important for the process of graphitization is structural anisotropy, i.e., relative positioning of the basic planes in starting materials. For graphitizing materials, the three-dimensional regularity of carbon layers (graphitization) emerges at temperatures of 1600–1800 °C. For example, carbon composites with non-carbon structures can be formed during graphitization of the surface of silicon carbide, monocrystals of which (4H, 6H poly-types) have exceptional emission characteristics (see Sect. 10.5.5).

Properties of a single graphite crystal are radically different along the a (in-plane) and c (normal to the plane) axes. This is caused by the layered structure of the crystal lattice. Development of anisotropy in polycrystalline graphites is based on specific features of the technology of fabrication. Thus, in compression molding, the particles become mostly oriented in the direction of the molding axis; in extrusion, the crystallographic axis is mostly perpendicular to the axis of extrusion. Glassy carbon and fullerenes are characterized by nearly total absence of anisotropy, while acrylic carbon fiber has a pronounced axial texture, i.e., the crystallographic axis is perpendicular to the fiber axis.

Basic properties of carbon-based materials to be taken into account when using them as FE cathodes include those related to adsorption. The high ability of carbon-based materials to adsorb various substances from gases and solutions onto their surface is exploited in the activated carbon process. Man-made carbon-based materials are expressly porous because their production process is connected with some mass loss and compaction of the structure, which results in shrinkage and cracking. There exists a convenient classification of carbon-based materials in terms of average width of their pores; this was proposed by M.M. Dubinin and developed in later papers dedicated to sorption properties of carbon-based materials [5]. Pores that are less than 20 Å wide are referred to as micropores; pores more than 200 Å wide are classified as macropores; and those in the range 20–200 Å are called intermediate pores.

The mechanical properties of carbon-based materials depend on the starting raw materials and the production-process parameters. In the temperature range of 20–2000 °C, graphites have limited plasticity, and are fragile as far as their fracture behavior is concerned. One should bear in mind that the larger the diameter of the blank, the higher is the coefficient of variation of the mechanical properties of the blank, and that the larger the grain size, the lower is the material strength.

Qualitative descriptions of electrical and electronic properties of different carbon-based materials can be given within the framework of a band model. The changes

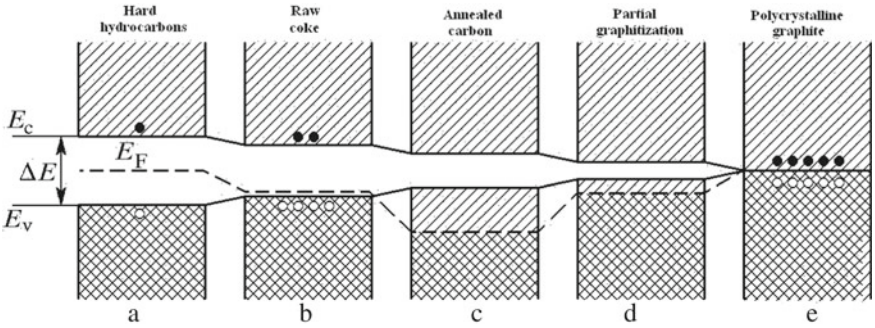

Fig. 10.3 **a**–**e** Diagrams showing the electron-energy bands and Fermi level positions for various carbon-based materials. E_V labels the valence-band maximum, and E_c the conduction band minimum. ΔE is the band gap, E_F labels the Fermi level

in electronic properties of carbon-based materials can be evaluated following the diagram shown in Fig. 10.3.

Figure 10.3 represents stages of transition—from solid aromatic hydrocarbons bound by van der Waals forces, to carbon-based materials of various types, through highly defective structures (coke), to almost ideal graphite. With the rise in the temperature of processing, the width of the band gap between the conduction and valence bands decreases, and becomes zero in the extreme case of infinitely large crystals of graphite, in which case the conduction and valence bands touch.

The valence band of carbon-based materials is formed by π-electrons of organized carbon-atom grids of a *macro-aromatic* nature. In the case of ideal graphite (Fig. 10.3a), the conduction band where there are no electrons at 0 °K is separated from the π-electron band by a negligibly small band gap. As a result of band adjacency and easy thermal excitation into the conduction band of ideal graphite, the number of electrons in the carbon conduction band is large enough for graphite to effectively behave like a metal.

Different stages of transmutations from aromatic hydrocarbons through intermediate forms of carbon to crystal graphite can be represented as a consecutive reduction of width of the band gap. In the temperature range of up to 1000 °C (Fig. 10.3b), cross-linking of the grids and emission of hydrogen during carbonization results in the emergence of holes in the π-band. The vacant free valences function as electronic traps localized on the defects (e.g., on the boundary atoms of the broken lateral chains of carbon and carbon layers).

Though partial filling of electronic bands should explain the *metallic* nature of the conductance of these carbon-based material types, they show a positive temperature coefficient of electrical conductivity. That is explained by the hole nature of conductance (or scattering) at the inter-grid boundary. With an increase in hole concentration, the lower band is gradually exhausted. It seems that at temperatures above 1400 °C (Fig. 10.3c), hole development due to hydrogen emission is mostly blocked. Cross-linking of broken grids taking place when the crystals grow reduces the number of hole defects acting as electronic traps. As this takes place, the π-band begins to refill. At the same time, dimensional growth of carbon grids causes reduction of the band-gap width ΔE. At a temperature of 2000 °C (Fig. 10.3d), this gap can be considered narrow enough for electrons driven by thermal excitation to pass into the conduction band. Therefore, unlike crystal graphite, which has an essentially metallic conductivity mechanism, the transition carbon forms are organic semiconductors with electrical properties determined by delocalized π-electrons.

We shall now describe the structural and FE properties of the above materials, as far as they have been studied up till now.

10.2 Carbon-Based Material Structures

10.2.1 Graphene

Graphene is a layer or "sheet" of carbon atoms, linked with sp^2 bonds and forming a hexagonal two-dimensional crystal lattice (see Fig. 10.4). It can be thought of as a graphite layer separated from the bulk crystal. Graphene has relatively high mechanical stiffness and good thermal conductivity. High mobility of current carriers at room temperature makes it a promising material for various applications. *Inter alia* can be used as a basis for nanoelectronics and a possible replacement for silicon in integrated microcircuits. At present, graphene is mostly produced by mechanical cleavage or exfoliation of graphite layers. This method produces the best samples, with high carrier mobility. It is not useful for large-scale production, however, because it is still very much a manual procedure. An approach much more suitable for industrial production is based on thermal decomposition of a silicon carbide substrate.

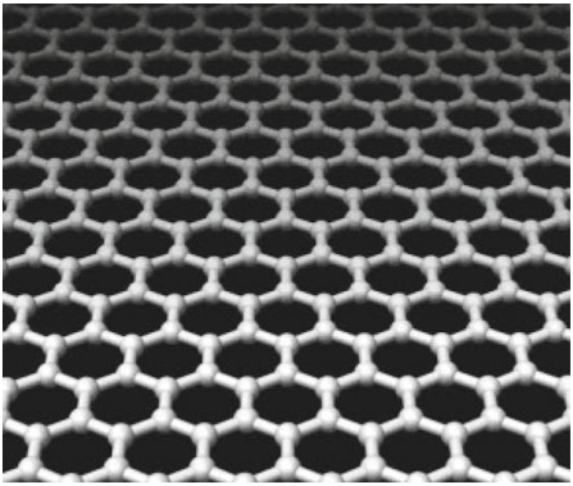

Fig. 10.4 Crystallographic structure of a graphene sheet

Because graphene was first produced as late as 2004, it has still not been studied in full depth, and thus generates keen interest. It is incorrect to view this material just as a piece of another allotropic carbon crystal such as graphite or diamond, because specific features of the energy spectrum of carriers in graphene make its electro-physical properties different from those of other two-dimensional systems.

Graphene nanoribbons are narrow graphene strips about 10–100 nm wide. Their physical properties differ from those of wider samples that follow the linear dispersion law, as an infinite graphene layer would do. Nanoribbons are particularly interesting because they follow a non-linear dispersion law, and have semiconductor properties—due to the presence of a band gap that depends on ribbon width and on the arrangement of atoms at its boundaries. This is why graphene nanoribbons are regarded as an important step toward making a graphene-based transistor working at room temperature. Graphene is also being considered as a possible base for the construction of a ballistic transistor. In 2006, a research group at the Georgia Institute of Technology around Walt de Heer announced that they had produced a graphene-based field transistor as well as a quantum interference device [6]. The researchers believe that their achievements can eventually develop into a new class of graphene-based nano-electronics, with the basic transistor thickness reduced to as little as 10 nm. Additionally, graphene can be used as a highly sensitive sensor to detect particular molecules of chemical substances attached to the film surface. Another promising application of graphene is to build electrodes in ionistors (supercapacitors), a promising class of rechargeable electricity sources. Despite all its obvious potential, the field emission properties of graphene have not yet been extensively studied.

10.2.2 Carbon Fibers

Depending on the starting raw material, carbon fibers can be divided into acrylic, pitch-based, and pyrocarbon ones.

The fibers of the first two types are manufactured commercially and their mechanical properties span a wide range in terms of values of their elastic modulus (200–700 GPa) and tensile strength (2–4 GPa). Here, we shortly recall relevant definitions: the elastic modulus is given by the applied tensile force per unit area (=tensile stress σ) divided by the relative elongation (=strain $= \Delta L/L_0 = \varepsilon$) and is given as the slope of the linear part of the stress/strain diagram (Hooke's law). The *ultimate tensile strength* is the maximum tensile stress of the stress/strain curve, i.e., the tensile strength at which the fiber breaks

Pyrocarbon fibers (pyros) have not been widely used in industry yet, and as yet there is little precise information about their behavior.

In terms of their mechanical characteristics, the acrylic carbon fiber family can be divided into *high-tenacity* (HT) and *high-modulus* (HM) ones. Several incompatible definitions of "tenacity" exist in the literature. In our view, the most appropriate definition of tenacity is "ultimate tensile strength, divided by the fiber density". For

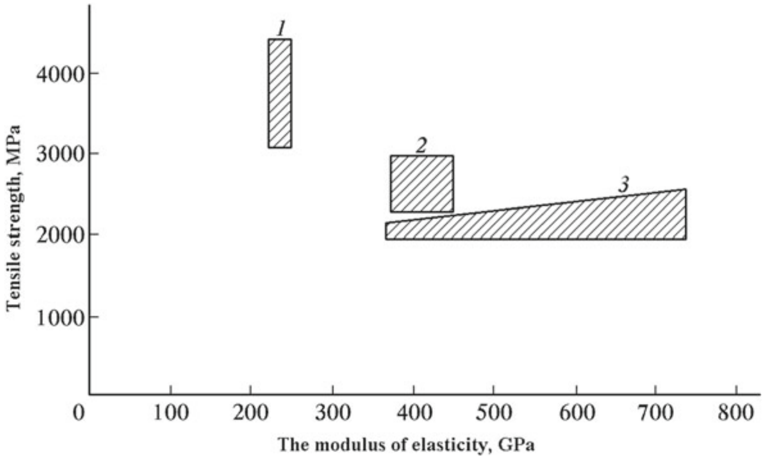

Fig. 10.5 Approximate ranges for the tensile strengths and elastic moduli, for carbon fibers of different types: 1—high-tenacity (HT) polyacrylonitrile-carbon fiber; 2—high-modulus (HM) polyacrylonitrile-carbon fiber; 3—mesophase pitch carbon fiber (see [3, 7])

"tenacity" defined in this way, the SI unit is usually stated as Pa m^3/kg or N m/kg. The high-tenacity carbon fibers are manufactured at temperatures below 1400 °C, high-modulus ones at temperatures of 1800–3200 °C. Typical ranges for the tensile strengths and elastic moduli of acrylic carbon fibers and pitch-based carbon fibers are shown in Fig. 10.5 [3, 4, 7].

The properties of carbon fibers, as with other graphite-based materials, are determined by their structure. The elastic modulus of a material is connected with interatomic forces. Producing high-modulus carbon fibers is feasible because of the extremely high interaction energy between carbon atoms in their hexagonally structured base-planes. Graphite tenacity along the base-plane is determined by the interaction between carbon atoms. The tensile strength of graphite in the perpendicular direction is much lower, because the interaction between the atoms of adjacent layers is weak. High thermal and electrical conductivity of graphite in the atomic-layer plane is caused by delocalization of valency-band p-electrons between the layers. Note that a graphite monocrystal should not be described as a metallic conductor, but rather as an overlapping-orbital semiconductor.

The greatest stiffness and tenacity of carbon fibers is reached only when the crystal-lattice layers are exactly parallel to the fiber axis.

Elastic moduli for a graphite monocrystal have been measured with great precision [8]. Figure 10.6 illustrates the three main coefficients relating to elastic properties: the Young's modulus under tension in the C_{11} carbon-layer plane, the Young's modulus under tension in the C_{33} orthogonal direction, and the C_{44} shear modulus.

The maximum possible value of Young's modulus is 1060 GPa, but this value can only be reached in the case of a defectless crystal structure with the atomic planes oriented exactly along the fiber axis. The elastic modulus of fibers in the orthogonal

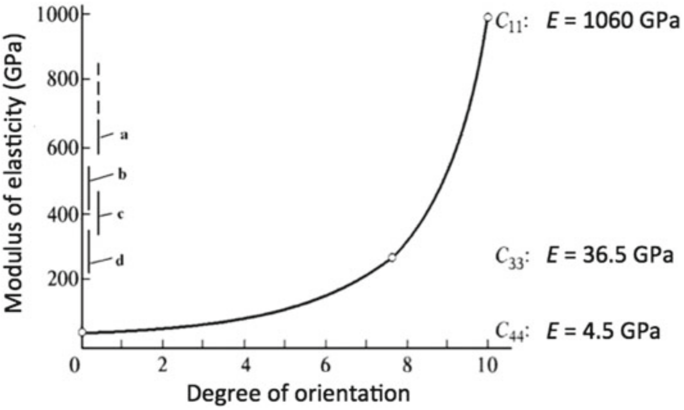

Fig. 10.6 **a** Modulus-of-elasticity values for various carbon-based materials, and the influence of the degree of orientation of atomic layers: a—graphite fibers (based on mesophase pitch); **b** carbon fiber (based on mesophase pitch); c—high-temperature PAN carbon fiber; d—low-temperature PAN carbon fiber. The curve plotted is Young's modulus *E* versus the degree of orientation for a graphite monocrystal based on an equation given by B. Kelly [8]

direction is an order of magnitude smaller. The minimum value (usually about 4.5 GPa) is that of the shear modulus. Fiber tenacity is directly proportional to the fraction of atomic layers oriented along the fiber axis. Disorientation of atomic planes decreases tenacity along with a decrease in the actual value of the elastic modulus. The theoretical tenacities of high-tenacity and high-modulus fibers are 70 and 25 GPa, respectively. For high-modulus fibers, the tenacity can only be implemented up to 3% of theoretical estimates, i.e., 2.1 GPa, and even the best high-tenacity fibers don't reach more than 5 GPa, which is 2% of theoretical maximum. Figure 10.6 shows the dependence of the experimental values of the fiber elasticity modulus on the degree of orientation of the carbon-atom layers. In the best industrial samples of fibers, the elastic modulus reaches 70% of the theoretically possible value.

Despite high-tenacity in the plane of an atomic layer, the crystal can be easily bent or curved, due to the low shear modulus. An interlayer shear becomes more difficult with the introduction of defects into the crystal lattice. Defects within a layer, such as vacancies, insertions, disclinations, as well as layer-packing defects, increase the interlayer distance. Layer and interlayer defects are often interconnected, because defects inside a layer can lead to improper packing of the adjacent layers and result in an increase in the interlayer distance; this causes incomplete delocalization of electrons and impedes interlayer shear. Disclinations also interfere with the shear and lead to the emergence of vacancies and improper packing of adjacent layers.

The occurrence of disclinations and the degree of carbon-layer orientation are mainly determined by the structure of the starting fiber. Additionally, these carbon fiber characteristics depend on the draw-down rate at the initial stage of fiber production. The inside-layer defects and the layer-packing defects are largely eliminated during heat treatment.

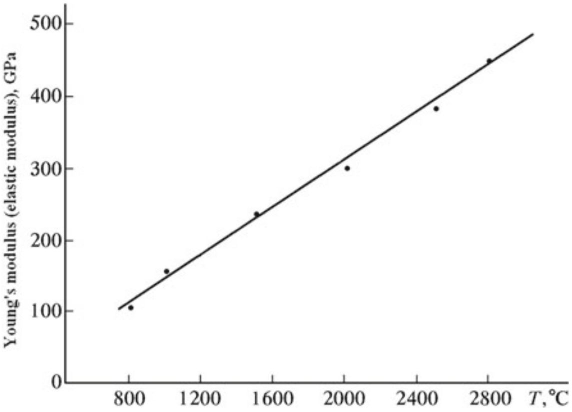

Fig. 10.7 The dependence of Young's modulus on the temperature of heat treatment of polyacrylonitrile ("PAN") carbon fibers

For industrial fibers, the elastic modulus is a stable characteristic because it is determined by the final processing temperature and the draw-down ratio, and these technological parameters are well reproducible. Figure 10.7 illustrates, for PAN fibers, how the fiber's structural properties depend on the processing temperature. Production of fibers with stable tenacity is much more difficult, because tenacity depends on the presence of cracks and other macrodefects, and these are largely decided by the properties of the raw fiber. The use of chemically pure acrylic carbon fibers enables chemically pure and homogeneous carbon fibers to be produced.

Most important for field emission are the properties of carbon fiber surfaces, as fully described by means of

(1) The surface-layer composition, i.e., the functional group types present and their concentration, as well as the presence of impurity atoms;
(2) Surface energy per unit area, and its changes when gaseous substances are adsorbed;
(3) Specific surface geometry, roughness, microporosity;
(4) Number of surface cracks and their size distribution;
(5) Shape and size of the filament (elementary fiber), its structure, and the surface anisotropy.

Because of the great fiber anisotropy, and the related great variation in surface electrostatic field when the fiber is charged overall, the fiber end-surface field emits most strongly. This fiber end-surface is a set of chaotically located micro-elevations of different heights, radii of curvature, and configurations. When an electrical voltage is applied, the numerous micro-elevations are sure to include a few with a relatively high electric field at their vertices. These micro-elevations are the initial emission centers when voltage is applied. With further increase in voltage, the electric field becomes sufficient for emission from other, less sharply pointed, micro-elevations.

The initial distribution of emitting centers over the fiber end-surface is absolutely arbitrary, and does not coincide even for quite closely located sites of the same filament. This is primarily due to the variability of mechanical properties along the fiber axis.

10.2.2.1 Acrylic Carbon Fibers

Acrylic carbon fibers are produced by pyrolysis of polymeric polyacrylonitrile (PAN) fibers and subsequent high-temperature processing. These carbon fibers have a filament diameter of 6–10 μm. They are about 99.9% pure carbon, and are normally described as "chemically pure". The technology of carbon fiber production from a synthetic PAN fiber includes the following operations [9–11].

(1) Oxidization of the PAN fiber in atmospheric oxygen for several hours at temperatures ranging between 200 and 300 °C, with the fiber held in a state of tension in order to prevent shrinkage and drawing of the fiber. As this oxidation takes place, polymeric molecules turn into six-link rings, oriented along the fiber axis and containing carbon and nitrogen. This operation increases the elastic modulus and the fiber tenacity.
(2) Carbonization of the oxidized fiber, without tension, at a temperature of up to 1000 °C, in an inert atmosphere.
(3) Graphitization in the inert atmosphere, at temperatures up to 3200 °C.

If graphitization is carried out at processing temperatures of 1000–1700 °C, then high-tenacity fibers are produced [4]. But most interesting for field emission is the high-modulus fiber type fabricated by using processing temperatures up to 3200 °C, which is referred to as a *graphite fiber*. Figure 10.7 shows how Young's modulus value depends on the final processing temperature. Conspicuous is the fact that this dependence is linear.

The elastic modulus of the fiber increases with an increase in the degree of orientation of the structure (see Fig. 10.7). At the same time, the specific electrical resistance or electrical resistivity ρ of the fiber decreases (see Fig. 10.8). Figure 10.8 also shows that structural features of the fiber change. Each fiber consists of many, much smaller, structural components called *microfibrils*. The typical dimensions L_a and L_c of these microfibrils (in directions parallel to the "*a*-" and "*c*-" crystallographic axes in graphite, respectively) depend on the production conditions and temperature, and range from $L_a = 10$ to 50 nm, and $L_c = 2$ to 5 nm. The fiber density d also changes.

It is worth noting that the curves in this diagram only show representative qualitative tendencies, because each carbon-fiber batch has its own values of the specified parameters, depending on the starting acrylic carbon fiber structure and the carbon-fiber production technology. Figure 10.9 represents three fiber structure types [3, 11] identified so far, which differ in the orientation of the graphite crystal grains in the fiber cross-section.

Structures (a) and (b) are double-band, while structure (c) is single-band. Structure (a) has preferential orientation at the circumference of the surface crystal grains of the fiber, with the inner part having chaotic orientation. It is mostly generated by amorphous carbon.

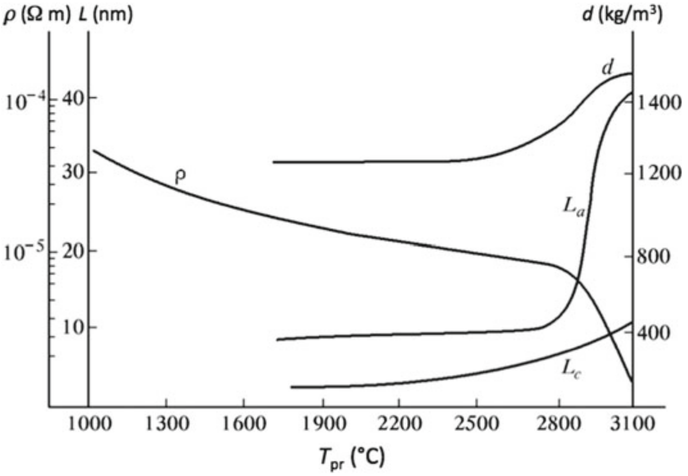

Fig. 10.8 Representative changes in the structural parameters of graphite-type carbon fibers, as the heat treatment temperature T_{pr} increases: ρ—electrical resistivity; d—density. L_a and L_c are the average values of crystallite ("microfibril") dimensions in the directions of the *a*-axis and *c*-axis in graphite, respectively

In the second type of structure, (b), the surface layers of crystal grains are mostly oriented at the fiber circumference, the neutral band displaying radial orientation.

The third type of structure is characterized by the cylindrical orientation of crystal grain *c*-axes over the entire fiber cross-section. It is worth noting that the supramolecular structure of the starting fiber is inherited by the processed carbon fiber and is almost independent of the final processing temperature.

To evaluate the effect of fiber characteristics on field emission, it is necessary to have a clear idea of the carbon-fiber structure and of any specific features of its emitting surface.

The earliest models represented a fiber as a conglomerate of interconnected highly oriented fibrils of sub micrometer size. After heat treatment at 2000 °C, the high-modulus carbon fibers have been established to contain at least two phases, both consisting of fibrils with graphite insertions. One phase consists of wider and thicker ribbons with increased longitudinal orientation. The other phase is built from narrower, less oriented, and intensely intertangled fibril ribbons. Both phases contain a large number of pores, micro-cracks, and other defects. In the central part of the fiber, fibril orientation is usually less exhibited; fibrils with fewer defects are found at the outside. Between these two regions, there is an intermediate layer containing ribbons of both types. The up-to-date fiber micro-crack model (for the structure shown in Fig. 10.9b) is illustrated in Fig. 10.10 (compare [12]).

The fiber surface is its best-oriented part. It contains both exposed crystallite boundaries and defectless basic atomic planes. Highly energetic boundary atoms are linked with each other by sp^2-bonds and are able to chemosorb oxygen in an active way. The base-plane surface atoms forming the structure of an ideal graphite lattice

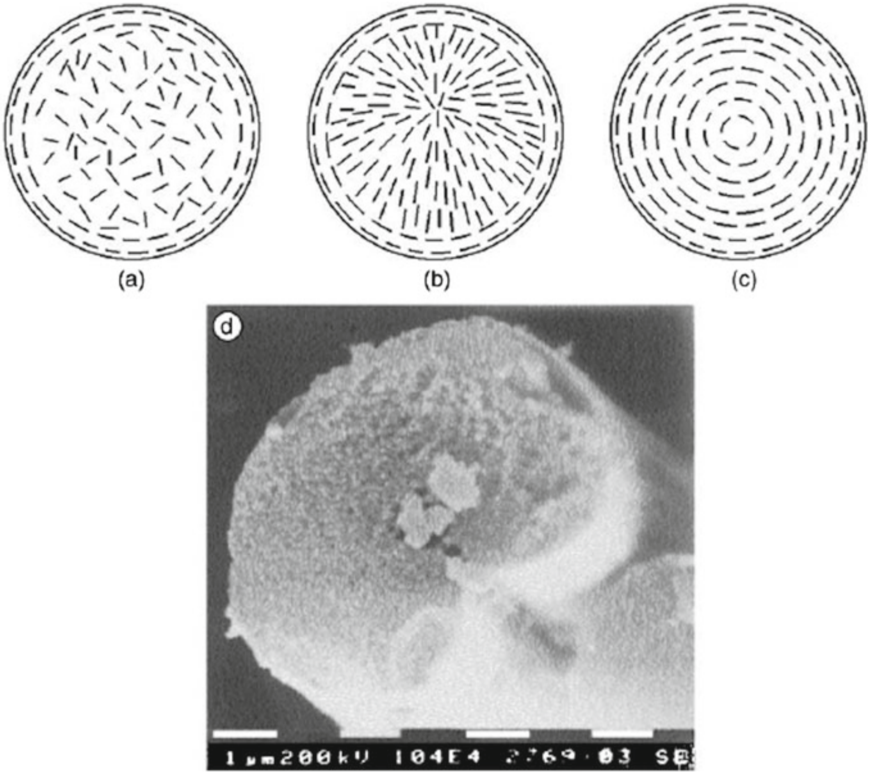

Fig. 10.9 Schematic illustration of the internal structure of PAN fibers: **a** isotropic center and oriented surface layer; **b** different orientation of the center and the surface layers; **c** one type of preferred orientation; **d** photograph of the working surface of the carbon fiber type "VULON"; from [3]: E.P. Sheshin, Properties of carbon materials, especially fibers, for field emitter applications, Appl. Surf. Sci. **215**, 191–200 (2003), with permission of Elsevier

interact with the weakest σ-bonds, and have considerably lower surface activity. In addition, the fiber surface can have a fibril-like microstructure, micropores, crystallite boundaries, foreign insertions, and cracks, making it susceptible to mechanical destruction. To produce high-quality carbon fibers, three requirements have to be met:

(1) reduction in the fiber diameter, to decrease the probability of serious structural defects;
(2) use of high-quality, chemically pure polymeric raw materials; and
(3) high reproducibility of technological processes, especially at the oxidation stage.

At this point in time, the most extensive studies have been on the FE properties of acrylic carbon fibers. FE cathodes made from such fibers are promising for some practical applications.

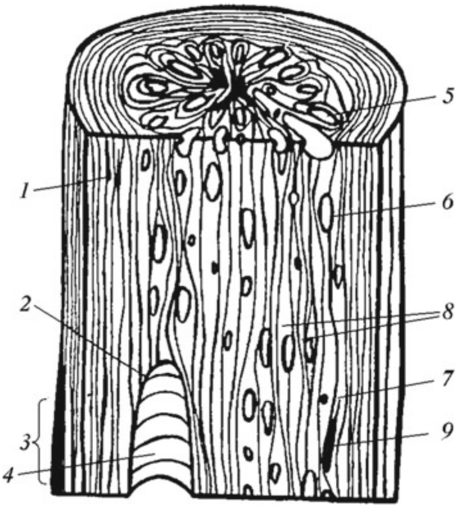

Fig. 10.10 The structure of polyacrylonitrile (PAN) carbon fibers: 1—micro-cracks; 2—shell cracks and pores; 3—convexity on the fiber; 4—big pore; 5—small pore; 6—micro-inclusions of crystalline graphite; 8—interfibril layers in the middle part of the fiber; 9—micro-crack; from [12]: E. P. Sheshin, Field emission of carbon fibers, Ultramicroscopy **79**, 101–108 (1999); with permission of Elsevier

10.2.2.2 Pitch-Based Carbon Fibers

The production technology for pitch-based carbon fibers consists of five basic stages: (1) pitch preparation; (2) fiber spinning/formation; (3) stabilization through oxidation; (4) carbonization; and (5) graphitization (to produce high-modulus carbon fibers).

To produce the pitch of the desired quality as the starting material, it is necessary to increase its aromatization, molecular mass, and melting point. An additional step in pitch preparation is to turn it into the so-called mesophase pitch, which is characterized by spinnability.

Pitch having the above qualities is heated at 350–500 °C in a protective atmosphere for a prolonged period. Heating causes a series of transmutations and results in the development of polycyclic large molecules, which come together in the liquid-crystal phase, i.e., the mesophase. This phase has a larger surface tension than the isotropic phase (with low relative molecular mass) from which the mesophase grows. The mesophase consists of large flat molecules oriented parallel to each other in such a way as to form spherical crystals (spheroids); these grow and coagulate into large spheres, resulting in a bulk mesophase. Eventually, the mesophase pitch has a heterogeneous structure consisting of an anisotropic mesophase and isotropic regions. There are many detailed production methods for mesophase pitch, but exact technological details are most often kept as corporate or industrial secrets.

To produce fibers from the pitch, the prepared pitch is drawn through spinnerets. The wet process involves a special coagulation bath, where a bundle of up to 320,000 elementary fibers is formed. In the dry method, the number of elementary fibers produced is smaller, although the fiberization rate is higher. Drawing can be done by centrifugation, structural processes, or appropriate pitch melting.

Spinneret orifice configurations can be widely different. Together with drawing-mode variations, these differences yield fibers with many different structures. For example, the radial carbon fibers are produced as a result of the laminar flow of the mesophase pitch through spinnerets. Cross-section models of the main types of pitch-based carbon fiber are shown in Fig. 10.11.

Table 10.1 shows structural parameters, found by X-ray diffraction, for some pitch-based carbon fibers. The fibers are identified by their "brand" names/codes. The table shows that the carbon fibers made from isotropic pitch have lower values of the fibril parameters L_a, $L_{c,}$ and higher values of the parameter d_{002} than mesophase pitch-based carbon fibers. (L_a and L_c have been explained when discussing Fig. 10.8; the crystallographic parameter d_{002} is equal to half the interlayer spacing between the graphene sheets in graphite). In the course of graphitization of isotropic pitch-based fibers, crystallite sizes increase and the interlayer parameter d_{002} decreases.

10.2.2.3 Pyrolytic Carbon Fibers

Carbon fibrils, i.e., pyrolytic carbon fibers, are among the solid products of pyrolysis of gaseous hydrocarbons. Visually, pyrolytic carbon fibers are similar to graphite whiskers [13].

Pyrolytic carbon fibers are grown on graphite substrates using preliminary seeded salts of iron, nickel, and cobalt. As a result of pyrolysis of methane at 1100–1400 °C, with a residual gas pressure of 20–80 Torr (namely 3–11 kPa), such fibers grow in the direction perpendicular to the deposition surface. The linear growth rate is about 10 mm/min. Fully grown fibers can be as long as 30 mm and the diameter can reach 70 μm.

Pyrocarbon fibers are formed only in a particular range of hydrocarbon/methane concentrations. As formation takes place, a portion of pyrocarbon is deposited as a continuous coating and another portion forms carbon fibers. These fibers are polycrystalline. They mainly consist of turbostratically structured carbon with crystallites of size ~40 Å, and with high fiber-axis orientation of hexagonal layers (see Fig. 10.12). Pyrocarbon fibers are formed in stages, as follows [14].

(1) Decomposition of the catalytic agent spreads on the sample surface when heated in the methane atmosphere, with the associated formation of reduced metal on the particle surface.
(2) Formation, above the surface, of bulk electric charge caused by evaporation (in an ionic form) of potassium present in the catalytic agent. This induces electric charge of the opposite sign localized on surface irregularities.
(3) Intensification of reactions in the gaseous phase as temperature rises, i.e., potassium ions evaporate, and iron atoms become centers of homogeneous crystallization of carbon. In addition, the rising temperature disturbs the balance between bulk and surface electric charges.
(4) Development of carbon fibrils as a result of Coulomb interaction between bulk carbon-bearing electric charges and electric charges located on surface irregularities, and then at the apexes of the growing fibrils.

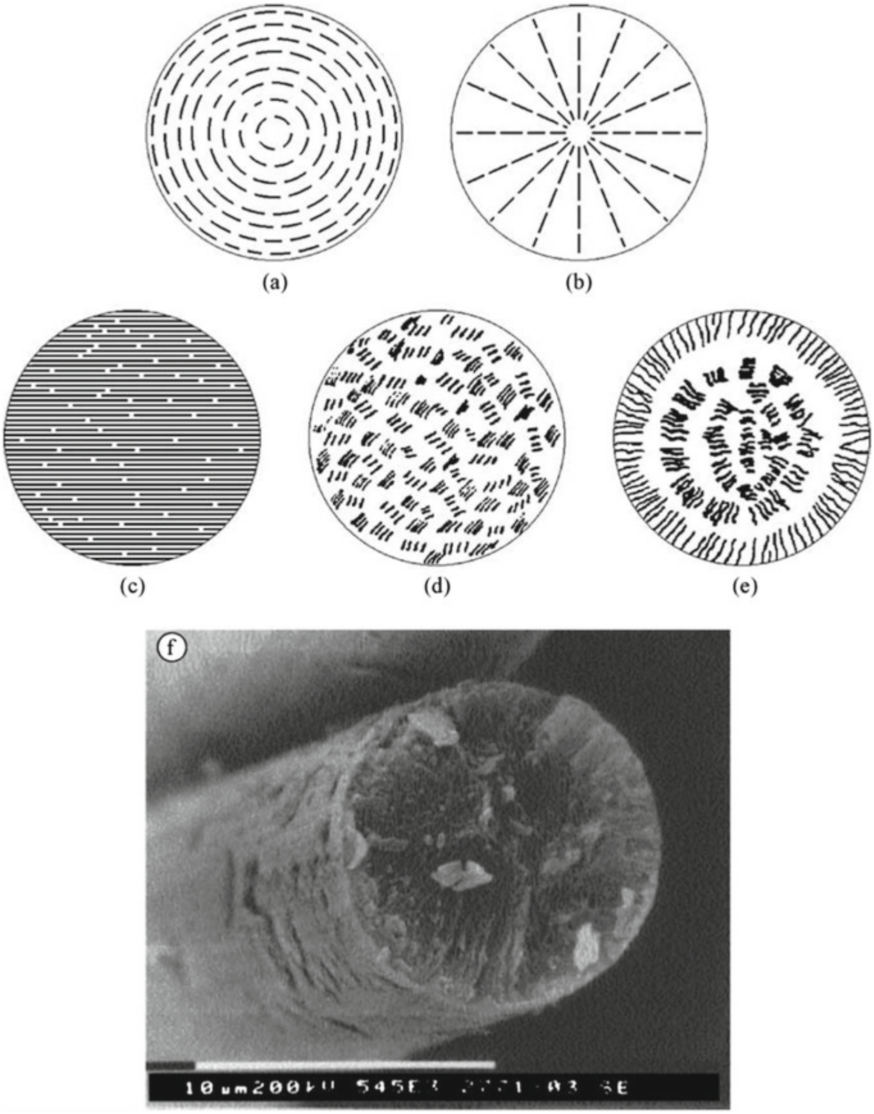

(a) (b)

(c) (d) (e)

Fig. 10.11 Models for the cross-sections of pitch carbon fibers: **a** onion-skin type structure (tangential); **b** radial structure; **c** structure of R-series fiber; **d** isotropic structure; **e** structure of fiber type TP; **f** SEM micrograph of the working end-surface of a "brand P-25" carbon fiber; from [3]: E.P. Sheshin, Properties of carbon materials, especially fibers, for field emitter applications, Appl. Surf. Sci. **215**, 191–200 (2003), with permission of Elsevier

Table 10.1 Properties of different "brands" of pitch-based carbon fibers

Brand of Carbon fiber	Structure	Fibril length (a-axis) L_a (nm)	Fibril length (c-axis) L_c (nm)	Lattice parameter d_{002} (nm)	Main feature of carbon fiber
J	Isotropic	2.62	1.07	0.41	Isotropic fiber
JG	Isotropic (graphitized)	9.65	3.7	0.34	Isotropic fiber with processing temperature of 2700 °C
MP	Mesophase	6.46	2.05	0.35	Fiber based on mesophase pitch, suitable for general purpose applications
TP	Mesophase	19.05	11.9	0.34	High-modulus fiber based on mesophase pitch
P-25	Mesophase	18.6	11.3	0.34	Fiber based on mesophase pitch
P-75	Mesophase	20.9	14.6	0.34	High-modulus fiber based on mesophase pitch
P-100	Mesophase	21.2	19.7	0.34	High-modulus fiber based on mesophase pitch
P-120	Mesophase	21.8	21.5	0.34	High-modulus fiber based on mesophase pitch

(5) Growth of thin fibrils as the temperature rises.
(6) Growth in fiber diameter, caused by layer-by-layer deposition of pyrocarbon.

The resulting fiber structure depends on the particular conditions of pyrocarbon growth, including the substrate temperature, the pressure of methane, and the pressure gradient along the fiber length.

The specific electrical resistance (electrical resistivity) of pyrocarbon fibers is in the range of 5–10 Ω μm. The tensile strength of pyrocarbon fibers is strongly dependent on their diameter, as may be deduced from Fig. 10.13. The basic length of the sample in these trials was 3 mm. Figure 10.13a shows that the strongest fibers have a diameter of less than 10 μm, and a tensile strength around 2 GPa. With an increase in the diameter up to 30 μm, fiber tensile strength decreases to 0.6–0.8 GPa. Along with the dependence of strength on diameter, the pyrocarbon fiber tensile strength has been found to depend on another geometrical factor, namely fiber length. This form of dependence is shown in Fig. 10.13b, where the fiber diameter is 8–10 μm. However, analysis of the dependence shows that a tenfold increase in

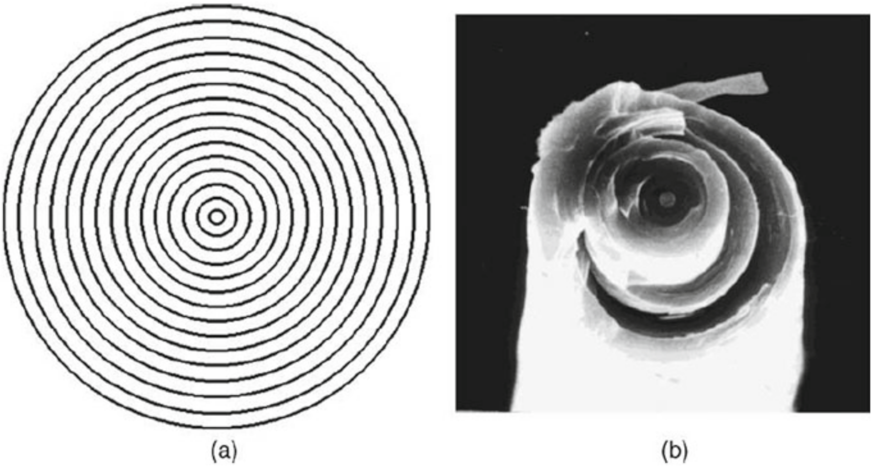

Fig. 10.12 Pyrolytic fibers: **a** model of the transverse structure; **a** SEM micrograph showing the end-surface of the fiber; from [3]: E.P. Sheshin, Properties of carbon materials, especially fibers, for field emitter applications, Appl. Surf. Sci. **215**, 191–200 (2003), with permission of Elsevier

the basic length reduces fiber tensile strength by as little as 40%. In addition to the scale factor, pyrocarbon fibers are characterized by considerable variation in how tensile strength varies with fiber length, as a result of different structural defects in the samples.

In addition, the manufacturing of FE cathodes normally involves man-made carbon-based materials. Such materials are produced from organic substances whose destruction results in coke residue, which is a solid carbon product.

10.2.3 Pyrographite

Pyrolitic graphite or pyrographite [15–18] is produced by the decomposition of carbon gases (propane, methane, acetylene, etc.) on surfaces heated to 1000–2500 °C. If pyrolysis proceeds in a condensed phase, the result is low-temperature pyrographite, i.e., pyrocarbon (800–1400 °C) [19]. Decomposition of hydrocarbon gas at higher temperatures, usually above 2000 °C, results in true pyrographite.

Pyrographite is a hypocrystalline material characterized by a high degree of preferred orientation of crystallites along the deposition surface. X-ray diffraction studies show that some crystallites have a well-expressed texture of the plane (002) parallel to the deposition surface. Order increases as the pyrographite synthesis temperature rises, and temperatures above 2300 °C cause the development of three-dimensional order.

Pyrographite of more than 98.5% theoretical density, i.e., 2100–2200 kg/m^3 (2.1–2.2 g/cm^3) has low porosity and increased corrosion stability.

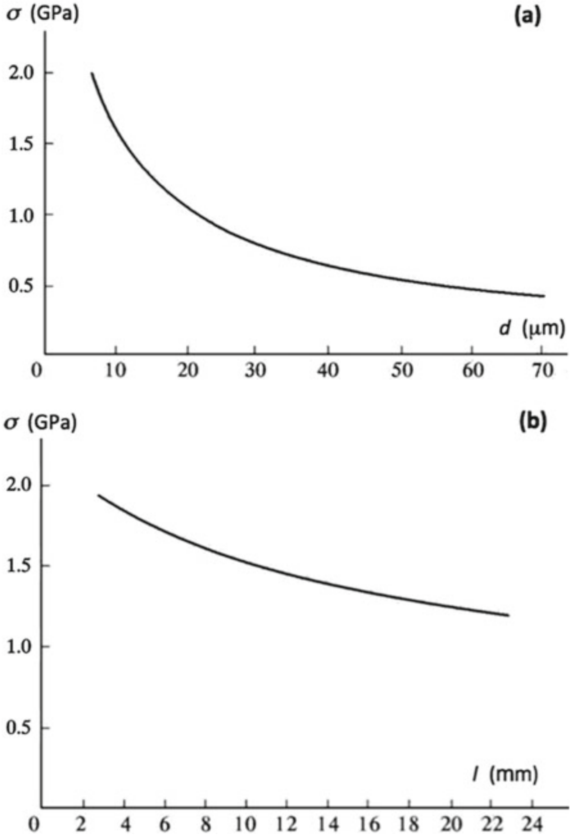

Fig. 10.13 Dependence of the average tensile strength σ of pyrolytic carbon fibers on **a** fiber diameter d; **b** fiber length l

The pyrographite production temperature is among the key parameters determining its structure and properties. However, temperature-effect data need to be treated with care, since the temperature measured can differ considerably from the real one, due to strong temperature gradients. Deposition temperature variations, even as little as ±20 °C, cause considerable changes in the pyrographite structure.

In this connection, pyrographite properties can widely differ along the deposition surface. This is because gas movement along the surface changes not only the temperature, but also the composition of the gases transported, and sometimes even their response time. In aggregate, these things can change the deposition rate and the pyrographite structure, depending on the distance from the gas ingress place. It is worth noting that studies of pyrographite microstructure sometimes find deposition irregularities, which have caused the emergence of additional inter-boundary regions.

The typical appearance of the effective surface of a pyrographite sample suitable for manufacturing FE cathodes is shown in Fig. 10.14. The picture gives a good view of the pyrographite layers opening out into the effective surface.

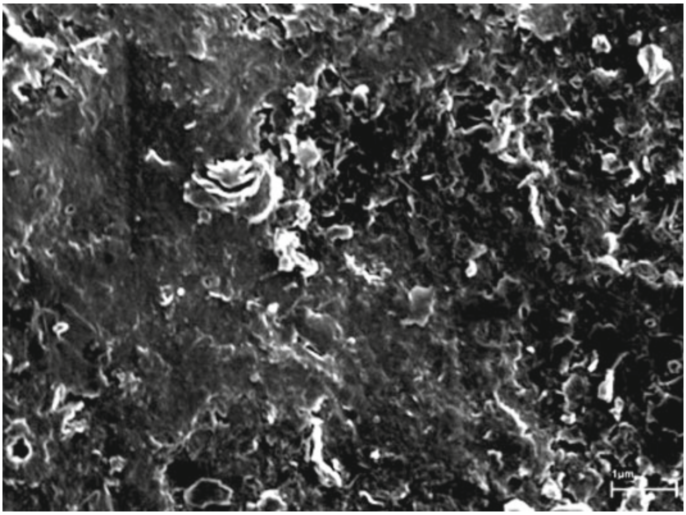

Fig. 10.14 The surface structure of pyrographite; the length of the bar in the lower right corner is 1 μm

10.2.4 Glassy Carbon

Glassy or vitreous carbon is a product of the thermal destruction of cross-linked thermosetting polymers that undergo non-reversible hardening when heated, and are capable of carbonization at the same time. The starting thermosetting polymers most often used are phenol-formaldehyde and furfural resins [20, 21].

Almost all substances used as raw materials to manufacture glassy carbon have the following specific characteristic: there is no clear dependence of final physical and chemical properties on the conditions of synthesis, such as temperature, pressure, and the molecular ratio of the starting components. Thus, the starting raw materials most suited to the glassy-carbon production conditions are chosen by practical considerations.

The characteristic properties of glassy carbon include high compressive strength in the range of 200–500 MPa [22] or even higher at small density (usually about 1450–1550 kg/m^3 or 1.45–1.55 g/cm^3), low fluid and gas permeability, chemical inertness against the most aggressive media, high thermal stability, and high surface purity. In addition to products in various other configurations, glassy carbon is used to manufacture fibers of diameter 6–30 μm that have high tensile strength.

X-ray diffraction analysis shows that there is no three-dimensional order in the glassy-carbon structure. This is also confirmed by the nature of X-ray photoemission spectra. Low-temperature glassy-carbon samples seem to have oxygen bridges. Apparently, all the above suggests that glassy carbon has different types of carbon–carbon bonds irregularly distributed in the material bulk.

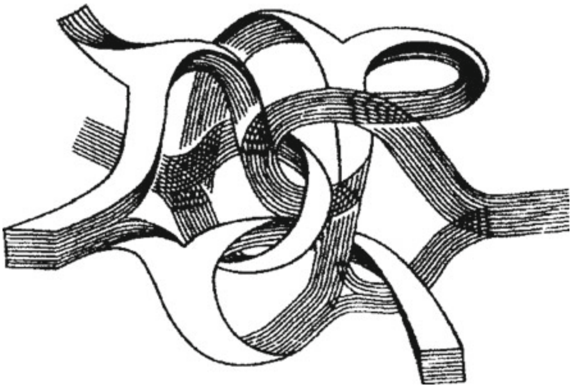

Fig. 10.15 The molecular belt model for the structure of glassy carbon

Glassy carbon does not graphitize at temperatures below 3200 °C. Carbon atoms form small two-dimensional graphite-like layers linked by carbon atoms with 1.55 Å long tetrahedral bonds into a three-dimensional polymeric structure. Figure 10.15 shows a "molecular belt" model of glassy carbon, taking account of microfibril formation. Their presence determines the unusual properties of glassy carbon.

Glassy carbon has micro- and transition pores. Depending on the processing temperature, the pore diameter averages at about 24–62 nm. The walls can have micropores of diameter 3 nm or less. Most of the bulk is made of closed pores, which enables the fabrication of products having almost no through-porosity.

There is also another interesting structural modification of glassy carbon, so-called reticulated vitreous carbon (RVC) foam (see Fig. 10.16) [22]. This name is partially explained by the material structure. The RVC foam has an extremely large number of open pores, up to 96%, which essentially distinguishes it from other kinds of glassy carbon, where pores are mostly closed. As a result, the RVC foam is characterized by extremely low density, no more than 50 kg/m^3, and high gas and fluid permeability. At the same time, it preserves all carbon properties.

Analysis of the porous structure of the RVC foam shows that its surface area increases with the reduction of pore size and growth of their number.

In addition to the above-described materials, FE cathodes can be based on carbon films. It is important to underscore that the same methods can be used to produce carbon films with different structures, because the methods depend on the starting composition and conditions of sample production.

10.2.5 Nanotubes

Carbon nanotubes are extended cylindrical structures, as shown in Fig. 10.17, with the diameter ranging from one to several tens of nanometers and length up to several micrometers. They basically consist of one or several hexagonal sheets rolled up to form quasi-cylindrical "walls", and in some cases have "caps".

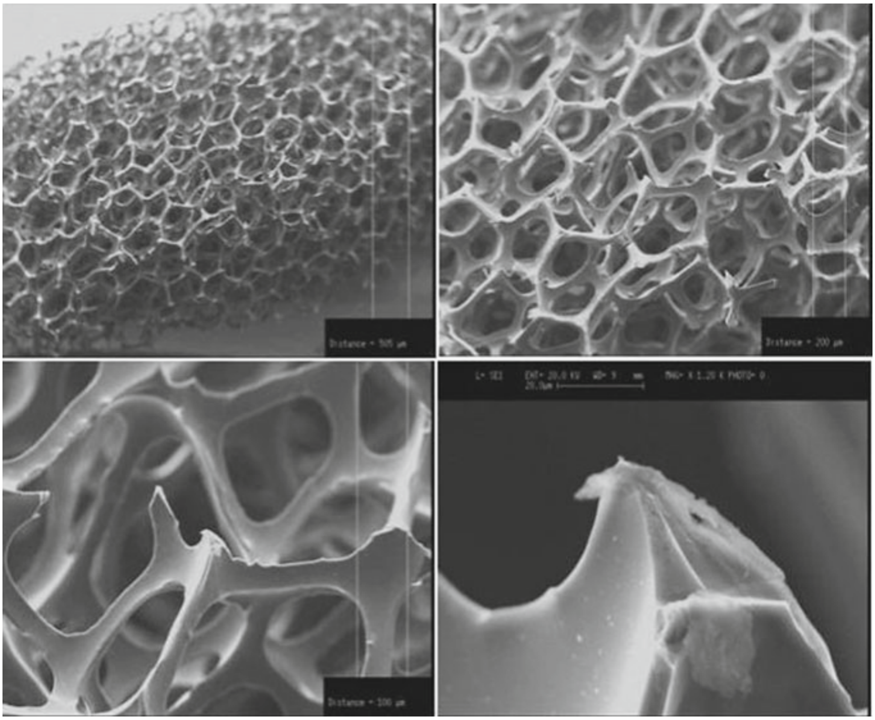

Fig. 10.16 SEM micrographs of the structure of reticulated vitreous carbon (RVC) foam with increasing magnification; the distance between the two vertical white lines is decreasing from 500 µm (upper left) via 200 µm, 100 µm to 20 µm (white bar, lower right)

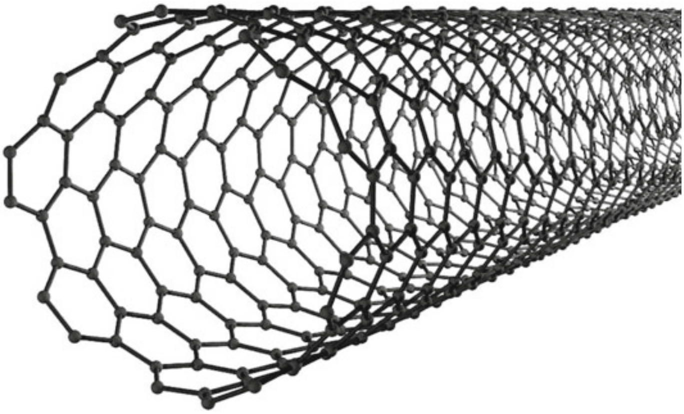

Fig. 10.17 Basic "rolled graphene" structure of a simple carbon nanotube

In 1991, Iijima identified carbon nanotubes by high-resolution electron microscopy [23]. The tubes produced in the first experiments were multi-wall structures differing in the number of layers, the shape of boundaries, and other characteristics. Differences in the chemical activity of a cylindrical nanotube and its hemispherical cap allowed the development of methods of control over the parameters of nanotubes, on the basis of their partial oxidization.

The ideal nanotube is a rolled graphene plane, i.e., a surface made of regular hexagons with carbon atoms at the vertexes. An idealized model of a one-layer (or "single-walled") nanotube is shown in Fig. 10.18. Such a tube has no seams on the generating line and ends with hemispherical "caps" containing not only regular hexagons but also six regular pentagons. The presence of pentagons on the tube ends suggests that we might regard the tube as an extreme case of a fullerene molecule, where the length of the longitudinal axis considerably exceeds the diameter. Real nanotube structures can differ significantly from the ideal one, particularly in the structure of the vertices or fiber ends, which also could be open or truncated.

Multi-walled nanotubes differ from single-walled ones in having a considerably wider variety of shapes and configurations, both in the longitudinal and transverse directions. Some possible modifications of the transverse structure of multi-walled nanotubes are shown in Fig. 10.19. The first two modifications are a complex of

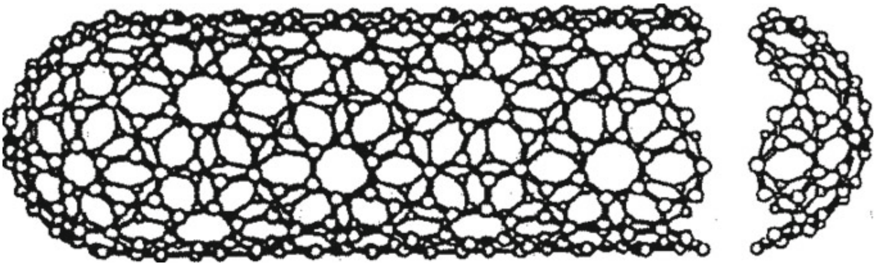

Fig. 10.18 Idealized model of a single-walled carbon nanotube, including quasi-hemispherical "caps"

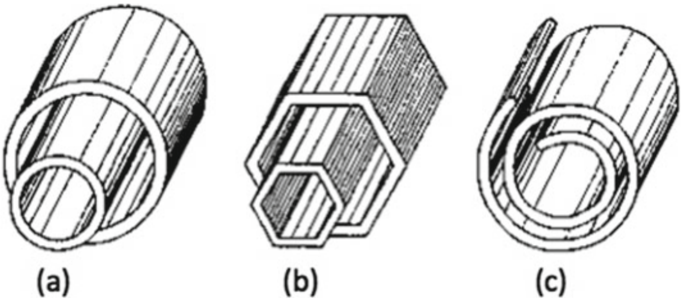

Fig. 10.19 Model transverse structures of multi-walled nanotubes: **a** "Russian doll" (left); **b** hexagonal prism; **c** scroll (right)

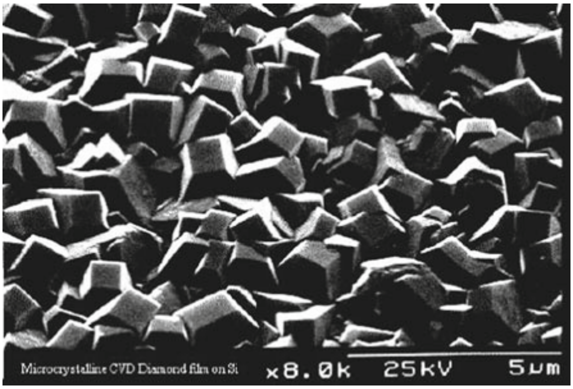

Fig. 10.20 The structure of diamond-like films

single-walled cylindrical tubes put one into another (Fig. 10.19a), or coaxial prisms (Fig. 10.19b). The last of the structures (Fig. 10.19c) resembles a scroll.

Implementation of this or that structure depends on the particular conditions of nanotube synthesis. However, all structures have the distance between adjacent walls close to 0.34 nm, i.e., the distance between adjacent base-planes of crystal graphite. At present, there are no direct experimental data indicating the prevalence of this or that particular structure, the main reason being the insufficiently high resolving ability of contemporary analytical devices.

Recently, much attention has been paid to filling nanotubes with various substances. This can have great practical importance, e.g., for reduction of electronic work function or (potentially) in quantum computing. Filling nanotubes is done by capillary suction of molten metal or solutions. There is a particular interest in filling nanotubes with Cs. Partial filling can also be achieved via embedded catalytic nanoparticle seeds (Fe, Ni) in a PCVD process [24].

The electrical resistivity of some nanotubes is close to that for graphite, but for nanotube films and bundles, the resistivity can vary significantly.

10.2.6 Diamond-like Films

Many authors refer to solid carbon films as “diamond-like”, on the grounds that there is some similarity between their properties and those of diamond. The geometrical surface structure of such a film is illustrated in Fig. 10.20. In fact, analysis of the bond structures in carbon films shows that these structures are neither fully diamond-like nor fully graphite-like, but are complex systems containing both types of bonds, and amorphous regions, all present together.

There are many methods for producing diamond-like films. The most widespread is by chemical vapor deposition (CVD) onto a substrate [25]. The films produced by CVD have the lowest content of the graphite phase. The carbon film on the substrate surface is formed when carbon ions deposit out of a hydrocarbon gas, usually methane. Sufficiently high substrate temperature (over 1000 °C) enables epitaxial film growth. High concentration of carbon atoms causes the growth of a mostly amorphous carbon film. To prevent that, the non-diamond carbon phases are etched with atomic hydrogen while the films grow. To achieve this effect, the working gas is enriched with hydrogen up to 99%. In this case, it is considered that a plasma etch using chemically pure atomic hydrogen transfers the non-diamond structures of the growing film into the gas phase [25].

Currently, a search of new carbon-based materials usable as FE cathodes is under way. For today, fullerenes and onion-shaped carbon structures seem to be among the most interesting ones.

10.2.7 Fullerenes

Fullerenes are a wide class of polyatomic carbon molecules. They are stable polyatomic carbon clusters consisting of at least several tens of carbon atoms. A fullerene C_{60} molecule is illustrated in Fig. 10.21.

The name was a homage to the engineer and designer Richard Buckminster Fuller, whose geodetic constructions follow this principle. The number of carbon atoms in such a cluster is not arbitrary but follows a particular geometrical regularity. The fullerenes are spheroids with the facets forming pentagons and hexagons. As

Fig. 10.21 Structure of the fullerene molecule C_{60}

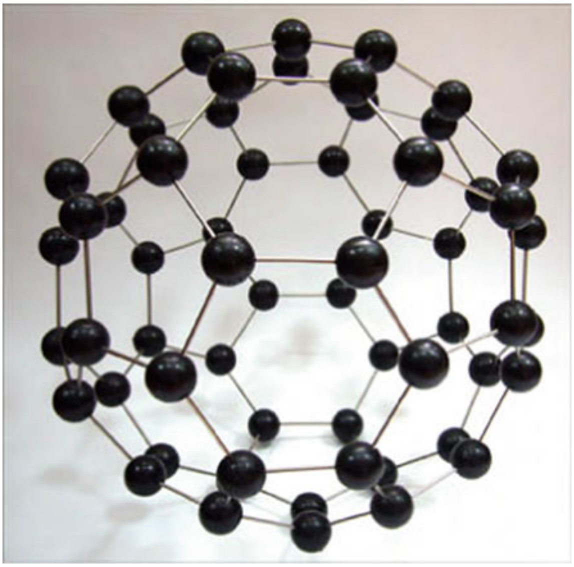

Fig. 10.21 shows, carbon atoms locate themselves on the surface of the spheroid, at the vertexes of the pentagons and the hexagons. Fullerene C_{60} was discovered as a result of experiments by Kroto and Smalley [26] designed to simulate the interstellar medium. Irradiating the surface of a graphite target with a high-power laser beam and using a mass spectrometer, he found a large peak corresponding to the mass of 60 carbon atoms. The structure was identified as a truncated icosahedron and named Buckminsterfullerene (fullerene) in honor of the famous architect. It was noted that its curvature (in comparison with the planar structure of a graphene layer) results from the introduction of pentagonal rings.

Later, a small peak corresponding to a mesh of 70 carbon atoms was identified. Later still, C_{60} started to be produced in macroscopic quantities in a crystal form. Further on, it became clear that graphite can produce a family of the structures referred to as *fullerenes*. According to a geometrical calculation made by Euler long ago, the construction of such a polyhedron requires the number of pentagonal facets to be twelve, while the number of hexangular facets is arbitrary. This condition is met by clusters with the number of atoms $N = 32, 44, 50, 58, 60, 70, 72, 78, 80, 82, 84$, etc. Experimental research is particularly interested in fullerene C_{60} due to its greatest stability and high symmetry.

10.2.8 Onion-like Carbon Structures

Core–shell nanoscale particles, i.e., particles with onion-like carbon shells surrounding a non-carbon core, are very interesting in terms of future practical applications [27]. The carbon layers can protect (from external adverse effects) a nanoscale core that is physically and chemically active. For example, the core can be protected from oxidization and from sorption of foreign substances. A nanoscale core can have physical properties considerably different from those of the bulk material. The shell material, i.e., the graphite-like layers, is ecologically safer and often more *biologically compatible* than many other materials. Materials composed of core–shell particles, aka. “core–shells”, can be used in magnetic fluids [28], as contrast substances for NMR analysis [29], and as substances for ultra-dense magnetic recording of information [30].

Core–shell materials can be produced by *high-energy* methods, e.g., the method of arc discharge between metal-containing electrodes [31, 32], or the laser-ablation method, including metallocene powders ablation [33]. A promising core–shell production method involves the use of closed containers and over-pressures [27].

Significantly, such a core–shell particle should be considered not as just a *mixture* of components, but as a *single* physicochemical system where the mutual influence between the phases results in the successful attainment of a particular goal.

10.3 Theoretical Behavior of Post-like Field Emitters

10.3.1 Field Emission Theory in Brief

At present, there is no single general theory of field emission from different materials. Thus, the functioning of each different type of FE cathode is described via a physical and mathematical model of the cathode. As of now, the best developed form of FE theory relates to the emission of electrons from smooth, planar metal surfaces. This theory derives primarily from the work of Fowler and Nordheim (FN) [34, 35] and Murphy and Good (MG) [36], with some later improvements, especially in the last ten years, as described in Chaps. 8 and 9 earlier. (For recent textbook accounts of FE theory, see [2, 37].)

These treatments are far from complete, even for metals. Strictly, they do not exactly apply to semiconductors or to carbon materials, and they do not exactly apply to sharply curved emitters of any kind. However, a common practice among experimentalists is to use the planar-metal-surface formulae to estimate the behavior of FE from semiconductors and carbon-related materials, making appropriate assumptions and allowances. This kind of approach is to be treated as a useful first approximation. Essentially, it is a compromise between a strict physical model, an adequately selected calculation method, and the possibility of obtaining a result in the simplest way and in an analyzable form. Thus, we shall base our calculations below on the zero-temperature FE equation derived by Murphy and Good (MG).

Real field emitters have curved surfaces, and both the local electrostatic field E and the magnitude J of the local emission current density vary with position $\boldsymbol{s}$ on the emitter surface. Strictly, the mathematical form of the potential-energy barrier differs for planar and curved surfaces, but we shall make the usual approximation of taking the barrier at any location $\boldsymbol{s}$ to be that for a planar emitter subject to a field $E(\boldsymbol{s})$, where $E(\boldsymbol{s})$ is the classical electrostatic field at location $\boldsymbol{s}$.

In the coordinate system normally used (as in Sects. 10.3.3 and 10.3.4 below, but not in Sect. 10.3.2), field electron emission occurs in the positive z-direction, and FE occurs when the classical field $E(\boldsymbol{s})$ is negative. Thus, we shall write the Murphy–Good (MG) FE equation for the magnitude $J(\boldsymbol{s})$ of local emission current density at location $\boldsymbol{s}$ in the form

$$J(s) = A|E(s)|^2 \exp[-B/|E(s)|], \tag{10.1a}$$

where the quantities A and B are given by

$$A = t^{-2}(f) a_{\mathrm{FN}} \phi^{-1},\ B = v(f) b_{\mathrm{FN}} \phi^{3/2}. \tag{10.1b}$$

Here, a_{FN} and b_{FN} are the Fowler–Nordheim (FN) constants, as usually defined (e.g., [38]); ϕ is the local work function; f is the operating value of scaled field, being given by $f = (e^3/4\pi\varepsilon_0)\phi^{-2}|E| \cong (1.439965\ \mathrm{eV}^2\ (\mathrm{V/nm})^{-1}]\phi^{-2}|E|$ (where ε_0 is the vacuum electric permittivity and e is the elementary positive charge); and $v(f)$ and

$t(f)$ are particular values of the field emission special mathematical functions $v(x)$ and $t(x)$ (e.g., [39]), obtained by setting $x = f$.

The magnitude I of the total emission current is obtained by integrating (10.1a) over the surface of the curved emitter. A parameter S_{em} that is a measure of the emission area is obtained by writing the result in the form shown in (10.2):

$$I = \int J(r)\,\mathrm{d}S = J_{\mathrm{a}} S_{\mathrm{em}}. \tag{10.2}$$

where J_{a} is the magnitude of the apex local current density. This parameter S_{em} is sometimes called the *notional emission area* (as derived by using the MG zero-T equation).

Strictly speaking, the theory above is exactly applicable only at the temperature $T = 0$ K. However, since small changes in temperature cause only small changes in the distribution of electrons in the metal, and change the electron supply function at the Fermi level by only about $k_{\mathrm{B}}T$ (where k_{B} is the Boltzmann constant), the formulae of the zero-T theory remain qualitatively adequate at temperatures such that $k_{\mathrm{B}}T \ll \phi$. For example, at room temperature, $k_{\mathrm{B}}T = 26$ meV, whereas a typical work-function value for carbon compounds is $\phi = 4.6$ eV; thus, the condition is well satisfied. Fuller discussions of how temperature affects emission can be found in [36, 37, 40].

10.3.2 The Almazov–Egorov Model: The Single-Emitter Case

The specific properties of different carbon-based materials mean that it is important to be able to optimize the cathode and system geometry appropriately, in order to achieve emission efficiency and the possibility of drawing a large peak field emission current. From the theoretical point of view, this problem comes down to calculation of the optimum cathode structure, and then making practical recommendations to experimental technologists on the basis of the calculation results. An approach of this kind was developed by Egorov and Almazov [41], by making using of slender-body theory [42]. The treatment here follows that in Sect. 7.2 of our textbook [1], recently translated into English [2], but with some differences in notation and some changes in presentation.

Firstly, let us consider an emission system consisting of a FE cathode represented by an axially symmetrical tip of arbitrary shape and a system of electrodes, viz. an anode, grids, etc., as depicted in Fig. 10.22. In such a system, the (total) classical electrostatic potential $\Phi(r, z)$ satisfies the Laplace equation

$$\Delta\Phi = 0, \tag{10.3}$$

with the boundary conditions

$$\Phi|_C = \Phi_C,\ \Phi|_{\mathrm{A}} = \Phi_{\mathrm{A}} \tag{10.4}$$

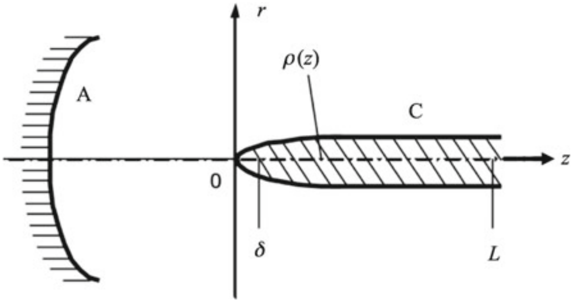

Fig. 10.22 "Slender-body" model o0m. "A" labels the anode surface, "C" the cathode surface. The electrostatic potentials are Φ_A at the anode, Φ_C at the cathode, with $\Phi_A \gg \Phi_C$. Cylindrical coordinates (r, z) are being used, and the emitter apex "a" is placed at (0,0). For explanation of other labels, see text. In this diagram, due to the orientation of the emitter relative to the coordinate axes, field electron emission takes place in the negative z-direction, at a classical field value that is positive

Here, "A" labels the anode and "C" the cathode, "$|_A$" labels a value taken at the anode surface and "$|_C$" a value taken at the cathode surface, Φ_A is the electrostatic potential of the anode and Φ_C the potential of the cathode. The related classical electrostatic field is given by the usual formula $\boldsymbol{E} = -\,\mathbf{grad}\Phi$. The most important characteristic of such systems is the value $\boldsymbol{E}_a$ of $\boldsymbol{E}$ at the tip apex. Except in various special cases, there are no good analytical expressions for $\boldsymbol{E}_a$, because its value depends on the geometrical shape of the field emitter, and (in some cases) on the whole system geometry.

For practical applications, thin needle-like emitters are the most interesting. In such problems, a small parameter arises, namely the ratio of the needle radius to the emitter's typical longitudinal dimension. To study such emitters, it is sufficient to expand the electrostatic potential Φ as an asymptotic series in the vicinity of an *ideally thin* emitter. The first few terms of this series will allow us to calculate the field intensity in quite a precise way.

To construct an asymptotic expansion of this kind, let us apply the following approach. Consider the axially symmetric system shown in Fig. 10.22, where r, z are cylindrical coordinates. Using the modern international system of quantities and equations, in which charge is measured in coulombs, let a line-charge of linear density $\sigma(z)$ be located along the z-axis, between $z = \delta$ and $z = L$, but for notational simplicity, let the symbol $\rho(z)$ denote the quantity $\sigma(z)/4\pi\varepsilon_0$. Let us represent the sought-for solution as the sum of three contributions

$$\Phi(r, z) = \Phi_0(r, z) + \Phi_1(r, z) + \Phi_2(r, z), \qquad (10.5)$$

where Φ_0 is given in terms of a line-charge representing the needle, via

$$\Phi_0(r, z) = \int\limits_{\delta}^{L} \frac{\rho(z')}{\sqrt{r^2 + (z - z')^2}} \mathrm{d}z', \tag{10.6}$$

where z' is a dummy variable related to z. We now choose the functions Φ_1 and Φ_2 to meet the following requirements:

$$\Delta\Phi_1 = 0, \quad \Phi_1|_{\mathrm{A}} = \Phi_{\mathrm{A}}, \tag{10.7a}$$

$$\Delta\Phi_2 = 0, \quad \Phi_2|_{\mathrm{A}} = -\Phi_0|_{\mathrm{A}}, \tag{10.7b}$$

and note that the function Φ_2 can be represented as

$$\Phi_2(r, z) = \int\limits_{\delta}^{L} u_2(r, z; z')\rho(z')\mathrm{d}z', \tag{10.8}$$

where the function $u_2(r, z; z')$ is defined via the Green's function for problem (10.6), namely

$$u_2(r, z; z') = -4\pi\varepsilon_0 G(r, z; 0, z') - [(r^2 + (z - z')^2]^{-1/2}. \tag{10.9}$$

It is obvious that (10.5) satisfies the Laplace equation and the boundary conditions at the anode "A". Our aim is to select the line-function $\rho(z)$ in such a fashion that the physical tip surface, as represented by a function $r_{\mathrm{C}}(z)$, coincides with the equipotential surface (of the total potential Φ) that has the value Φ_{C}. Having selected $\rho(z)$ in this way, we will be able to meet the boundary conditions (10.4) and find values for the apex field E_{a} and the emission area S_{em} we are interested in.

As we are only interested in thin emitters, it is sufficient to study the equipotential surfaces of the model potential (10.5) that are located near the emitter axis. Let us thus resort to asymptotic expansion [43] of the potential near the emitter axis:

$$\begin{aligned} \Phi|_{\substack{r\to 0 \\ \delta<z<L}} &= \rho(z) \ln \frac{2(L - z)}{\delta - z + \sqrt{r^2 + (\delta - z)^2}} + \int\limits_{\delta}^{L} \frac{\rho(\xi) - \rho(z)}{|\xi - z|} \mathrm{d}\xi \\ &\quad + \Phi_1(0, z) + \Phi_2(0, z). \end{aligned} \tag{10.10}$$

Taking (10.10) into account, the equipotential surface close to the tip axis follows the relation

$$\rho(z) \ln \frac{2(L - z)}{r_{\mathrm{C}}(z)} + \int\limits_{\delta}^{L} \frac{\rho(\xi) - \rho(z)}{|\xi - z|} \mathrm{d}\xi + \Phi_1(0, z) + \Phi_2(0, z) = \Phi_{\mathrm{C}}, \tag{10.11}$$

where $r_{\mathrm{C}}(z)$ is the function that describes the cathode shape. Since this shape is known, (10.11) is an equation for determining $\rho(z)$ and hence the line-charge density $\sigma(z)$.

Equation (10.11) includes the parameter δ, which is still unknown. Let us define it from the condition that $\Phi(0, 0) = \Phi_{\mathrm{C}}$, i.e., we take the tip apex at the origin of coordinates. Let us underscore that for a thin tip, the value of δ should be small. In this case, the condition $\Phi(0, 0) = \Phi_{\mathrm{C}}$ can be represented as [44]

$$\Phi_{\mathrm{C}} = \rho(\delta)\ln\frac{L}{\delta} + \int\limits_{\delta}^{L}\frac{\rho(\xi)-\rho(\delta)}{\xi}\mathrm{d}\xi + \Phi_1(0,0) + \Phi_2(0,0). \tag{10.12}$$

Another relation is found by putting $z = \delta$ in (10.11), which yields

$$\Phi_{\mathrm{C}} = \rho(\delta)\ln\frac{2(L-\delta)}{r_{\mathrm{C}}(\delta)} + \int\limits_{\delta}^{L}\frac{\rho(\xi)-\rho(\delta)}{|\xi-\delta|}\mathrm{d}\xi + \Phi_1(0,\delta) + \Phi_2(0,\delta). \tag{10.13}$$

Comparison of (10.12) and (10.13) demonstrates that the relation $\ln(L/\delta) = \ln\{2(L–\delta)/r_{\mathrm{C}}(\delta)\}$ should be true within the accuracy up to the terms vanishing as $\delta \to 0$, from which we can obtain the following equation for the value of δ:

$$2\delta = r_{\mathrm{C}}(\delta). \tag{10.14}$$

Near the tip apex, for any smooth tip shape, the function r_{C}^2 can be written as

$$r_{\mathrm{C}}^2(z) = 2R_{\mathrm{a}}z + \mathrm{O}\left(z^2\right), \tag{10.15}$$

where R_{a} is the tip's apex radius-of-curvature. We assume that the tip is smooth enough at the apex. Moreover, we will consider that the condition $r_{\mathrm{C}}^2(\delta) = 2R_{\mathrm{a}}\delta[1 + \mathrm{O}(\delta)]$ has been met. Substituting into (10.14) leads to the result:

$$\delta = R_{\mathrm{a}}/2. \tag{10.16}$$

If condition (10.15) is met, then (10.11) can be simplified. Let us underscore that if $z \gg \delta$, then

$$\frac{2(L-z)}{\delta - z + \sqrt{r_{\mathrm{C}}^2(z) + (\delta - z)^2}} = \frac{4z(L-z)}{r_{\mathrm{C}}^2(z)}\left(1 + \mathrm{O}\left(\frac{r_{\mathrm{C}}^2(z)}{z^2}\right) + \mathrm{O}\left(\frac{\delta}{z}\right)\right). \tag{10.17}$$

Further, if z and δ are of the same order, then the two expressions $2(L - z)\left(\delta - z + \sqrt{r_{\mathrm{C}}^2(z) + (\delta - z)^2}\right)^{-1}$ and $4z(L - z)r_{\mathrm{C}}^{-2}(z)$ coincide in higher order as $\delta \to 0$, and are roughly equal to $2L/R_{\mathrm{a}}$. As a result, (10.11) can be reformulated as

$$\rho(z)\ln\frac{4z(L-z)}{r_{\mathrm{C}}^2(z)}+\int\limits_{\delta}^{L}\frac{\rho(\xi)-\rho(z)}{|\xi-z|}\mathrm{d}\xi+\int\limits_{\delta}^{L}u_2(0,z;\xi)\rho(\xi)\mathrm{d}\xi=\Phi_{\mathrm{C}}-\Phi_1(0,z). \tag{10.18}$$

Using (10.18), let us construct the desired expansion for ρ(z). To this effect, it is sufficient to seek solution of (10.18) as an iterative series. Iterating (10.18), we can obtain the solution in the form

$$\rho(z)=\sum_{k=0}^{\infty}\rho_k(z), \tag{10.19}$$

$$\rho_0(z)\;=\;\frac{\Phi_{\mathrm{C}}-\Phi_1(0,z)}{\ln[4z(L-z)r_{\mathrm{C}}^{-2}(z)]}\approx\frac{\Phi_{\mathrm{C}}-\Phi_1(0,z)}{\ln[2L/R_a]}, \tag{10.20}$$

$$\rho_{k+1}(z)=-\left(\ln\frac{4z(L-z)}{r_{\mathrm{C}}^2(z)}\right)^{-1}\left[\int\limits_{\delta}^{L}\frac{\rho_k(\xi)-\rho_k(z)}{|\xi-z|}\mathrm{d}\xi+\int\limits_{\delta}^{L}u_2(0,z;\xi)\rho_k(\xi)\mathrm{d}\xi\right], \tag{10.21}$$

where the second form in (10.20) uses (10.15), but is valid only near the emitter apex. In fact, the iterative series seems to be asymptotic for thin tips.

With coordinate axes and electrostatic potentials defined as in Fig. 10.21, the classical electrostatic field E is regarded as positive if a positive test charge moves to the right, or if an electron moves to the left. In this system, therefore, field electron emission (FE) is characterized by a positive value of E, but by a negative value of $\rho(z)$. Knowing the function $\rho(z)$, it is not difficult to find an expression for the field value E_{a} at the tip apex. Using (10.5) and 10.6), we can express E_{a} as

$$E_{\mathrm{a}}=-\left.\frac{\partial\Phi}{\partial z}\right|_{\substack{z=0\\r=0}}=-\int\limits_{\delta}^{L}\frac{\rho(\xi)}{\xi^2}\mathrm{d}\xi-\left.\frac{\partial}{\partial z}(\Phi_1+\Phi_2)\right|_{\substack{z=0\\r=0}}. \tag{10.22}$$

For thin emitters, the main contribution to (10.22) is given by the first term. Calculating the integral asymptotically as $\delta\to 0$, we find the apex field value as

$$E_{\mathrm{a}}\approx-\rho(\delta)/\delta=\,-2\rho(\delta)/R_{\mathrm{a}}. \tag{10.23}$$

Adjustments to (10.23), necessary in principle, can be shown to vanish as $\delta\to 0$.

Using (10.20) in (10.23), with $z=\delta$, gives a zero-order approximation for the emitter apex field, namely

$$E_a^{(0)}\;\approx\;-\frac{\Phi_{\mathrm{C}}-\Phi_1(0,\delta)}{k_0^{(0)}R_{\mathrm{a}}}\;\approx\;-\frac{\Phi_{\mathrm{C}}-\Phi_1(0,0)}{k_0^{(0)}R_{\mathrm{a}}}, \tag{10.24}$$

since it is safe to assume that Φ_1 is slowly varying near (0, 0). The constant $k_0^{(0)}$ is a zero-order estimate of a parameter k_0, and is given by

$$k_0^{(0)} = \frac{1}{2} \ln \frac{2L}{R_\mathrm{a}}. \tag{10.25}$$

However, expression (10.25) gives a wrong result for k_0 when L is large. Formulas (10.23) and (10.24) predict that as $L \to \infty$, then $E_\mathrm{a} \to 0$; however, it is obvious that in the limit of $L \to \infty$, we should have $E_\mathrm{a} \to \mathrm{const} \neq 0$. So the construction of a correct expression for k_0 needs the involvement of a term $\rho_1(z)$ of form (10.21).

Having inserted $\rho_0(z) + \rho_1(z)$ in (10.23), setting $z = \delta$, we find a first-order approximation $k_0^{(1)}$ as

$$k_0^{(1)} = \frac{1}{2} \ln \frac{2L}{R_\mathrm{a}} \left[1 - \frac{1}{\Phi_\mathrm{C} - \Phi_1(0,\delta)} \int\limits_{\delta}^{L} \mathrm{d}\xi \left(\frac{\rho_0(\xi) - \rho_0(\delta)}{\xi} + u_2(0,\delta;\xi)\rho_0(\xi) \right) \right]^{-1}. \tag{10.26}$$

For a slender emitter, the integral in square brackets is small because the value of $\rho_0(\xi)$ is small. Therefore, when δ approaches (but does not reach) 0, (10.23) can be written

$$k_0^{(1)} \approx \frac{1}{2} \ln \frac{2L}{R_\mathrm{a}} \left[1 + \frac{1}{\Phi_\mathrm{C} - \Phi_1(0,0)} \int\limits_{\delta}^{L} \mathrm{d}\xi \left(\frac{\rho_0(\xi) - \rho_0(\delta)}{\xi} + u_2(0,0;\xi)\rho_0(\xi) \right) \right] + \cdots. \tag{10.27}$$

Using (10.20), with $z = \xi$, and assuming that $\rho_0(0) = 0$, we can transform (10.27) into

$$k_0^{(1)} \approx \frac{1}{2} \ln \frac{2L}{R_0} \int\limits_{\delta}^{L} \mathrm{d}\xi \left[\ln \frac{4\xi(L-\xi)}{r_\mathrm{C}^2(\xi)} \right]^{-1} \frac{\Phi_\mathrm{C} - \Phi_1(0,\xi)}{\Phi_\mathrm{C} - \Phi_1(0,0)} \left(\frac{1}{\xi} + u_2(0,0;\xi) \right). \tag{10.28}$$

On assuming that most of the contribution to the integral comes from the region of z where the emitter apex is quasi-spherical, where (10.15) applies, and that Φ_1 is slowly varying in this region, (10.28) reduces to

$$k_0^{(1)} \approx \frac{1}{2} \ln \frac{2L}{R_\mathrm{a}} \left[\int\limits_{\delta}^{L} \left[\ln \frac{2(L-\xi)}{R_\mathrm{a}} \right]^{-1} \frac{\mathrm{d}\xi}{\xi} + \int\limits_{\delta}^{L} \left[\ln \frac{2(L-\xi)}{R_\mathrm{a}} \right]^{-1} u_2(0,0;\xi)\mathrm{d}\xi \right]. \tag{10.29}$$

The leading term in the result for the first integral can be evaluated analytically, but evaluation of the second integral can be difficult in arbitrary system geometry, because a suitable representation needs to be found for $u_2(0, 0; \xi)$.

As an example, let us consider a system consisting of an emitter shaped as a thin ellipsoid of revolution and an anode represented by an infinite plane located at distance D from the tip apex. Let the anode potential be zero. In this case,

$$u_2(0, 0; \xi) = -(2D + \xi)^{-1}. \tag{10.30}$$

The related integrals in (10.29) can be calculated accurately. For the factor $k_0^{(1)}$, we obtain

$$k_0^{(1)} \approx \frac{1}{2} \ln \frac{4LD}{R_\mathrm{a}(2D + L)}. \tag{10.31}$$

For $L \ll D$, expression (10.31) turns into (10.25). For $L \gg D$, the factor becomes that for a hyperboloid of revolution.

In both field ion and field electron emission, experiments that aim to find the emitter apex field are often discussed with the aid of *Gomer's formula* $|E_\mathrm{a}| = |V_\mathrm{a}|/(k_G R_\mathrm{a})$ [45], where V_a is the applied voltage between anode and cathode, R_a is the emitter apex radius, and k_G is a geometrical factor (sometimes called the *shape factor*) that is often taken as about 5 in traditional field electron microscope geometry. In our theory (neglecting the difference between voltage and "difference in classical electrostatic potential", which is always small in practice), the equivalent formula would be

$$E_\mathrm{a} \approx \frac{\Phi_\mathrm{A} - \Phi_\mathrm{C}}{k_\mathrm{G} R_\mathrm{a}}. \tag{10.32}$$

The physical reason for the difference between k_G and k_0 is that Gomer's formula is an empirical formula that automatically takes into account effects due to charge on all other surfaces in the system, as well as charge on the needle, whereas our approach concentrates on effects due to the charge on the needle. The needle contribution is the largest contribution in most experimental circumstances, and probably is often the dominant contribution.

We also note that the literature (e.g., [46, 47]) does contain formulas for the field-enhancement factor associated with a hemi-ellipsoid of height h on one of a pair of widely separated (by distance l) parallel planar plates. These formulas lead to the following expression for the Gomer-type shape factor for this configuration:

$$k_\mathrm{G} \approx \frac{l}{h} \times \left(\frac{1}{2} \ln \frac{4h}{R_\mathrm{a}} - 1 \right) \approx \frac{l}{h} \times \left(\frac{1}{2} \ln \frac{4h}{R_\mathrm{a}} \right) \tag{10.33}$$

where the second form applies if $l \gg R_\mathrm{a}$, which will usually be the case in practice.

Since $h \cong L$, this formula differs from our (10.25) by having a factor “4”, rather than “2”, in the logarithm, and a dimensionless factor (l/h) outside the logarithm. The physical situation to which (10.33) applies is different from ours, so exact equivalence of the expressions is not to be expected, but it remains a matter for future research as to precisely how the differences between the two expressions arise.

Whatever the precise approach used to predict a value of the apex field E_a, we can use this value to estimate the total current and the emission area (S_em), using (10.1a) and (10.2) above. For $\phi = 4.5$ eV, B is typically around 40 V/nm and E_a is typically around 4 V/nm, so the condition $B \gg E_0$ is satisfied. It follows that integral (10.1) can be calculated asymptotically by the Laplace method [48], yielding

$$I = -\frac{2\pi A E_\text{a}^4}{B E''_{rr}(0,0)} \exp\left(-\frac{B}{E_\text{a}}\right). \tag{10.34}$$

This formula is the basis for the emission-area expression:

$$S_\text{em} = I J_\text{a}^{-1} = -\frac{2\pi E_\text{a}^2}{B E''_{rr}(0,0)}. \tag{10.35}$$

Using model potential (10.5), it is not difficult to calculate the value of $-E''_{rr}(0)$. However, the resulting expression looks cumbersome. As $\delta \to 0$, i.e., for a slender emitter, and taking (10.16) and (10.23) into account, (10.35) is essentially reduced to

$$S_\text{em} = (2\pi R_\text{a}^2/B) \cdot E_\text{a}. \tag{10.36}$$

The linear dependence of emission area on the apex field value was stated in several papers, e.g., [49–51]. However, they did not determine the coefficient of proportionality for that dependence.

10.3.3 The Almazov–Egorov Model: The Regular Emitter Array

A procedure similar to that above can be applied to a multi-tip periodic system. In particular, it can be applied to the system where a regular array of identical emitters stands on a common, planar “cathode base-plate”, as illustrated (for a square array) in Fig. 10.23, and the anode is a distant plate parallel to the cathode base-plate, a distance l away from it. In this context, it is easier to use the common system of coordinates, used in Fig. 10.23, in which electron emission takes place in the positive z-direction, at values of classical electrostatic field that are negative in value. In this case, one takes the origin of coordinates at the location where the axis of a “central”

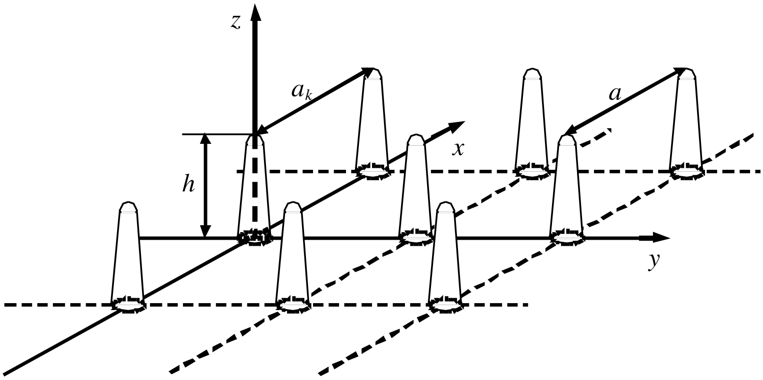

Fig. 10.23 Model of a regular, square multi-emitter array. The squares have sides of length a, and the emitter height is h. Distance z is measured from the base-plane

emitter intersects the base-plane, and defines a "field point" by a three-dimensional vector ($\boldsymbol{r}$,z) where $\boldsymbol{r}$ is a two-dimensional vector in the plane of the base-plate.

For electrostatic consistency, the images of the emitters in the base-plate need to be taken into account. Thus, at a field point above the base-plane, the classical electrostatic potential $\Phi(\boldsymbol{r},z)$ has to be taken as defined by

$$\begin{aligned}
&\Phi(\mathbf{r}, z) = -E_{\mathrm{M}} z + \int\limits_{-h+\delta}^{h-\delta} \mathrm{d}\xi \cdot \rho(\xi) \sum_k \frac{1}{\sqrt{|\mathbf{r} - \mathbf{a}_k|^2 + (z-\xi)^2}}, \\
&\rho(-z) = -\rho(z),
\end{aligned} \tag{10.37}$$

where E_{M} is the "macroscopic" classical electrostatic field E_∞ value far from the cathode; h is the emitter height; $\boldsymbol{a}_k$ is the vector connecting the origin of coordinates to the point where the axis of the kth tip intersects the base-plane; $a_k = |\boldsymbol{a}_k|$; and ξ is a dummy variable associated with the coordinate z. Note that, in the array case, the line-function $\rho(z)$ has values different from the single-emitter case, and that these values depend on the array geometry.

Having made calculations as above, one can be sure that the field value E_{a}^* at the emitter apex is determined by an expression analogous to (10.23) in this case too, i.e.,

$$E_{\mathrm{a}}^* = \frac{2 \cdot \rho(h - R_{\mathrm{a}}/2)}{R_{\mathrm{a}}}. \tag{10.38}$$

However, the line-function $\rho(z)$ [$\equiv \sigma(z)/4\pi\varepsilon_0$] now satisfies a different equation, namely

$$\rho(z)\ln\frac{4(h^2-z^2)}{r_{\mathrm{C}}^2(z)} + \int\limits_{-h+R_{\mathrm{a}}/2}^{h-R_{\mathrm{a}}/2} \mathrm{d}z' \left[\frac{\rho(z')-\rho(z)}{|z'-z|} + \sum_{\substack{k\\ k\neq 0}} \frac{\rho(z')}{\sqrt{a_k^2+(z-z')^2}}\right] - E_{\mathrm{M}} z \cong \Phi(r_{\mathrm{C}}(z), z) = \Phi_{\mathrm{C}} = 0, \tag{10.39}$$

where the sum applies to all emitters except the central one ("$k = 0$") located at the origin of coordinates. The first two terms in this expression are an asymptotic approximation for the classical electrostatic potential due to a line-charge representing the central emitter; the summation term gives the potential contribution due to all the other emitters; and the term involving E_{M} represents the potential contribution due to the macroscopic field. In the limit that $r_{\mathrm{C}}(z) \to 0$, the sum of these contributions becomes equal to the cathode potential, which is taken to be zero.

Result (10.38) can also be used to define an *apex field enhancement factor* β for this array case, by

$$\beta = \frac{E_{\mathrm{a}}^*}{E_{\mathrm{M}}} = \frac{2\cdot\rho(h-R_{\mathrm{a}}/2)}{E_{\mathrm{M}} R_{\mathrm{a}}} \tag{10.40}$$

It is not difficult to verify that the emission area for an individual emitter is given by (10.26) in both a multi-emitter system and the single-emitter case (but with E_{a} replaced by E_{a}^* in the multi-emitter case). However, it should be noted that research into the related asymptotic expansion for (10.39) is difficult when studying multi-emitter systems because: on the one hand, the asymptotic expansion parameter $[\ln(4\,h/R_{\mathrm{a}})]^{-1}$ can be insufficiently small for such real systems; on the other hand, even the second term of the series considered is rather cumbersome, which prevents efficient research. Therefore, multi-emitter systems are more conveniently studied directly with (10.39). The approximate solution of this equation seems to be equivalent to the approximate summation of the asymptotic series generated by this equation.

Let us note that the numerical solution of (10.39) needs some caution, because its second term is a singular-nucleus integral, which may cause the computing loop to lose stability.

For numerical computation, we selected a system consisting of hemi-ellipsoidal emitters located at the nodes of a flat square grid with node-spacing a (see Fig. 10.23). The equation was solved with the Ritz method [52], the solution having been sought-for as odd polynomials to the $2N$–1 degree. The focus of the research was on calculating the *depolarization factor* ν [$\equiv\beta/\beta_0$], where β_0 is the apex FEF for a single isolated emitter, and investigating how this factor depends on the *height-to-spacing ratio* (*H/S ratio*) h/a, for emitters with different apex radii R_{a}.

In some contexts, the inverse ratio (or *packing parameter*) a/h is more useful. The numerical computation showed that solution stability was lost even for $N = 4$, for $a/h > 0.5$. For $N > 4$, stability was lost at even less close-packed emitter arrangements. But for $N = 2$ and $N = 3$, the numerical method worked well, even at $a/h \sim 1$, and produced results differing by about 5% at the worst. The computation results are shown in Fig. 10.24. One can see that the tips begin depolarizing each other at a/h

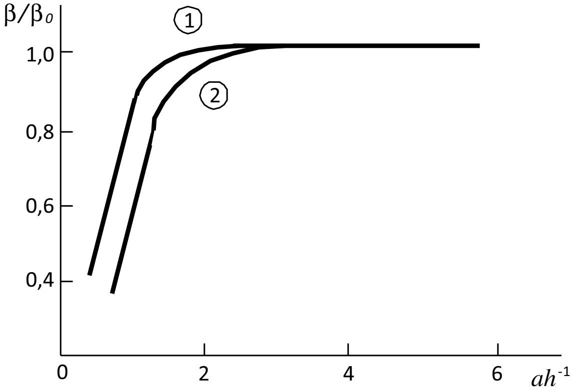

Fig. 10.24 To illustrate how the depolarization ratio β/β_0 depends on the ratio *a*/*h*, for a regular, square multi-emitter array. For curve 1, $(h/R_a) = 100$ and $\beta_0 = 50.1$; for curve 2, $(h/R_a) = 50$ and 30.3. For explanation of symbols, see text

~ 3. If the tips are even more close-packed, the field-enhancement factor plummets down. The computation results suggest that tip packaging closer than *a*/*h* ~ 3 to 4 is not efficient. This result, originally found by Egorov and Almazov [41], is similar to that found later by other authors (e.g., [53]), using a different emitter model (which, however, suggested a "most efficient" value of around *a*/*h* ~ 2 to 2.5).

In the case of a single isolated emitter in this system geometry, the apex field enhancement factor β_0 would be given by a formula similar to (10.40), but with $\rho(h–R_a/2)$ replaced by $\rho_0(h–R_a/2)$, where $\rho_0(z)$ is the line-function appropriate to the case of a single isolated emitter. Hence, it can be seen that the depolarization factor ν is given by

$$\nu \cong \beta \big/ \beta_0 = \rho(h - R_a/2) \,/ \rho_0(h - R_a/2). \tag{10.41}$$

This result is broadly similar to that obtained in the simplified version of the "floating sphere at emitter plane potential" (FSEPP) model, as discussed recently [54], where a result is obtained that could be put in the form

$$\beta \big/ \beta_0 = q \big/ q_0, \tag{10.42}$$

where q_0 is the charge at the center of the floating sphere in the isolated-single-emitter case, and q is the (reduced) charge in the array case. The underlying physics is, of course, the same in both treatments because electron thermodynamics requires that the Fermi level must be constant throughout the cathode, the electrostatic-potential change at each emitter apex, as the emitters are brought closer together, forces electron charge to be withdrawn from the emitter apex into the substrate, thereby returning the apex electrostatic potential to its original value (characteristic of well-separated emitters), but also reducing the magnitude of the apex field.

In the array case, the total current I_1 from each emitter in the array is given by

$$I_1 = S^*_{\text{em}} J^*_{\text{a}} \tag{10.43}$$

where the apex current density J_{a}^{*} for the array case follows (10.1a), but with the field set equal to the "reduced" apex field E_{a}^{*}, and the "reduced" emission area S_{em}^{*} given by

$$S_{\mathrm{em}}^{*} = (2\pi R_{\mathrm{a}}^{2}/B)\,E_{\mathrm{a}}^{*}. \tag{10.44}$$

10.3.4 Optimizing Multi-emitter Systems

This Section considers the problem of how to maximize the macroscopic (or "array average") current density J_{M} (i.e., the magnitude of the total emission current per unit area of the array base-plane), for a multi-emitter array.

Consider a multi-emitter system as described above and illustrated in Fig. 10.23. Let the anode–cathode separation be l. Take the electrostatic potential of the cathode as zero, and that of the anode as $\Phi_{\mathrm{A}} = -E_{\mathrm{M}}l$, where E_{M} is the uniform, "macroscopic", classical electrostatic field between the plates. In the system shown in Fig. 10.23, field electron emission occurs when Φ_{A} is positive and E_{M} is negative. Emission currents to be considered are at a level where associated space-charge effects are negligible.

To optimize a multi-emitter system, it is necessary to know how the apex field E_{a}^{*} depends on the H/S ratio h/a. Let us consider the different terms of (10.39). To that end, introduce some new notations, namely

$$h_{\mathrm{r}} = (h - R_{\mathrm{a}}/2);\ \xi = z/h_{\mathrm{r}};\ \xi' = z'/h_{\mathrm{r}}; \tag{10.45}$$

$$\tilde{\rho}(\xi) = \frac{\rho(z)}{E_{\mathrm{M}}h_{\mathrm{r}}};\ \tilde{\rho}(\xi') = \frac{\rho(z')}{E_{\mathrm{M}}h_{\mathrm{r}}};\quad S_{k} = a_{k}/a;\quad \mu = h_{\mathrm{r}}/a \approx h/a. \tag{10.46}$$

Taking into account that for an ellipsoidal apex

$$\ln\frac{4(h^{2} - z^{2})}{r_{\mathrm{C}}^{2}(z)} = \ln\frac{4h}{R_{\mathrm{a}}}, \tag{10.47}$$

substitution into (10.39) gives

$$\tilde{\rho}(\xi)\ln\frac{4h}{R_{0}} + K_{1}(\tilde{\rho}(\xi)) + K_{2}(\tilde{\rho}(\xi)) = \xi, \tag{10.48}$$

where K_{1}, K_{2} are given by

$$K_{1}[\tilde{\rho}(\xi)] = \mu\sum_{\substack{k\\ k\neq 0}}\int_{-1}^{+1}\frac{\tilde{\rho}(\xi')d\xi'}{\sqrt{S_{k}^{2} + \mu^{2}(\xi - \xi')^{2}}},$$

$$K_2[\tilde{\rho}(\xi)] = \int\limits_{-1}^{1} \frac{\tilde{\rho}(\xi') - \tilde{\rho}(\xi)}{|\xi' - \xi|} d\xi'. \tag{10.49}$$

For K_1, we consider the expansion [42]

$$\frac{1}{\sqrt{S_k^2 + \mu^2(\xi - \xi')^2}} = \frac{1}{S_k} - \frac{1}{2}\mu^2 \frac{(\xi - \xi')^2}{S_k^3} + \frac{3}{8}\mu^4 \frac{(\xi - \xi')^4}{S_k^5} + O(\mu^6), \tag{10.50}$$

and use the property of “odd symmetry”, namely $\rho(-z) = -\rho(z)$, to obtain

$$K_1 = C_3\mu^3 \int\limits_{-1}^{1} \xi\xi'\tilde{\rho}(\xi')d\xi' - \frac{3}{2}C_5\mu^5 \int\limits_{-1}^{1} (\xi^3\xi' + \xi\xi'^3)\tilde{\rho}(\xi')d\xi' + O(\mu^7) \tag{10.51}$$

where C_3 and C_5 are coefficients determined only by the geometry of the array, by

$$C_3 = \sum_{\substack{k \\ k \neq 0}} \frac{1}{S_k^3}, \quad C_5 = \sum_{\substack{k \\ k \neq 0}} \frac{1}{S_k^5}. \tag{10.52}$$

These coefficients can be obtained numerically; for a square grid, $C_3 \cong 9.03362$, $C_5 \cong 5.09026$. It is not difficult to see that, in the context of an established formulation, K_1 is an integral operator acting on $\tilde{\rho}$ according to the rule

$$\begin{aligned} K_1[\tilde{\rho}] =& C_3\mu^3 P_1(\xi)\langle P_1 \cdot \tilde{\rho}\rangle - \frac{3}{2}C_5\mu^5\left[\frac{6}{5}P_1(\xi)\langle P_1 \cdot \tilde{\rho}\rangle + \frac{2}{5}(P_3(\xi)\langle P_1 \cdot \tilde{\rho}\rangle + P_1(\xi)\langle P_3 \cdot \tilde{\rho}\rangle)\right] \\ &+ O(\mu^7), \end{aligned} \tag{10.53}$$

where $\langle f \cdot g\rangle$ represents the scalar product of two *functions* f and g, and the functions, $P_1(\xi) = \xi$, $P_3(\xi) = 5\xi^3/2$–$3\xi/2$, are Legendre polynomials. Relevant orthogonality relations are

$$\langle P_1 \cdot P_1\rangle = \frac{2}{3}, \quad \langle P_3 \cdot P_3\rangle = \frac{2}{7}, \quad \langle P_1 \cdot P_3\rangle = 0. \tag{10.54}$$

Similarly, K_2 is an integral operator whose verifiable eigenfunctions are Legendre polynomials P_n with eigenvalues $\lambda_n = -2\sum_{k=1}^{n} k^{-1}$. Therefore, the subspace covering the polynomials P_1 and P_3 yields the relation.

$$K_2[\tilde{\rho}] = -3P_1(\xi)\langle P_1 \cdot \tilde{\rho}\rangle - \frac{77}{6}P_3(\xi)\langle P_3 \cdot \tilde{\rho}\rangle. \tag{10.55}$$

Hence, (10.48) is reduced to

$$\ln\frac{4h}{R_0}\tilde{\rho}(\xi) - 3P_1(\xi)\langle P_1\cdot\tilde{\rho}\rangle - \frac{77}{6}P_3(\xi)\langle P_3\cdot\tilde{\rho}\rangle + C_3\mu^3P_1(\xi)\langle P_1\cdot\tilde{\rho}\rangle$$
$$-\frac{3}{2}C_5\mu^5\left[\frac{6}{5}P_1(\xi)\langle P_1\cdot\tilde{\rho}\rangle + \frac{2}{5}(P_3(\xi)\langle P_1\cdot\tilde{\rho}\rangle + P_1(\xi)\langle P_3\cdot\tilde{\rho}\rangle)\right] + O(\mu^7) = P_1(\xi) \tag{10.56}$$

This equation is solved by

$$\tilde{\rho}(\xi) = \alpha P_1(\xi) + \gamma P_3(\xi), \tag{10.57}$$

where α and γ are determined by the equations

$$\begin{aligned}\left(\ln\frac{4h}{R_a} - 2 + \frac{2}{3}C_3\mu^3 - \frac{6}{5}C_5\mu^5\right)\alpha - \frac{6}{35}C_5\mu^5\gamma &= 1,\\ \left(\ln\frac{4h}{R_a} - \frac{11}{3}\right)\gamma - \frac{2}{5}C_5\mu^5\alpha &= 0.\end{aligned} \tag{10.58}$$

In any regimes where it can be assumed that terms in μ^3 and μ^5 are small in comparison with the other terms, clearly a first approximation $\alpha^{(1)}$ for α is

$$\alpha^{(1)} = \left(\ln\frac{4h}{R_a} - 2\right)^{-1}. \tag{10.59}$$

Strictly, the related first approximation for γ is $\gamma^{(1)} = 0$, but a better approximation is

$$\gamma^{(2)} = \frac{2}{5}\left(\ln\frac{4h}{R_a} - 2\right)^{-1}\left(\ln\frac{4h}{R_a} - \frac{11}{5}\right)^{-1}C_5\mu^5. \tag{10.60}$$

This result suggests that γ is small in the regime of interest. Hence, by neglecting the term γ in the first expression in (10.58), and using binomial expansion, we get a second approximation for α

$$\alpha^{(2)} = \left(\ln\frac{4h}{R_a} - 2\right)^{-2}\left(\ln\frac{4h}{R_a} - 2 - \frac{2}{3}C_3\mu^3 + \frac{6}{5}C_5\mu^5\right) \tag{10.61}$$

Since $P_1(1) = 1$ and $P_3(1) = 1$, it follows from (10.46) and (10.57) that

$$\rho(h - R_0/2) \equiv \rho(h_r) = \tilde{\rho}(1)E_M h_r = (\alpha + \gamma)E_M h_r. \tag{10.62}$$

Hence, from (10.40)

$$\beta = 2(\alpha + \gamma)\,(h_{\mathrm{r}}/R_{\mathrm{a}}). \tag{10.63}$$

The corresponding result (β_0) for the single-isolated-emitter case is found by neglecting the terms in μ, which leads to (10.59) as an expression for α_0 and then to

$$\beta_0 = 2\alpha_0(h_{\mathrm{r}}/R_{\mathrm{a}}) = 2\left(\ln\frac{4h}{R_{\mathrm{a}}} - 2\right)^{-1}(h_{\mathrm{r}}/R_{\mathrm{a}}) \equiv \kappa\cdot(h_{\mathrm{r}}/R_{\mathrm{a}}) \approx \kappa\cdot(h/R_{\mathrm{a}}), \tag{10.64}$$

where κ is a correction factor defined by this equation and given by

$$\kappa = 2\left(\ln\frac{4h}{R_{\mathrm{a}}} - 2\right)^{-1}. \tag{10.65}$$

This result coincides with the 1991 result of Kosmahl [55], using straightforward Laplace-type mathematical analysis, and with later stated formulae [46, 47]. For example, for $h/R_{\mathrm{a}} = 100$, we find $\kappa = 0.501$ and $\beta_0 = 0_0 = 50.1$.

For post-like emitters, formulas for β_0 of the form (10.64) are, of course, now well known (e.g., [46]), with a well-known suggestion [56] that, for the hemisphere-on-cylindrical-post (HCP) emitter model, κ can be adequately approximated as 0.7 over the range $30 < (h/R_{\mathrm{a}}) < 2000$, to within ± 25%. This is interestingly close to our predicted values.

Returning to the array case, we find from (10.60) to (10.64) that the related approximation for the depolarization factor ν is

$$\nu = \beta/\beta_0 = 1 - \frac{\kappa C_3\mu^3}{3} + \frac{6C_5\mu^5}{5}\left(\left(\ln\frac{4h}{R_{\mathrm{a}}} - 2\right)^{-1} + \left(3\ln\frac{4h}{R_{\mathrm{a}}} - 11\right)^{-1}\right). \tag{10.66}$$

In a large-spacing approximation that disregards the term in μ^5, the related *fractional field reduction Δ in apex field*, as a result of electrostatic depolarization, is given by

$$\Delta \equiv 1 - \nu \approx \kappa C_3\mu^3/3 \tag{10.67}$$

This result, derived by Egorov and Almazov [41] (though not in precisely this form), supports the recent assertions by de Assis and Dall-Agnoll [57, 58] that, at large array spacings, electrostatic depolarization effects fall off physically as the inverse-third power of the lattice parameter, rather than exponentially (as assumed from some numerical line-charge treatments, e.g., [59]).

Optimization of a multi-emitter system to achieve maximum value of the macroscopic ("array average") current density J_{M} needs knowledge of how J_{M} depends on the H/S ratio h/a [$\cong\mu$]. Disregarding any constant multiplicative terms, the current

I_1 from each tip in the array goes as

$$I_1 \sim \left|E_a^*\right|^3 \exp\left[-B/|E_a^*|\right] \sim \nu^3 \exp[-B/\nu\beta_0|E_M|], \tag{10.68}$$

and the macroscopic current density J_M as

$$J_M \sim I_1/a^2 \sim \mu^2\nu^3 \exp\left(-\frac{B}{\nu\beta_0|E_M|}\right). \tag{10.69}$$

The depolarization factor ν can be written in the form

$$\nu = 1 - d_3\mu^3 + d_5\mu^5 + O(\mu^6), \tag{10.70}$$

where d_3 and d_5 have meanings found by comparing (10.55) with (10.70). It is then not difficult to show that when $\Delta = (1\text{–}\nu) \ll 1$ then J_M goes as

$$J_M \sim \mu^2\{1 - D(d_3\mu^3 - d_5\mu^5)\} + O(\mu^8), \tag{10.71}$$

where

$$D = \frac{B}{\beta_0|E_M|} + 3. \tag{10.72}$$

As noted above, $D \gg 1$ in normal FE situations. Having differentiated (10.71) with respect to μ, equated the expression obtained to zero, and taken away the trivial root of $\mu = 0$, we obtain an equation for the optimum value μ_o of μ, namely

$$5d_3\mu_o^3 - 7d_5\mu_o^5 + O(\mu_o^6) = \frac{2}{D}. \tag{10.73}$$

Studies of (10.73) show that it has one root arbitrary close to zero as $D \to \infty$. Other roots are separated from zero for any value of D. Definitely, it is this solution of the problem that is physically sensible, and other roots appeared due to the approximate nature of (10).

If we disregard the higher order terms in μ_o, (10.73) yields a first approximation as

$$\mu_o^{(1)} = \left(\frac{2}{5d_3D}\right)^{1/3}. \tag{10.74}$$

It follows that $O(\mu^6) = O(D^{-2})$, and (10.73) looks like

$$5d_3\mu_o^3 - 7d_5\mu_o^5 = \frac{2}{D} + O(D^{-2}). \tag{10.75}$$

Solution of (10.75) with this accuracy results in the second approximation

$$\mu_{\mathrm{o}}^{(2)} = \left(\frac{2}{5d_3 D}\right)^{1/3} + \frac{14}{75}\frac{d_5}{d_3^2}D^{-1} + O(D^{-1}), \tag{10.76}$$

with

$$d_3 = \frac{2C_3}{3\ln(4h/R_{\mathrm{a}}) - 6}, \tag{10.77}$$

$$d_5 = \frac{6C_5}{5}\left[\left(\ln\frac{4h}{R_{\mathrm{a}}} - 2\right)^{-1} + \left(3\ln\frac{4h}{R_{\mathrm{a}}} - 11\right)^{-1}\right]. \tag{10.78}$$

The procedure described allows us to determine the optimum value of the H/S ratio $\mu = (h\text{–}R_{\mathrm{a}}/2)/a \cong h/a$, for fixed values of the other system parameters, namely h, R_{a}, and E. In the first approximation, the optimum lattice spacing a_{opt} (i.e., the closest distance between two emitters) is given by an expression that follows easily from (10.74) and (10.77):

$$a_{\mathrm{opt}} = h\left[\frac{5C_3 D}{3\ln(4h/R_{\mathrm{a}}) - 6}\right]^{1/3}, \tag{10.79}$$

with D given by (10.72).

Expressions (10.79) and (10.72) show that the optimum cathode-tip packaging depends on the operating point of the emission diode (i.e., on E_{M}): at high operating voltages between the anode and cathode, it is optimal for emitters to be more close-packed. The underlying physical reason is that the curvature of the current–voltage emission-diode dependence decreases as emitter apex field increases, which means that the emission current density becomes less sensitive to a drop in apex field caused by tightening of the emitter-array structure. Expressions (10.76)–(10.78) give the first two terms of the expansion for μ_{o} (which is equivalent to a_{opt}) in terms of the parameter D.

As an example, consider a carbon post-like emitter (with work-function 5 eV) that is assumed to emit according to the Murphy–Good FE equation, and initially suppose that, when operating as a single isolated emitter, the apex field ($\beta_0|E_{\mathrm{M}}|$) is 5 V/nm. For such an emitter, $B = 49.6$ V/nm, $D = 12.9$. For $h/R_{\mathrm{a}} = 500$, this yields $a_{\mathrm{opt}}/h = 1.91$. This finding, derived from the formula found by Egorov and Almazov [41], agrees well with values ("near 2") found later by other authors by using numerical methods (e.g., [53]). For $h/R_{\mathrm{a}} = 500$ and apex field 7 V/nm, the result is the lower value 1.68, as expected from the above discussion. For $h/R_{\mathrm{a}} = 100$ and apex field 5 V/nm, the result is 2.13, demonstrating (as expected from (10.71)) that the optimum spacing is also affected by the value of h/R_{a}.

In general terms, in several applications of the model, the results found by the Egorov and Almazov (1997) analytical model compare well with equivalent results found later by other techniques.

10.4 Materials Science and Experimental Field Emission Properties

The field electron emission (FE) properties of many different carbon-based materials have now been researched. These materials include carbon nanotubes, fibers, foils, fullerenes, diamond-like films, graphene, and variants of these. Carbon fibers have already been investigated in the 1970s (e.g., [60]). Nowadays, a search for new carbon-based materials with stable FE characteristics is under way. This section discusses the FE properties of the most extensively studied materials and of some recently studied materials, drawn from those described above.

10.4.1 Fullerenes

The fullerene sample initially tested was a *bead* of about 3 mm in diameter, chosen because it had an uneven surface that (it was thought) would improve FE properties. But when a relatively high voltage of about 8 kV was applied, no FE pattern was obtained, even after the bead surface had been processed (see Fig. 10.25 a, b). Consequently, there was no current, either. Subsequently, a C_{60} fullerene fragment was selected, on the grounds that the tip should emit. That attempt resulted in quite bright FE patterns (Fig. 10.26) and gave a current–voltage characteristic (Fig. 10.27).

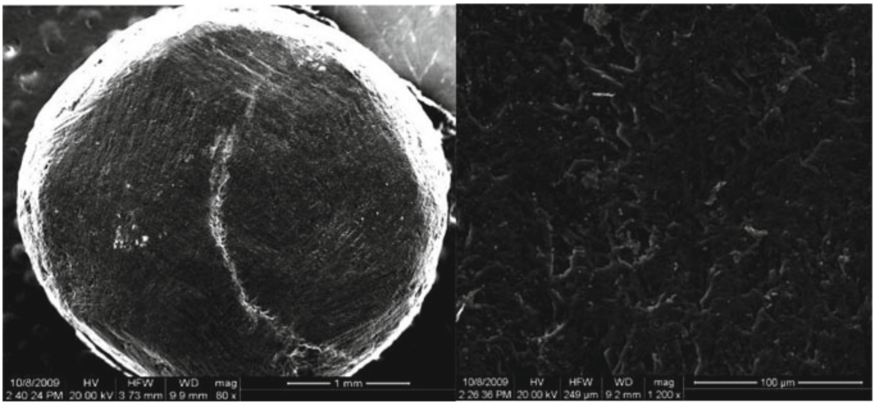

Fig. 10.25 Fullerene specimen prepared as a "bead": (a: left) SEM micrograph, overall view, the length of the white bar is 1 mm; (right) magnified image of surface, length of the bar 100 µm. © 2010 IEEE. Reprinted, with permission, from [61]: V.D. Blank, et al., Proc. 8th International Vacuum Electron Sources Conf. and Nanocarbon, Nanjing, October 2010 (IEEE Explore, 2010), pp. 164–165

Since the cathode-to-anode distance was 1 mm, the onset or threshold field amounted to 4 V/μm, which is quite favorable [61].

As the fullerene FE experiments were only preliminary, that work stage resulted in the conclusion that the material could be used as a FE cathode. However, fullerenes do not make ideal planar FE cathodes, because large parts of their surface areas do not emit.

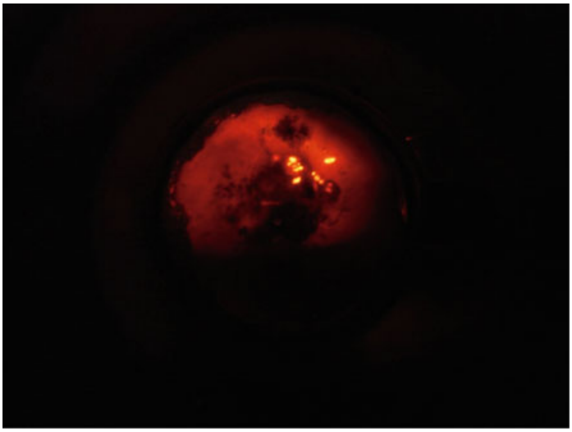

Fig. 10.26 Field electron (emission) microscope image of a C_{60} fullerene fragment

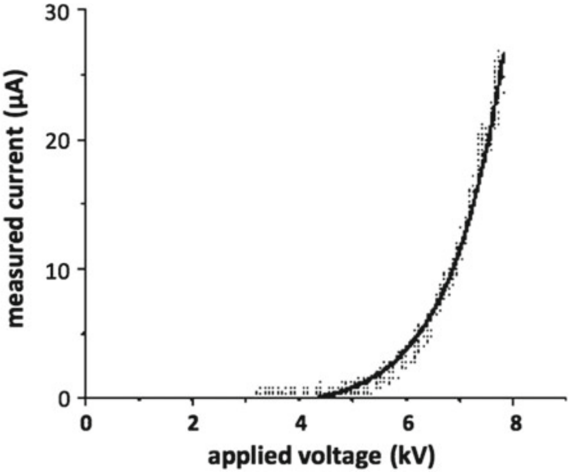

Fig. 10.27 Measured FE current–voltage (I-V) characteristic taken from a C_{60} fullerene fragment

10.4.2 Carbon Nanotubes

The transverse dimensions of nanotubes are extremely small. Therefore, the apex field of a carbon nanotube (CNT) is much higher in magnitude than the average (or "macroscopic") field value in the interelectrode gap. Measurements of the FE characteristics of CNTs mounted perpendicular to the substrate plane are presented in Fig. 10.28. Unfortunately, the current scale is linear and does not extend to the nA range; hence the macroscopic turn-on (onset) field E_{on} cannot be determined from such a plot. This was done by Choi et al. [62], where they measured $E_{\mathrm{on}} = 2$ V/μm for single-walled CNTs (SWCNTs) and $E_{\mathrm{on}} = 2.9$ V/μm for graphite. A. Musatov et al. found, for multi-walled CNTs (MWCNTs grown by CVD), values of E_{on} of 0.7 to 2 V/μm, for nanotube diameters in the range of 20–40 nm [63].

The typical cathode-to-anode distances in test setups of the authors were in the range of 0.4–1 mm. At a voltage of about 500 V, an emitter with a macroscopic area (or "footprint") of about 1 mm^2 generates an emission current of about 0.5 mA; this corresponds to an *average* (or "macroscopic") emission current density (J_{M}) of about 50 mA/cm^2. Since it is known that, during FE, the *local* emission current density (J_{L}) values are typically of the order of 10^3 A/cm^2, it is obvious that only a very small fraction of the total footprint is actually emitting electrons.

This small "emission area" is located near the tips of the CNTs, where the local electric field (E_{loc}) is much higher in magnitude than the mean (or "macroscopic") electric field intensity (E_{M}) between the cathode and the anode. This is

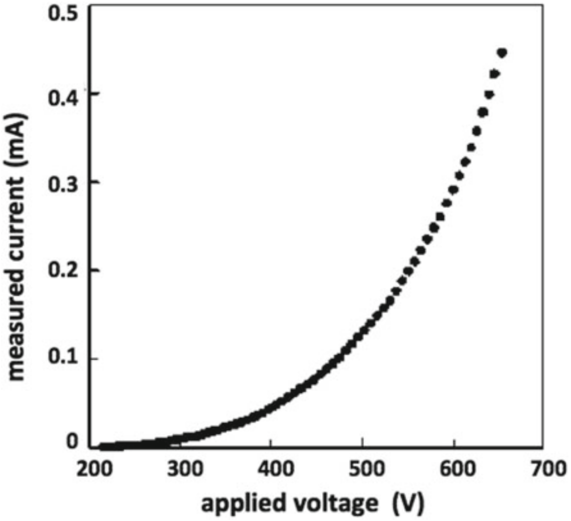

Fig. 10.28 Measured FE current–voltage (I-V) characteristic taken from the film of carbon nanotubes oriented perpendicular to the substrate plane. The macroscopic area (or "footprint") of the film was about 1 mm^2

the well-known physical effect often called *field enhancement*. The related *field-enhancement factor* (FEF) is defined by FEF = $E_{\mathrm{loc}}/E_{\mathrm{M}}$. For carbon nanotubes, FEF-values can sometimes reach a value of 1000 or more (depending primarily on the ratio "height/radius" for the nanotube). This result makes carbon nanotubes (both as single emitters, and as films containing many emitters) quite attractive for application in electronics as cold emitters.

Measurements [64] of total energy distributions (TEDs) found that, at low total emission currents, the TED consisted of separate peaks of about 0.12 eV in width. We ascribe these peaks to emission from particular nanotubes. When the emission current was increased, these peaks broadened and overlapped, but the energy-separation between them remained at the level of 0.1–0.2 eV. One possible explanation is that, with different individual CNTs, the emission is coming from discrete electronic levels that are differently positioned relative to a shared emitter Fermi level.

The same research procedure was applied to look for differences in the FE properties of single-walled (SWCNT) and multi-walled (MWCNT) nanotubes. For the SWCNTs, FE onset occurred at macroscopic fields of 1.6–2 V/μm, and yielded a J_{M}-value of 30 mA/cm^2. The current–voltage characteristic of the process is well described by a Fowler–Nordheim-type expression, which confirms that the emission process is "cold emission" (i.e., Fowler–Nordheim tunneling from states close to the local emitter Fermi level). The maximum achievable value of J_{M} was 3A/cm^2.

For MWCNTs, higher macroscopic-field values are needed in order to cause FE to occur, but the J_{M}-values achieved are nearly the same as for SWCNTs.

By now, there are many reviews relating to field emission from CNTs, as noted in Sect. 10.6. In addition, a particularly useful document is the handbook edited by Saito [65]. Discussion of some particular recent results on CNTs and arrays of bundles of CNTs can be found in Chap. 12.

10.4.3 Pyrographite

Field emission from pyrographite is extremely anisotropic. Its peak value can be obtained from the end-faces of pyrographite plates, but emission is extremely small from the plane faces [66, 67]. Thus, an effective surface for FE cathodes needs to be built from the end-faces of pyrographite plates of varying lengths and thicknesses.

Preliminary experiments showed that pyrographite is quite promising as a field emitter. After that, it became important to determine the optimum temperature of thermal processing and optimum pyrographite plate thickness. To this end, the research focused on the emission characteristics of FE cathodes made with pyrographite plates of 30 μm in thickness processed at 1400 °C, 2000 °C, and 2500 °C, as well as the plates of 5 and 150 μm in thickness processed at 2000 °C and 1700 °C, respectively [67].

The higher the material processing temperature (T_{proc}), the higher was the limiting current achieved. The most likely reason for this was that the material's tensile strength improves with an increase in processing temperature. The FE current fluctuation or instability level (measured as a typical percentage variation in current) was constant for all samples at small currents (about 1–10 μA), but decreased as current increased to higher values (more than 1 mA). At currents of less than 1 μA, the pyrographite FE cathodes of 30 μm in thickness showed the lowest instability value at $T_{\mathrm{proc}} = 2000$ °C and the highest at $T_{\mathrm{proc}} = 2500$ °C. At currents of 3–6 μA, the instability of all samples was 1–2%.

Analysis of FE current fluctuations can provide additional quantitative data on the surface condition. By examining the statistical variance of the current fluctuations, and how this depends on the number of emitting centers, we have been able to conclude that (other things being equal) the cathode with the largest number of the emitting centers is the pyrographite FE cathode of 30 μm in thickness, processed at a temperature of 2000 °C. The number of emission centers per unit area affects the maximum current that can be drawn, the uniformity of FE over the cathode surface, and the cathode lifetime. Thus, we have concluded that pyrographite with these fabrication parameters is the preferred carbon cathode for electronic devices.

10.4.4 Glassy Carbon

In the case of glassy carbon, it did not take long for early experiments to show some specificities of behavior when the emitters were subject to ionic bombardment in intense electric fields. This finding allows the possibility of an in situ emitter formation process.

Edge structures are the easiest to manufacture. They are produced mechanically in a quite simple way. When the effective surface is 10 mm in length, meaning the footprint area is 10^{-4}–10^{-2} cm^2, the forming operation is most effective at currents of more than 1 mA; under these conditions, the emitting surface is rapidly developed. If the forming has not been completed, the emission current can increase, which presumably indicates that the emitting sites continue to get sharper. Correct forming results in emitters with a very stable current–voltage characteristics, both under many-hour operation in high technical vacuum and after holding the FE cathode under air pressure for many days.

However effective the edge-based glassy-carbon cathodes might be, they cannot be used for many applications involving field emission cathodes of relatively large area. At the same time, it should be noted that, in practice, a flat polished surface of glassy carbon cannot function effectively as a FE cathode.

Quite recently, development has begun of another type of a large-area glassy-carbon FE cathode. This is based on reticulated vitreous carbon (RVC) foam, which can easily be cut into blank cathodes of the desired area and configuration [68, 69]. The surface density of micro-elevations able to become emission centers is regulated

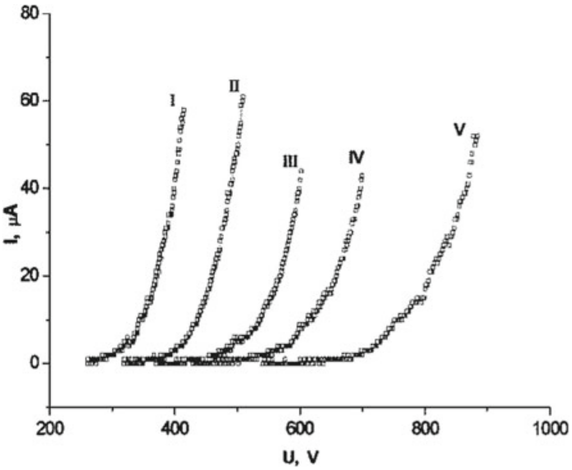

Fig. 10.29 Dynamics of measured current–voltage characteristics, for a large-area glassy carbon cathode, illustrating how the characteristics change gradually (from I to V) as the processing time increases

by the choice of the material volume density, which depends on the details of the configuration of its pores.

Experiments showed that, for large-area glassy-carbon cathodes, the major problems are the same as for many other carbon-based large-area cathodes, namely the achievement of uniform emission from the effective surface of the FE cathode, and achievement of a long service life. Figure 10.29 shows the change of the current–voltage characteristics of an RVC-foam FE cathode with increasing dc current treatment, see [69].

10.4.5 Onion-like Carbon Structures

At the present time, an active search of new materials for FE cathodes continues. Promising new materials include onion-like carbon structures. Only a few experimental investigations of the properties of this material have been described so far, but these suggest that onion-like carbon structures have quite good FE properties. There are different kinds of onion-like structures having different FE properties. When examined in the same experimental test system, the threshold voltage V_{thres} of such powders is less. For example, fullerenes have $V_{\text{thres}} \sim 3$–4 kV, while some powders have $V_{\text{thres}} \sim 0.9$ kV. As yet, we have only managed to obtain some initial data about the FE properties of this powder, i.e., the FE pattern (Fig. 10.30a) and the current–voltage characteristic (Fig. 10.30b).

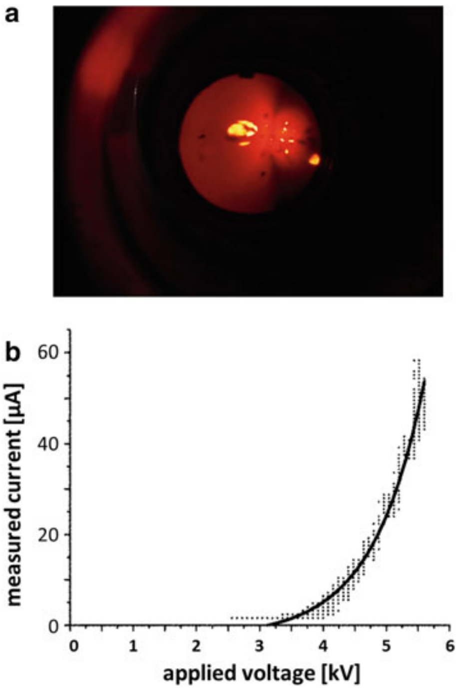

Fig. 10.30 **a** Field electron (emission) microscope image of bulbous carbon structure. **b** Current–voltage (I-V) characteristic taken from bulbous carbon structure

10.4.6 Carbon Fibers

Carbon fibers were first investigated as field emitters in the 1970s (e.g., [60]). In comparison with metallic point FE cathodes, the research showed that carbon-fiber emitters have a longer service life under operation in technical vacuum, partly because they seemed to be "self-healing". Nowadays, it seems promising to make FE cathodes of PAN fibers. Depending on the structure determined by the initial fiber and the thermal processing modes, the PAN-based fibers [12, 70] are superior to both pitch-based carbon fibers and pyrocarbon fibers, in terms of their current-supply capability and their service lifetime. There exists a further variant in the form of milled carbon fibers [71].

When studying the emission properties of PAN fibers, it was found that the current–voltage characteristic plotted in Fowler–Nordheim coordinates has a break in slope (see [12], Fig. 3). The analysis of the FE images made at different emission-current values revealed the irregular nature of the emitting carbon fiber surface [12]; compare Fig. 10.31. Another finding was that increase in applied voltage causes a considerable restructuring of the emission surface as a result of ionic bombardment and Maxwell-stress effects. However, FE cathode characteristics become relatively smooth and stable after a sufficient period of operation. The FE images showed

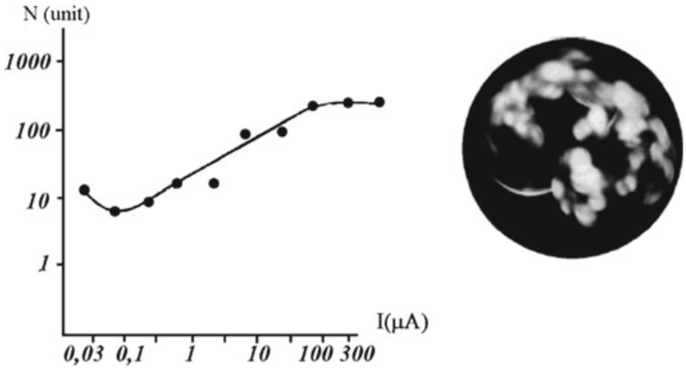

Fig. 10.31 Left: Relation between total current *I* and number *N* of emission centers. Right: Typical field emission microscope image of PAN fiber end (emitting surface). From [12]: E.P. Sheshin, Field emission of carbon fibers, Ultramicroscopy **79**, 101–108 (1999); with permission of Elsevier

stabilization of the FE cathode emission surface, i.e., a considerable growth of the current drawn did not entail any great changes in the emitting-surface structure. These experiments led the authors to conclude that obtaining an effective carbon fiber FE cathode with a stable current–voltage characteristic needs a preliminary formation process. We concluded that, in order to optimize the emitting-surface structure, the FE cathode has to be operated for some time at currents lower than the final working current.

Another important issue is the numerical determination of the emitting-surface area of a fiber. It was suggested above that there is a linear dependence between the emitting-surface area and the total emission current, which is limited to 100–200 μA for one fiber and can be increased in this range by suitable thermal treatment [72]. With a fiber diameter of 7 μm, which is also the diameter of the total emitting area, the theoretical maximum current density is about 520 A/cm^2; but from the field emission microscope (FEM) images, we know that only part of the surface is emitting, with a certain number of emission centers. In Sect. 10.2.2, we have seen that PAN fibers have a sub-micrometer structure consisting of fibrils [3, 12]. In [60], estimations are given of the contribution of emitting fibrils; these also confirm that only part of the fiber end-surface is emitting. In Fig. 10.31, one can see that, at maximum current, about 300 emission centers contributed to the total fiber current, which amounted to about 30% of the fiber end-surface. Since the FEM spots are magnified images of the actual emitting sites, the actual proportion of the surface that is emitting electrons must be significantly smaller. This is consistent with SEM micrographs of the cut fiber end, which show a lot of protrusions and irregularities.

The wide range of emission-current values found by different authors arises mostly from the fact that the parameters of polyacrylonitrile-carbon fibers that determine their emission properties depend on the thermal processing of the fiber. When the limiting FE currents from individual PAN fibers were studied for dependence on processing temperature, it was found out that the limiting current increases with an increase in processing temperature. The FE current that can be drawn from an individual fiber subjected to thermal preprocessing at 2600 °C can reach 190 μA [70, 72].

Field emission from one fiber end is limited to about 200 μA. Hence, for applications requiring higher total current, bundles of fibers have been prepared. Yet, due to field shielding and non-uniformity, the emitted current is also limited to values below 10 mA, regardless of further increase of the number of fibers in the bundle. Therefore, the authors used separate isolated bunches and thus could demonstrate 100 mA of total emission current from 12 bunches [12]. A. Baturin et al. used a bundle 300–600 fibers in their field emission electron gun [73]. Of course, it is also possible to use insulated fibers in a bundle in order to increase the total current. A further possibility especially w.r.t. higher brightness carbon fibers is to sharpen their ends by electro-polishing or etching, in order to get carbon tips. This was realized by Mousa et al. [74]; 24 μA could be drawn from a single tip.

In the context of field screening, some basic experiments have been conducted by Tang et al. in 2016 [75], using a small number of carbon fibers (1 to 9) with height 1.5 mm and inter-fiber separations of between 200 μm and 600 μm. They found that emission is dominated by the fibers at the outer edges, and that the turn-on field increased with the number of fibers. Their conclusion was that, by optimization of the array geometry, field-screening effects can be reduced.

10.4.7 Diamond-like Films

As a result of many experiments, it has been established that the slightest changes in the deposition arrangements for diamond-like films can cause significant changes in the structure of the films obtained. This affects their FE properties. It is also worth mentioning that analysis of the films obtained established that they contain many structural components—which is why diamond-like films are often described together with fullerenes and nanotubes. However, it was well established that the FE properties of diamond-like films are inversely proportional to the mean crystal grain size. For example, a reduction in grain size (mean averaged grain diameter) from 1.3 μm to 0.3 μm reduces the threshold FE voltage and changes the current–voltage characteristics (see Fig. 10.32a). If the grain sizes are the same, the FE current essentially depends on the surface micro-roughness. In particular, a change of grain orientation from (100) to (110) and (111) results in a shift of current–voltage characteristics (see Fig. 10.32b), which is apparently due to an increase in the field-enhancement factor that appears in Fowler–Nordheim-type formulas.

Other often-cited parameters relating to large-area carbon-film structures are “threshold voltage” and the related “threshold macroscopic field“. Threshold values are defined by criteria that involve either the total current or the macroscopic current density reaching a particular level. Criteria relating to macroscopic current density are to be preferred, but several different values are in use. Threshold voltages and threshold macroscopic fields depend on the overall system geometry, but particularly

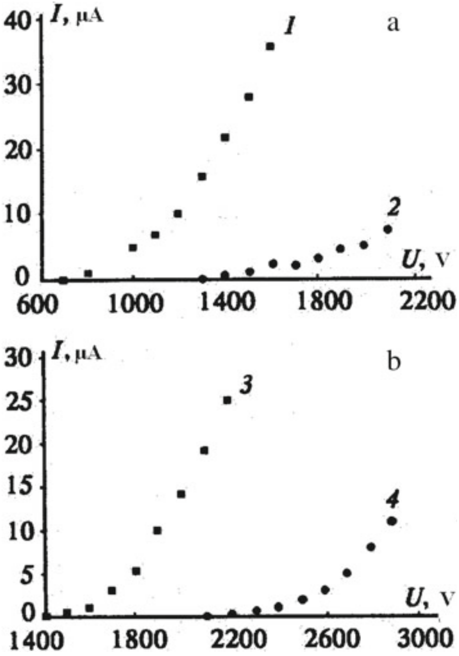

Fig. 10.32 **a** Measured current–voltage (*I-U*) characteristics of diamond-like films, showing their dependence on **a** grain size [1–1.3 μm; 2–0.3 μm]; and **b** grain orientation [3–(100); 4–{(110), (111)}]

on (a) the anode–cathode separation *and* (b) the geometrical structure of the emitter. All of these factors can vary as between different experiments, so care is needed in interpreting the values of threshold parameters. Typical values for the macroscopic current density are around 100 mA/cm^2 (Choi et al. 1997)

A further variant introduced by the authors is to use diamond-carbon nanocomposites as planar field emitters [76]. They consisted of micro-diamond particles embedded in pyrocarbon with 20% nano-diamond prepared by CVD. In order to get a lower turn-on field, the samples were mechanically roughened. Currents of up to 25 μA were achieved.

10.5 Devices and Equipment Employing Carbon-Based FE Cathodes

Recent years have seen FE from nanostructured carbon-based materials applied to provide technical solutions in many types of electronic devices and equipment. Field-electron-emission-based devices can be divided into six basic groups, namely

- light sources
- flat display screens
- X-ray tubes
- electron guns

- microwave devices
- other types of devices, such as ionizers, heaters, and sensors.

We look at these in turn.

10.5.1 Field Emission Light Sources

Basically, existing FE light-source applications can be divided into two main classes (see Fig. 10.33) [77], depending on whether they function in a transmission or a reflection mode.

Generally, the basic classical version is similar to the traditional field electron (emission) microscope. It contains (see Fig. 10.33a) a rod-type FE cathode (1). Such a cathode can be built with any suitable carbon form, such as a graphite rod, a carbon-fiber bunch, or nanostructures at the end face of an appropriate rod. Electrons are extracted with a metal orifice plate that acts as a modulator. (In the literature, this electrode is also called an “extractor” or a “control electrode”, but we prefer the term “modulator”, since one of its primary functions in a light source is to vary the current and control the brightness.)

The cathode-modulator configuration needs to be designed so that three mutually conflicting factors are optimized: one wants to achieve the maximum current transmission through the modulator, the minimum control voltage, and the maximum uniformity of the electron flow impinging onto the inner surface of the light-emitting screen.

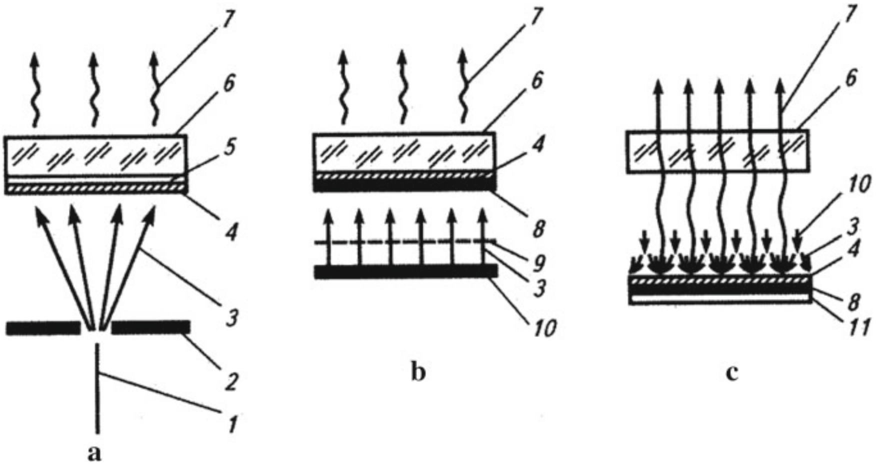

Fig. 10.33 Principles of FE light-source design: a, b—light emitted from the front-plate; c—light emitted by reflection. Design components are 1—field emitter; 2—modulator; 3—flow of electrons; 4—phosphor; 5—transparent conductive coating; 6—output glass; 7—emitted visible light; 8—aluminum coating; 9—grid-modulator; 10—cathode matrix; 11—cathode substrate

The latter is most easily achieved by overlapping the FE flows from a sufficient number of emission centers. This can be achieved by using several rod-type FE cathodes (and related modulator orifices) arranged uniformly in a circle, thus forming a round-section light source.

Classical light sources (see Fig. 10.33a) deposit the light-emitting phosphor onto the back of a transparent conductive coating put onto a glassy front-plate. In such sources, phosphor brightness is not used in full (only about 30% of the photons emitted) because many photons are absorbed by the conductive coating or are emitted backward toward the electron emitter. Better brightness can be obtained if the phosphor and the conductive coating interchange their positions, and the conductive coating is made of aluminum (see Fig. 10.33b). An aluminized coating increases output brightness, raising efficiency to about 70% of the maximum possible value.

Maximum efficiency is achieved when the light source has a "reflection-type" design [78], as shown in Fig. 10.33c. With this design, electrons (3) are emitted toward a luminescent layer (4) deposited onto an aluminum mirror (8) at the "back" of the device. Thus, the light loss is determined primarily by the penetrability of the cathode matrix (10), with relatively small (<10%), light absorption in the glassy front-plate (6).

The particular technological needs of practical applications require the selection of one of these design formats or a variation of it. Various practical FE-based light-source designs are now described.

A so-called "finger-type cathode-luminous tube lamp" is designed to make the brightest light source. It can provide a high-voltage electron flow of up to 10–15 kV with current of up to 1 mA. Such lamps can be more than 100,000 cd/m^2 bright. A schematic diagram of a lamp of this type is shown in Fig. 10.34. The electrons emitted by the FE cathode (1) are driven by the resultant electric field of the modulator (2) and the anode (3) and hit the luminescent screen, thus causing it to glow.

The detailed design of a light source of this type is shown in Fig. 10.35 [79–81]. A vacuum envelope (1) encloses the anode (3, 4), a modulator (5), electrical contact leads (12), and a FE cathode (9) made as a carbon-fiber bunch coated with a dielectric, mostly glassy, over its length. The FE cathode is located in the orifices of alignment disks (8, 10) that have grooves along the perimeter. These grooves tightly hold rods (6), made mostly of glassy, and orienting disks. The centers of the disk orifices are coaxial with the modulator orifice, which is inserted during the assembly of the cathode-modulator unit. The contact arrangements (11) for the FE cathode are made using an electrically conductive substance, usually aquadag, deposited onto

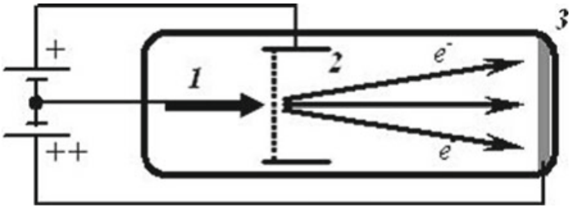

Fig. 10.34 Schematic design of a cathode-luminescence finger lamp: 1—cathode; 2—modulator grid; 3—luminescent anode

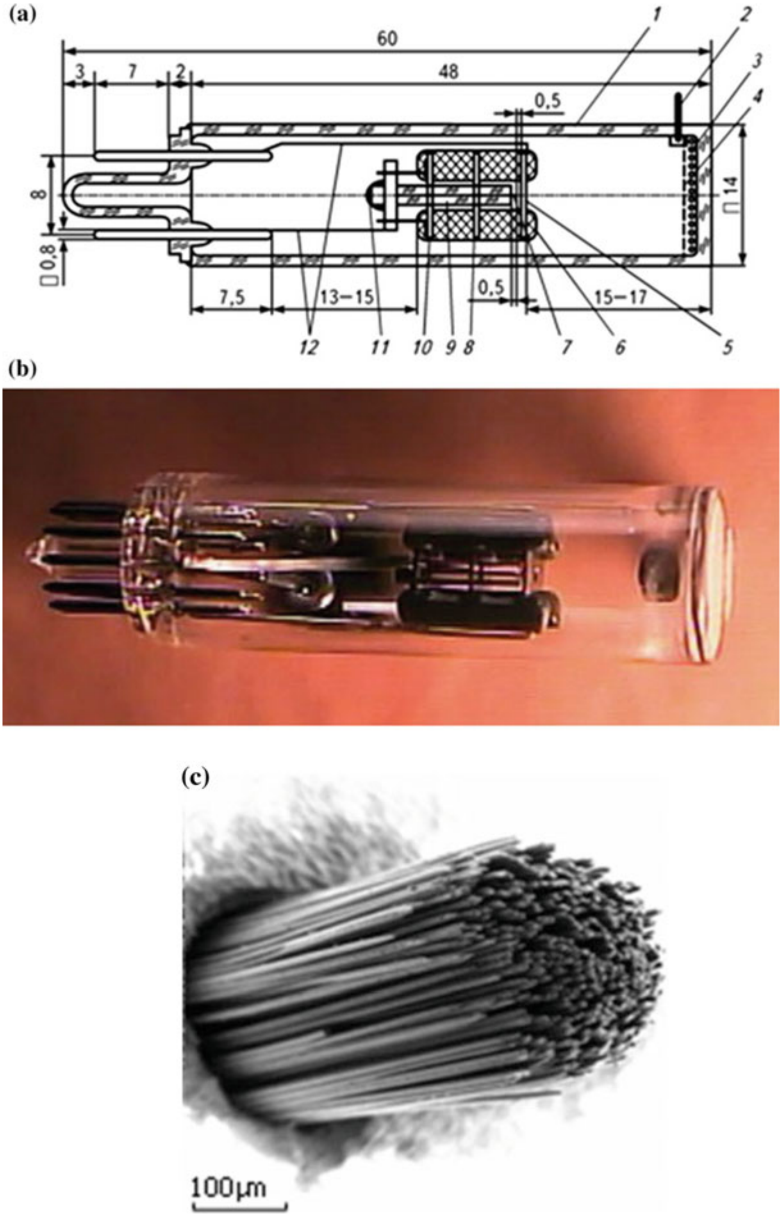

Fig. 10.35 **a** Light source design that uses a carbon-fiber bundle as the FE cathode: 1—vacuum envelope; 2—high-voltage input; 3—phosphor; 4—layer of aluminum; 5—modulator diaphragm; 6—rods; 7—emitting part of bundle of carbon fibers; 8—adjusting disks; 9—vitrified carbon fiber; 10—adjusting disks; 11—electrical contact to fiber; 12—electrical contact leads. **b** Photograph of assembled lamp; see [2], courtesy of Springer. **c** SEM micrograph of the carbon fiber bundle of the FE cathode; see [2], courtesy of Springer

an uncoated part of the fiber bunch. The coating connects the bunch via a lateral surface fixed to the back contact unit of the cathode assembly. The FE cathode itself is a complex multi-point system consisting of 300 PAN fibers bunched together and pre-treated by discharge methods (see Fig. 10.35c).

To increase light-emission power, one has to increase the emission current from the FE cathode. In long-term continuous operation, the current from one carbon-fiber bunch is limited to a value of about 100–150 μA. Thus, further current increase requires that the FE cathode contains several carbon-fiber bunches. In particular, [77, 82] describe a FE cathode with 10 carbon-fiber bunches arranged in a circle. In this case, the lamp dimensions remain very similar to those for the one-bunch FE cathode. Having a large number of fiber bunches in the FE cathode allows the emission current to be increased to about 10 mA. However, such a heavy current can overheat the anode. Another effect is that using a multi-bunch FE cathode improves the uniformity of the screen glow.

As alternatives to carbon fibers, light sources can use other materials as FE cathodes, in particular carbon nanotubes. The designs of such lamps are essentially similar to those shown in Fig. 10.35. Nanotubes are deposited onto flat bases of a few square millimeters in size, either by a CVD method [83] or a print method [84]. Typically, for a cathode-to-modulator-grid separation of 0.2 mm, the control voltage was 300 V. At an anode voltage of 10 kV, the anode current was about 60% of the total emission current of the FE cathode. With an aluminized anode, the brightness of such a source was 6.3×10^4 cd/m^2 for a green phosphor (ZnS:Cu), at an anode current of 200 μA. The efficiency of such a source was 70 lm/W.

The basic structural feature of flat light sources is that the anode and cathode have large areas, but that their separation is small in comparison with the linear dimensions of the cathode substrate. A flat light source has the following components (see Fig. 10.36): a phosphor-coated anode (1); a glass spacer (2), with thickness ranging from some tens of micrometers to a few millimeters; a mounting stub (3); a getter volume (4); a flat FE cathode (5); and a modulator (6), usually implemented by a metal grid.

A well-designed flat-vacuum-device manufacturing technology allows the fabrication of light sources more than 500 cm^2 in area. A device of this kind is built by using diode and triode structures determined by the required device characteristics. Hyper-luminous light sources require a triode structure. Flat light sources of small luminosity, about 1000–5000 cd/m^2, need only a diode structure, which considerably simplifies the manufacture of a vacuum device. In particular, this flat-panel geometry is used in LED-backlit displays.

An early FE-based flat-panel design, shown in Fig. 10.37, is based on carbon-fiber bunches [85–89]. Carbon-fiber bunches (1) are fixed to a metal mounting plate (4). A modulator electrode (2) is located parallel to the emitting plane of the carbon-fiber bunches, at the distance of a few tenths of a millimeter from it. The modulator orifices are coaxial with the emitting ends of the fiber bunches. The cathode (4) and modulator plate (2) are separated by an insulator located inside the vacuum space bounded by glass plates (5) and (7). The upper plate (7) is coated with layers of indium-tin oxide (ITO) of conducting transparent ITO coating (8) and phosphor (6).

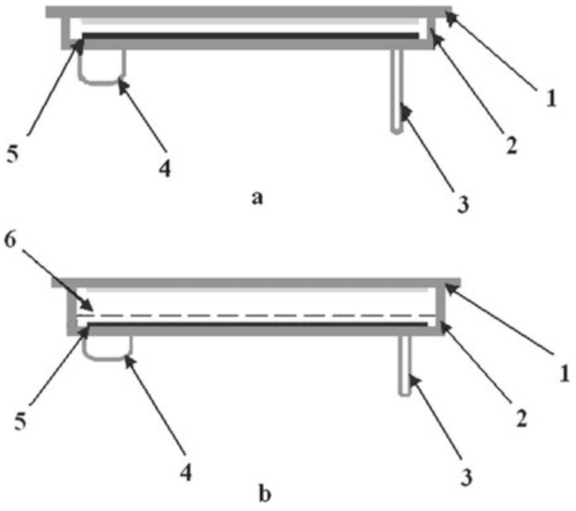

Fig. 10.36 Flat light sources: **a** diode-type design; **b** triode-type design. Design components are 1—anode, coated with phosphor layer; 2—glass spacer; 3—mounting stub; 4—getter volume; 5—flat cathode; 6—modulator grid

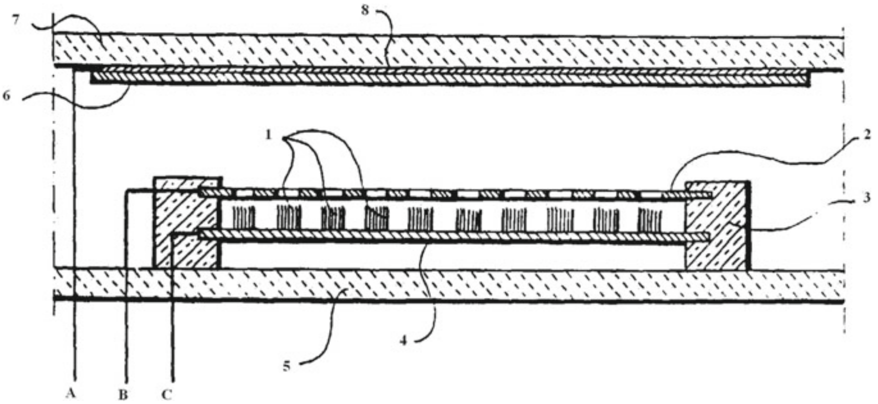

Fig. 10.37 Flat light source built using many bunches of carbon fibers. 1—carbon fiber bunches; 2—modulator with orifices; 3—insulating mounting pillar; 4—metal mounting plate for fiber bunches; 5—glass base-plate; 6—phosphor; 7—glass front-plate; 8—conductive transparent coating

The anode, modulator, and cathode are connected from the outside via electrical leads A, B, and C, respectively.

An alternative to both the above design geometries is to arrange cylindrical components around a central axis, in accordance with the conceptual design shown in Fig. 10.38. This form of design employs a cathode based on fibers, nanotubes, or other FE materials. A cylindrical design has an important electrostatic advantage over

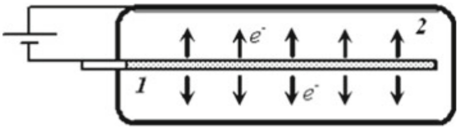

Fig. 10.38 Design of an axial light source: 1—the central part of the cathode structure; 2—cylindrical anode with luminescent coating

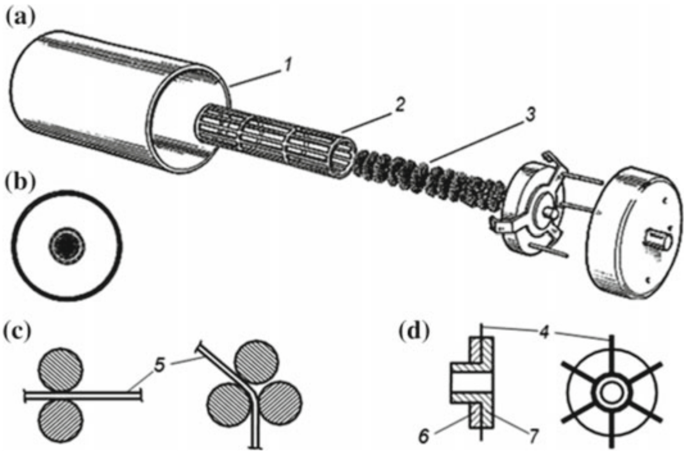

Fig. 10.39 A cylindrical light source that uses carbon-fiber bunches as the FE cathode: **a** to illustrate overall design; **b** cross-section; **c** details of cathode design; **d** cathode design with a radial arrangement of carbon fiber bunches. Components: 1—anode cylinder coated with conductive and luminescent layers; 2—cylindrical modulator mesh; 3—cylindrical-brush-type FE cathode; 4—carbon-fiber bunches; 5—electrical contact wire; 6—clamping disk; 7—mounting disk that holds fiber bunches in place

a planar design, because (for a given anode–cathode separation) the anode–cathode voltage V produces (at the cathode surface) a higher field than in the planar case. (For cylindrical geometry, the magnitude F_{M} of the macroscopic cathode surface is related to V by $F_{\mathrm{M}} = V/r\ln\{R/r\}$, where R and r are the radii of the anode and the cathode, respectively.) Consequently, it is possible to use a diode light-source structure, which is considerably cheaper in manufacturing than the triode structure, though this is not always done.

A cylindrical triode-based light source with FE cathodes made from carbon-fiber bunches is shown in Fig. 10.39 [90–92]. On the outside is an anode screen (1), i.e., a cylinder-shaped glass base coated with a conductive coating with a phosphor layer. The modulator (2) is a cylindrical metal grid or metal etched-foil. The FE cathode (3) is built from carbon fibers. There are two main types of cylindrical FE cathodes. The first has carbon fibers (4) fixed between two or three twisted wires (5), to form a *brush*-type structure. The structure is very easy to manufacture, but the deformation of the carbon fibers can cause them to break and be removed from the cathode by electrostatic forces. Moreover, it is very difficult to maintain a constant height for the FE cathode fibers, and thus constant spacing between the fiber tips and the modulator.

In the second version of the FE cathode structure (Fig. 10.39d), carbon fibers were fixed with a conducting glue or soldered between two disks (6) and (7) made from a conducting material. The assembled disk-modules are then fitted onto a bearing rod of the desired length. This structure provides a more accurate coaxiality of the FE cathode and the modulator, as well as higher structural efficiency. All these factors both improve the uniformity of the FE current over the surface of the FE cathode and reduce the likelihood of unintended electrical bridging of the cathode-modulator gap, either by direct contact or by vacuum breakdown.

Many papers [93–97] are dedicated to the classical diode structure, where the FE cathode function is performed by either a tungsten wire or a metal rod of 2 mm in diameter coated with carbon nanotubes. In all these papers, the rod length was between 3–10 cm, and the diameter between 15 and 30 mm. The nanotubes were deposited in tubular reactors made of quartz tubes 680–850 °C, within a deposition time of 10–30 min. The brightness achieved was about 10,000 cd/m^2 at the anode voltage of 5.4 kV [93].

The efficiency of all the above lamps depends significantly on the nature of the phosphor and on the applied voltage. For equivalent conditions, the luminous efficacy is 21 lm/W for a white phosphor and 37 lm/W for a green one [96]. Some efficiency improvement can be achieved by changing the anode structure [98, 99].

Another approach to the development of cylindrical light sources was proposed in [100, 101]. The diagram of such a source and the photo of its working model are presented in Fig. 10.40. The light source is a glass tube of 15–20 mm in diameter and 20–30 cm in length coated on the inside with phosphor. Cathode + modulator units, of the same design as in finger lamps, are welded into the end-faces of the tube. The anode lead-in wire is soldered into the middle of the tube, and supplied with the accelerating voltage of 10–15 kV. The electrons emitted by the FE cathodes knock out secondary electrons on their way to the anode. As a result, the lamp glow uniformity considerably increases and its efficiency improves. Experimental prototypes show a luminous efficacy of more than 20 lm/W, the rise time (turn-on time) being less than 0.1 ms.

An example of the above approach is a full-color video screen model (see Fig. 10.41) intended for shared use. This module has its own power unit and control system, so only needs a mains supply and computer control inputs [99–101]. Structurally, the module is a complete sign space containing $8 \times 8 = 64$ full-color pixels. Each pixel consists of three lamps of red, blue, and green, making a total of 192. The colors are mixed by pulse-width modulation of the emission current. The unit structure allows the construction of a panel of any size, without loss of screen resolution. The power requirement when all the lamps are "on" simultaneously is about 200 W.

The successful design and manufacture of this module show that it is possible to meet a major challenge associated with FE sources, namely uniformity of their emission characteristics [102] in mass production.

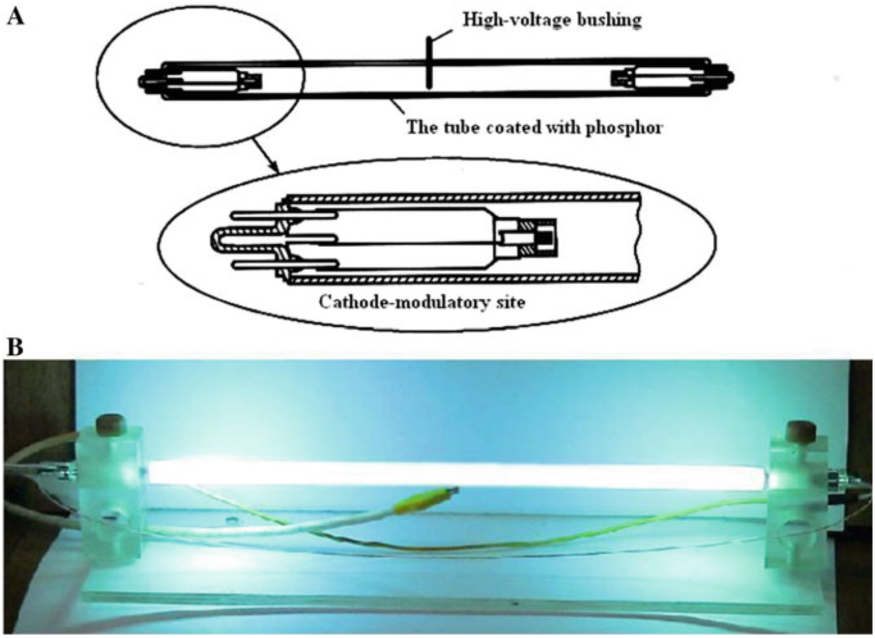

Fig. 10.40 Cylindrical light source with FE cathodes mounted at cylinder ends: **A** design of the source; **B** photograph of a working prototype

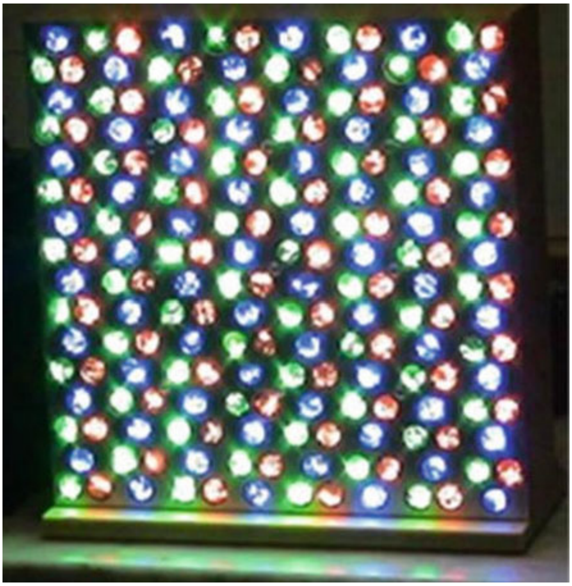

Fig. 10.41 The external module of the full-color video module: 8 by 8 pixels (192) lamp

10.5.2 Flat Display Screens

The world of today is in need of different video-information display devices. The requirements on such devices are also becoming increasingly stricter, because modern displays need to be compact, flat and scalable, reliable, cheap, economical, provide good color rendition and image sharpness over a wide viewing angle, and should have high resolution. Until 2006, which was the turning point in market share, there were three display types in service: liquid-crystal displays (LCDs), plasma-panel displays, and conventional electron-beam displays (= cathode ray tubes or CRTs). Electron-beam displays are ergonomic, have the best color rendition and image sharpness, but are cumbersome and uneconomical w.r.t. large screen sizes and ultra-high resolution. Liquid-crystal monitors are compact and economical, but had a number of problems with image quality; these have now been solved, and also their prices for an increase in dimensions have become competitive. Plasma panels are expensive, have a high power consumption, and are short-lived in comparison with other displays.

None of the three technologies met all the necessary requirements before 2006 (compare Chap. 1). Hence, displays with FE light sources or FE displays had been under development since 1986. Despite that, today in 2020, the race has been won by improved flat thin-film-transistor LC displays (TFT-LCD, light-emitting diode (LED) technology (e.g., [103]) and the new upcoming organic-LED (OLED) display technology (e.g., [104]). Nevertheless, it is instructive in this handbook, to study the technical solutions achieved with field emission displays (FEDs). FEDs were the vacuum electronic (VE) approach to replace the CRT, since they were flat and scalable and had the promise of high resolution. It should be mentioned that there were also other flat VE concepts using thermionic cathodes, pn emitters, or secondary electrons (compare Chap. 1). FEDs can be seen as a form of electron beam display, but with a different electron emission technology. Because FE is a tunneling phenomenon and does not involve emitter heating, it is a highly efficient process in energy terms, and its use can be extremely economical.

As noted above, a FE display pixel is a set of three subpixels, that are implemented as FE diodes or triodes, or as four-electrode FE devices. Anode plates are transparent and are coated with phosphors emitting one of three primary colors: red, blue, and green. The key difference between FE displays and conventional electron-beam displays is that the latter have one electron gun for all the pixels, while the display screens with FE cathodes have an individual electron gun for each subpixel. Such an approach does not involve any cumbersome focusing systems like those in electron-beam displays, and allows the display to be compact and comparable in thickness with liquid-crystal displays. This made the technology of flat display screens based on FE cathodes look very promising for the development of a perfect flat screen [105].

By around 2009 only Futaba and (in earlier years) PixTech had manufactured FEDs for commercial applications. Their displays were competitive at that time, but expensive and only produced in small quantities for special purposes. Later, AU

Optronics from Taiwan bought the FED assets from Sony, but—despite an announcement in 2011—did not start mass production of FEDs. It is still the status today that no company is manufacturing commercial FEDs, and this situation is perhaps unlikely to change.

As a further alternative, Surface-Conduction-Electron-Emitter-Displays were developed as prototypes by Sony, but all activities stopped in 2007.

Difficulties in FED development have related both to inadequacies in available emitter materials and to weaknesses in the structural concepts behind FED design. Modern achievements in electronics allow the development of control circuitry for arrays of FE cathodes, so investigations focused on the FE cathodes themselves and the materials to be used in them. There were two main issues: the development of new phosphors with better efficiency and longer life and the search for new emission materials.

In terms of internal arrangement, FEDs fall into several groups: a classification is shown in Fig. 10.42 [105]. Each structure solves some particular problem, but none solves all of them. The main structure types are described below, with particular examples.

The diode structures provide the simplest and cheapest flat display screens—which is why their development attracted great attention. Especially active attempts to develop such screens started with the application of screen-printing techniques and the electrophoresis method of producing FE cathodes. With the screen-printing technique, it was possible to produce monochrome [106, 107] and color [108, 109] display screens ranging from 4 to 9 inches in size.

Despite their simplicity, diode screens generally have low screen brightness because of a need to keep control voltages relatively low. That is why the greatest efforts have been focused on the development of triode-structure display screens. One section does not provide enough space to cover the whole range of the structures suggested. So we need to specialize our study by describing particular structures that illustrate different design approaches.

One past approach [110] used graphite powder to form FE cathodes that operated at relatively low extraction voltages, around 100 V. The graphite powder, containing

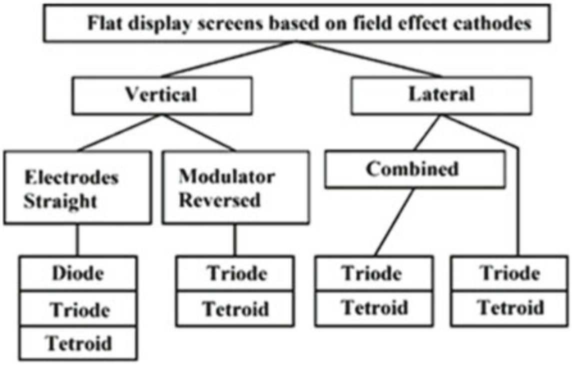

Fig. 10.42 Classification of different designs for "Field Emission Displays" (FEDs), i.e., for flat electronic displays based on field emission cathodes

particles of about 10 μm in size (or average diameter), was mixed with an organic binder to a paste-like state. The paste was then mechanically pressed into holes formed in a glass plate. The holes were made in photosensitive glass, approximately 1.5 mm thick, using ultraviolet photolithography. The holes have a diameter of 200–250 μm at their entrances, but reduce to a diameter of about 100 μm inside the glass, and were spaced 0.6–1.5 mm apart. After the paste had dried, the structure was annealed at a temperature close to the glass softening temperature, to remove the organic binder. Protruding graphite material was removed by mechanical abrasion and polishing. In this design, the modulator was shaped by molybdenum deposition on the structure obtained, with subsequent explosive etching. This resulted in a self-consistent alignment of the FE cathodes and the modulator orifices. The distance between the edges of the graphite cathode and the modulator was about 3–5 μm. The anode used had a usual structure of ITO layers and a phosphor.

The structure of a unit of this design is shown in Fig. 10.43. Contact to the emitter is made via a contact on the back-side of the glass emitter plate. As usual, the anode is coated first with an ITO layer, and then a phosphor layer. The modulator voltage used was 20–50 V; the anode voltage was about 1000–1500 V.

A specific feature of this structure is that FE takes place from the parts of the graphite inserts where the electrostatic field magnitude is highest, which is at the quasi-circular top edges of the inserts. That is why each light spot on the anode is a roughly circular ring [110], formed by a quasi-conical electron beam with a divergence half-angle of 30°–45°. To avoid overlapping the beams from adjacent emitters, the distance between adjacent emitters needs to be greater than the cathode–anode separation.

Naturally, the introduction of each additional electrode into the device structure pushes up the cost. However, the obtained or desired improvement of image brilliance, brightness, and sharpness often more than compensates for the additional costs. Many designs introduce an additional electrode between the modulator and the anode, with orifices coaxial with those in the modulator. This fourth electrode is designed

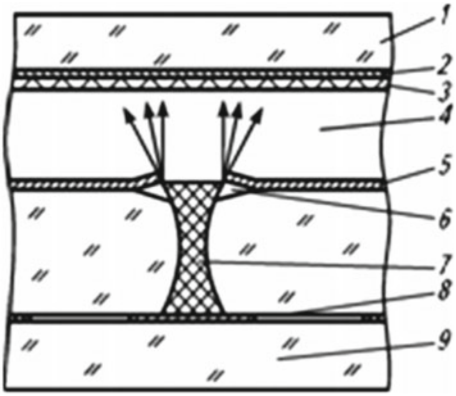

Fig. 10.43 Design of an element of a flat display made using graphite powder: 1—output window; 2—ITO layer; 3—phosphor; 4—flow of electrons; 5—molybdenum modulator; 6—cavity in the glass; 7—graphite cathode; 8—cathode contact; 9—back wall

to overcome the natural divergence of the electron beam from a field emitter, by focusing the beam to produce a smaller spot on the anode [111, 112].

The best results can be obtained by focusing on a so-called "quadrode system" [113]. This includes three apertures formed by structural components of the cathode plate. The focusing electrode can be used not only for its intended purpose, i.e., focusing, but also to protect the FE cathode from discharges [114]. In this case, the aperture of the focusing electrode is smaller than that of the modulator; thus, it is not only focusing that is possible, but also interception of some electrons by the focusing electrode.

The position of the modulator behind the FE cathode under an insulator layer sets this design apart from others. In particular, it eliminates the possibility of vacuum breakdown between the FE cathode and the modulator.

One of the first designs of this type was presented in [115–117]. Figure 10.44a shows the arrangement of the cathode part of the device, while Fig. 10.44b shows the distribution of electrostatic potential and typical electron paths in this kind of cathode-modulator unit. In this design, the glass substrate (1) is coated with an aluminum layer of thickness 150 nm, and then a standard photolithographic process produces modulator electrodes (2) of 400 μm in width. An insulating layer (3) comes next, which in this design is a polyimide layer of thickness 13 μm. Electron-beam vaporization is used to coat this with an aluminum cathode layer (4), and the cathode layer is then developed into cathode bars of width 390 μm. Using a metal grid with a mesh of 20 μm, the cathode bars are then smeared with a paste containing single-walled carbon nanotubes. Subsequent thermal treatment at 350 °C enables the nanotubes to project above the surface of the FE cathode coating, due to the annealing of the binder.

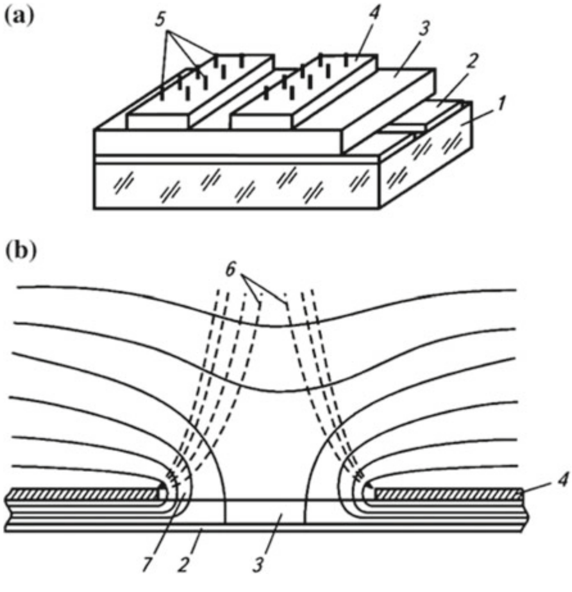

Fig. 10.44 Design of a light source with buried modulator: **a** overall view; **b** to show the distribution of electrostatic potential and trajectories of the emitted electrons. Components: 1—glass substrate; 2—modulator; 3—insulating layer; 4—cathode plate; 5—carbon nanotubes; 6—trajectories of electrons; 7—distribution of electrostatic field; see [2], courtesy of Springer

Figure 10.44b shows the expected distribution of electrostatic potential and expected electron paths, for different modulator voltages. The diagram shows that the electrostatic field is highest in magnitude at the cathode edges, which causes most electron emission to come from the cathode edges, rather than its central part. This effect can be minimized by reducing the width of the cathode units [118].

10.5.3 Microwave Devices

The efficiency of microwave devices needs improvement, and so does their speed-in-action. Microwave-device *heat* power is nearly the same as or even exceeds their *high-voltage* power. In addition, the weight and dimensions of microwave heat sources are comparable with or even exceed the weight and dimensions of high-voltage sources. Reduction of these parameters is especially important for independent and portable radio transmitters. The use of FE cathodes removes all the *heat* problems connected with power-supply sources.

The above comments can be illustrated by the start-up procedure for magnetrons. Magnetrons can be started by *injection*, into the interaction space, of an initial electron current much lower than that of a magnetron in the operating mode. Until now, only thermionic cathodes providing the necessary initial current of several mA have been used for this purpose. Usually, they are effective hot cathodes with an emission current density of 10^4–10^5 A/m^2.

For a FE cathode to start a magnetron, a magnetron reflector is replaced with a disk FE cathode. When anode voltage is applied, the end face of the FE cathode generates a strong electrostatic field that causes FE current. These primary field electrons, driven by the magnetic field, bombard the basic cathode of the magnetron and cause secondary electron emission, thus providing the necessary current for the magnetron in its operating mode.

The magnetron starts almost *immediately*. The start time is determined by an impulse formation time and is less than a micro-second. When hot cathodes are used, the time required for this type of magnetron to reach full operation is 150–180 s from the moment that cathode heating is started. Naturally, FE cathodes do not consume *heating* power, whereas the heating power for the hot cathode needed to start a magnetron amounts to tens of watts.

The first magnetron structures were disk edge FE cathodes. However, more recent magnetron structures employ disk film FE cathodes [119]. The design of such a magnetron is shown in Fig. 10.45. The guide core (1) carries various components. Secondary electron emitters (2) are made from tungsten impregnated with barium, or from alloys and compounds based on platinum-group metals (such as platinum, palladium, iridium, and osmium) combined with an alkaline-earth or rare-earth element (typically Ba, Ir, Ca, La). Between these emitters, there are field emitters (3) that project above them by 5–20% of the interelectrode gap. The field emitters are shaped as beads and consist of a conducting film, with dielectric films (4) protecting the sides.

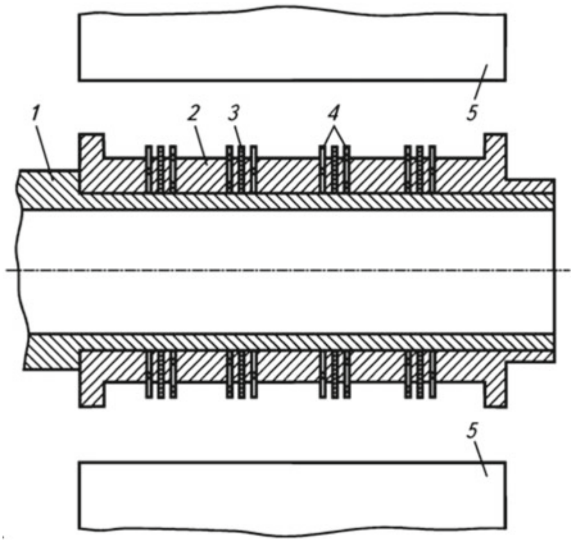

Fig. 10.45 Design of magnetron with disk film FE cathodes: 1—guide core; 2—secondary electron emitters; 3—FE cathode disks; 4—protective dielectric films; 5—cylindrical anode; see [2], courtesy of Springer

The dielectric film protects the lateral surfaces of the field emitter not only mechanically, but also electrically, i.e., when treated with positive ions, it becomes charged to a homogeneous potential that generates a field that repels inbound ions.

10.5.4 X-Ray Tubes

X-ray tubes, requiring high voltage to function, are an obvious application for FE cathodes. Attempts to develop FE-based X-ray technology have been in progress for a long time [120], but by 1975, it was being proposed [121] that the FE cathode be made of differently configured graphite fragments.

Nowadays, we can see intensive development in the field of miniature "through-target" X-ray tubes. A design for such a tube, with a FE cathode made from a carbon-fiber bunch, was suggested in [122] and is shown in Fig. 10.46. The main components in the glass vacuum envelope (1) are an electron gun (2), an anode (3), shaped as a chamber in this case, and the X-ray ejection window (4). The electron gun comprises a FE cathode (5); a modulator (or "cap") (6), with an orifice (12), and with a related electrical lead (7); a dielectric disk (8) that acts as an electrical insulator; and the FE cathode connector assembly (9).

The carbon fiber bunch (10) is mounted in a casing (11), in order to maintain the orientation of the carbon fibers, facilitate their mechanical mounting, and inhibit vibration. The casing can be made from a conducting material or from a semiconducting material such as a semiconducting glass or a metal-coated dielectric, and must be designed in such a way that it firmly grips the carbon-fiber bunch and prevents

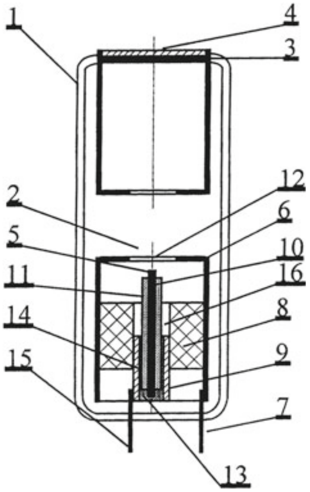

Fig. 10.46 Miniature X-ray tube with "shoot-through" anode and carbon-fiber FE cathode: 1—glass vacuum envelope; 2—electron gun; 3—anode; 4—window; 5—FE cathode; 6—modulator; 7 and15—electrical feedthroughs; 8—dielectric disc; 9—electrical contact for FE cathode; 10—carbon-fiber bunch; 11—casing on fiber bunch; 12—orifice in modulator; 13—electro-conductive paste; 14—metal feed well; 16—protective cavity

movement of the bunch relative to the casing when the tube is in operation. The carbon-fiber bunch (10) projects above the casing (11) on the emitter side.

The X-ray tube functions in the following way. The voltage applied between the cap and the end-faces of the carbon fibers projecting above the casing controls the field acting on the carbon-fiber emitters, and hence the FE current and the X-ray intensity. The high voltage applied between the anode (3) and the cathode (5) accelerates the electrons. X-rays are produced when the electrons bombard the anode, and a fraction of these travel through the anode and glass envelope to emerge from the device.

Numerous fibrils, which in this case are tetragonal crystalline carbon structures, about 25–100 nm in length and 2–5 nm in diameter, oriented along the fiber axis, project above the end-surface of the carbon fiber. These projecting fibrils are the carbon-fiber FE centers. The stop-down orifice (12) in the cap (6) permits field-emitted electrons to travel only to the anode (3) and prevents electrons from hitting the glass walls of the vacuum envelope.

10.5.5 Electron Guns

One of the basic units of an electron-beam tube is the "electron gun“ that generates the electron beam, i.e., a focused electron bunch with the energy and current density necessary for the application. Most guns are designed to produce a round-section beam, but sometimes shaped beams, e.g., ribbon beams, oval-section beams, or other specially shaped beams, need to be generated.

The design requirements for an electron gun can vary widely, depending on the intended application. Thus, the beam electron energy needed is several keV in small oscillographic tubes, but tens or even hundreds of keV in electron microscopes.

Another example is that the beam current of some image pick-up tubes is several tenths of a microampere, while it can reach several milliamperes in lithographic machines. However wide the range of variation of energy and current might be, the beam profile in a particular plane (usually in the receiver plane, i.e., a screen or a target) should normally be as small as possible. The beam profile is usually assessed by the *spot diameter*, a "spot" being understood as the trace of the electron beam on the receiver surface. In many types of contemporary device, the spot diameter is as small as several tenths of a millimeter, or in some applications much less (for example, in high-resolution electron microscopes).

Most guns need to be able to control the beam current over a wide range, from zero, i.e., gun blocking, to a maximum value that depends on the purpose of the beam device. Low-current electron guns are very widely used in electron probe devices, such as focused-beam microscopes and transmission electron microscopes, e.g., those of JEOL [123] or Hitachi.

The first electron gun with a FE cathode was developed by Crewe [124], with aspects of its electron-optical behavior calculated by Butler [125] (see Fig. 10.47). The voltage U_1 applied between the point and the first anode determines the maximum total emission current, but it can be varied up to that limit by variation of U_2. The voltage U_0 determines the electron-beam energy by the further acceleration of the electrons. The electrostatic lens marked as "4" focuses the beam and generates an image spot in the plane of the sample. This design has now been developed further (e.g., [126, 127]).

Fig. 10.47 Schematic design of a FE electron gun: 1—emitter; 2—ion trap; 3—aperture diaphragm; 4—Butler-type accelerating stage; 5—specimen

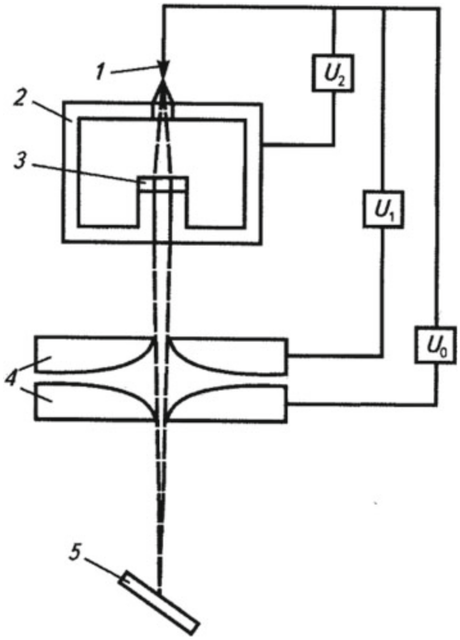

The “camera trap” inlet is 1–2 mm away from the field emitter point. It is supplied with the voltage of 5–8 kV relative to the emitter. The gun works by developing a virtual image of a fictional electron source called the “cross-over” [127]. Swan and Kynastou made a significant advance by suggesting [128] that this virtual source generated by the electron gun could be converted into a real one, by using an additional magnetic condensing lens.

Since the current from one field emitter is very low, the generation of high-ampere currents needs simultaneous operation of many hundreds and thousands of field emitters. The core of this problem has not yet been solved. However, there are continuing attempts to meet the challenge. One approach has been to use arrays of pointed molybdenum FE cathodes (the so-called “Spindt array“, discussed in more detail in Chap. 12). Such arrays employ more than 100,000 individual emitters, but need a working vacuum pressure better than 10^{-7} Pa.

As already pointed out, FE cathodes manufactured from carbon-based materials need less demanding working pressures. In particular, Grigoriev et al. used [129] an array of pointed FE cathodes made of glassy carbon, manufactured by photolithography and thermo-chemical etching. The emitters are 14 μm high and have an apex radius of about 1–3 μm. The emitters stand 20 μm apart. When the cathode-plate diameter is 3 mm, the emission current is of order 100 mA.

In addition, there are cathodes with a large area, usually more than 1 cm^2, that are made with carbon-fiber bunches [73] or high-tenacity graphite, e.g., “Fine-Grained Dense Graphite 6” [130]. These have a high-transmission modulator grid positioned near the cathode plane. This electron-gun design allows the formation of an electron beam with a configuration that depends on the shape and the size of the effective cathode surface.

An example of such a design is shown in Fig. 10.48. The field-electron gun is a

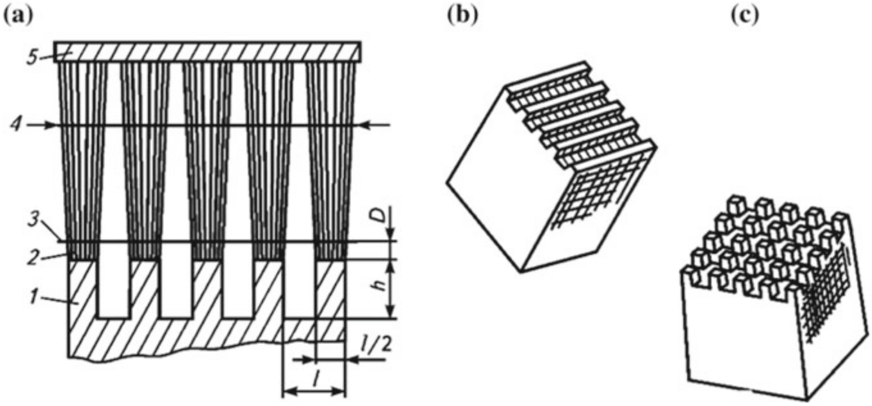

Fig. 10.48 Electron gun with graphite FE cathode: **a** basic design; **b** “bar” form of cathode; **c** matrix form. Components of (**a**): 1—FE cathode built from MPG–6 graphite; 2—working surface of the cathode; 3—modulator, with transparency 80%, built in the form of a grid made using tungsten wire of diameter 0.01 mm; 4—electron beam envelopes; 5—anode

FE cathode (1) with a grooved end-surface (2). In close proximity to the effective surface of the FE cathode, there is an extraction electrode (3) in the form of a grid made from a high-melting-point material. Applying a voltage to the extraction electrode causes FE from the micro-elevations on the effective surface of the cathode. The resulting electron beam, with a configuration that depends on that of the cathode, passes through the extraction electrode and reaches the anode (5), which collects the electrons.

The end-surface of a FE cathode made from nanostructured carbon-based material consists of a great number of micro-elevations, distributed in a statistically uniform fashion over the effective surface. In the course of emission under the bombardment of the surface by residual-gas ions, the emission centers are damaged and at the same time, new micro-elevations are exposed to become new emission centers. After the effective surface of the cathode has aged, this process stabilizes in time. This leads to high time-stability of the emission current drawn from such a cathode.

Increase in the working area of a cathode by more than 4–6 mm^2, intended to increase the cross-section of the emitted beam, can lead to spatial instability of the beam, due to the heterogeneity of a cathode surface of this size. However, a large-cross-section beam can be generated by using a set of separate stable electron beams, each generated by an emitting element that has dimensions comparable with the distance between the cathode and the extraction electrode.

An example of composite field emitter arrays as electron gun cathode from nanocrystalline diamond-like films coated silicon carbide has been developed to improve the electron emission characteristics of the pure silicon carbide tips [131, 132]. The field emission array covered with highly boron-doped diamond film demonstrated the lower turn-on electric field and higher emission current due to lower work function, 1.5 times lower than for undoped one. Both fabricated composite field emission arrays demonstrated high current stability with fluctuations not exceeding 5% at a relatively low vacuum (10^{-5}–10^{-6} Torr). Nevertheless, while the potential of the silicon carbide field emission material is recognized, only a few experimental attempts have been made to fabricate and measure emission characteristics of monolithic silicon carbide field emission arrays [133] and carbon composite structures with silicon carbide, for example, graphene-like structures formed in process of graphitization of silicon carbide surface [134–137].

A final application of interest is that FE cathodes can be used to increase the sensitivity of touch devices, i.e., those responding to even a small change in any physical parameter.

10.6 Conclusions

This chapter has reviewed various carbon-based materials, ranging from long known and well-studied materials to newer materials with much promise for application to FE cathodes and devices based on them. Investigations into the behavior of the best-known materials, operating under various conditions, have been discussed. In order to bring out information about the basic technologies and basic design principles involved, this chapter has looked at many of the historical developments. However, active search has been continuing for new carbon-based materials and viable applications. Since the first review by Bonard [138] in 2001, numerous review articles and book chapters have been published on FE from carbon materials, especially on carbon nanotubes, and related applications. Those who need more detailed information are invited to consult some of these reviews [138–158] and the Saito handbook [65]. Beyond this, further study of the FE properties of carbon-based materials (old and new) should advance the search to identify carbon forms that will progress the development of various types of electronic devices and improve their operating characteristics.

Acknowledgements The authors are grateful to Richard G. Forbes, Konstantin Nikiforov, and Georg Gaertner for critical reading of their manuscript and for valuable suggestions.

The reported study was funded by RFBR, project number 20-07-01086.

References

1. N.V. Egorov, E.P. Sheshin, *Field Emission: Principles and Applications* (Intellekt, 2011) (in Russian)
2. N.V. Egorov, E.P. Sheshin, *Field Emission Electronics* (Springer, 2017)
3. E.P. Sheshin, Properties of carbon materials, especially fibers, for field emitter applications. Appl. Surf. Sci. **215**, 191–200 (2003)
4. B. Rand, Mechanical properties, pp. 111–140 in: *Graphite and Precursors*, ed. by P. Delhaes (Gordon and Breach, Amsterdam, 2001)
5. M. Dubinin, Porous structure and adsorption properties of active carbons, pp. 51–120 in: *Chemistry and Physics of Carbon: A Series of Advances, Vol. 17*, ed. by P. Walker Jr. (Marcel Dekker, New York, 1966)
6. W.A. de Heer et al., Epitaxial graphene. Solid State Commun. **143**, 92–100 (2007)
7. E. Fitzer (ed.), *Carbon Fibers and Composites* (Mir, Moscow, 1988). (in Russian)
8. B.T. Kelly, Present understanding of thermal properties of graphite, High Temp. High Press. **5**, 133–134 (1973)
9. O. Vohler, E. Sperk, Kohlenstoff—Fasermaterial. Berichte der Deutschen Keramischen Gesellschaft **43**, 199–258 (1966). (in German)
10. W. Watt, Production and properties of high modulus carbon fibres. Proc. R. Soc. Lond. **A319**, 5–15 (1970)
11. A.A. Koknin, *Carbon and Other Heat Resistant Fibrous Materials* (Khimiya, Moscow, 1974). (in Russian)
12. E.P. Sheshin, Field emission of carbon fibers. Ultramicroscopy **79**, 101–108 (1999)
13. I.B. Donnet, R.C. Bansal, *Carbon Fibres* (Marcel Dekker, New York, 1990)
14. R.T.K. Baker, P.S. Harris, The formation of filamentous carbon. Chem. Phys. Carbon **14**, 83–165 (1978)
15. A.S. Fialkov, N.M. Sidorov, B.N. Smirnov, B.I. Djuzhikov, Features of the structure and growth of filamentous pyrocarbon formations, Bull. Russ. Acad. Sci. **211/1**, 158–160 (1973) (in Russian)
16. H. Kostka, S. Birkle, N. Kusebauch, Pyrographit—Eigenschaften und Anwendung, Materialwissenschaft und Werkstofftechnik, **22/3**, 92–99 (1989) (in German)

17. A.S. Fialkov, A.I. Baver, N.M. Sidorov, Pyrographite. Production, structure, properties, Uspekhi Khimii **34**, 132–153 (1965). (in Russian)
18. W.F. Knippenberg, B. Lersmacher, H. Lydtin, A.W. Moore, Pyrolytic graphite. Philips Techn. Rev. **28**, 231–242 (1967)
19. P.A. Tesner, *Carbon Production from Gas Phase Hydrocarbons* (Khimaya, Moscow, 1972). (in Russian)
20. V.D. Chekanova, A.S. Fialkov, I.M. Yurkovskiy, Study of structural changes during heat treatment of furfuralphenol-formaldehyde binder. Solid Fuel Chem. **5**, 1037–1040 (1970). (in Russian)
21. A.M. Sigarev, V.K. Bityugin, T.A. Zhuravleva, Properties and structure of glassy carbon. Graphite-Based Constructive Materials **6**, 132–137 (1971). (in Russian)
22. W.F. Knippenberg, B. Lersmacher, Carbon foams. Philips Techn. Rev. **36**, 93–103 (1976)
23. S. Iijima, Helical microtubules of graphitic carbon. Nature **354**, 56–58 (1991)
24. Z.X. Chen, G.C. Cao, Z.L. Lin, I. Koehler, P.K. Bachmann, A self-assembled synthesis of carbon nanotubes for interconnects. Nanotechnology **17**, 1062–1066 (2006)
25. B.V. Deryagin, D.V. Fedoseev, The growth of diamond and graphite from the gas phase (Nauka, 1997) (in Russian)
26. H.W. Kroto, J.R. Heath, S.C. O'Brien, R.F. Kurl, R.E. Smalley, C_{60}: Buckminsterfullerene. Nature **318**, 162–163 (1985)
27. V.G. Pol, S.V. Pol, A. Gedanken, Semiconducting, magnetic or superconducting nanoparticles encapsulated in carbon shells by RAPET method. Carbon Sci. Technol. **1**, 46–56 (2008)
28. S. Chikazumi, S. Taketomi, M. Ukita, M. Mizukami, H. Miyajima, M. Setogawa, Y. Kurihara, Physics of magnetic fluids. J. Magn. Magn. Mater. **65**, 245–251 (1987)
29. S. Mornet, S. Vasseur, F. Grasset, P. Verveka, G. Goglio, A. Demourgues, J. Portier, E. Pollert, E. Duguet, Magnetic nanoparticle design for medical applicaqtions. Prog. Solid State Chem. **34**, 237–247 (2006)
30. M. Leonowicz, M. Wozniak, Y.M. Shulga, V.E. Muradyan, Z. Liu, H.A. Davies, W. nKaszuwara, J. Grabski, Structure and magnetic properties of nanoparticles encapsulated in carbon shells, J. Magn. Magn. Mater. **294**, 57–62 (2005)
31. S.H. Huh, A. Nakajima, Laser synthesis and magnetism of amorphous iron and cobalt carbide nanoparticles with carbon onion. J. Appl. Phys. **99**, 064302 (2006)
32. F. Shoji, Z. Feng, A. Kono, T. Nagai, Spherical carbon particle growth in a methane plasma. Appl. Phys. Lett. **89**, 171504 (2006)
33. T. Hyeon, Chemical synthesis of magnetic nanoparticles. Chem. Commun. **8**, 927–934 (2003)
34. R.H. Fowler, L. Nordheim, Electron emission in intense electric fields. Proc. R. Soc. Lond. A **119**, 173–181 (1928)
35. T.E. Stern, B.S. Gossling, R.H. Fowler, Further studies in the emission of electrons from cold surfaces. Proc. R. Soc. Lond. A **124**, 699–723 (1929)
36. E.L. Murphy, R.H. Good, Thermionic emission, field emission and transition region. Phys. Rev. **102**, 1464–1573 (1956)
37. K.L. Jensen, *Introduction to the Physics of Electron Emission* (Wiley, Chichester, UK, 2018)
38. R.G. Forbes, J.H.B. Deane, Transmission coefficients for the exact triangular barrier: an exact general analytical theory that can replace Fowler & Nordheim's 1928 theory, Proc. R. Soc. Lond. A **467**, 2927–2947 (2011). See electronic supplementary material for definitions of FN constants
39. R.G. Forbes, Field electron emission theory (October 2016), pp. 31–39 in: *Proc. 2016 Young Researchers in Vacuum Micro/Nano Electronics Conf., St Petersburg, October 2016*, ed. by N.V. Egorov and K.A. Nikiforov) (Electronic ISBN 978-1-5090-4605-8) (IEEE Explore, March 2017); arXiv:1801.0825v2
40. A. Modinos, *Field, Thermionic, and Secondary Electron Emission Spectroscopy* (Plenum Press, New York and London, 1984)
41. N.V. Egorov, A.A. Almazov, Optimization of multi-tip field emission electron source. Vacuum **52**, 295–300 (1997)

42. A.N. Tichonov, A.A. Samarskii, *Equations of Mathematical Physics* (Pergamon, Oxford, 1963)
43. D.A. Ovsyannikov, N.V. Egorov *Mathematical Modelling of Systems of Formation of Electron and Ion Beams* (St. Petersburg State University Press, St. Petersburg, 1998) (in Russian)
44. A.A. Almazov, N.V. Egorov, On the method of calculation of field emission systems. Radiotechnika i Electronika **31**, 2452 (1986). (in Russian)
45. R. Gomer, *Field Emission and Field Ionization* (Harvard Univ. Press, Cambridge, Mass., 1961), see p. 32
46. R.G. Forbes, C.J. Edgcombe, U. Valdrè, Some comments on models for field enhancement. Ultramicroscopy **95**, 57–65 (2003)
47. D. Biswas, A universal formula for the field enhancement factor. Phys. Plasma **25**, 043113 (2018)
48. V.A. Zorich, *Mathematical Analysis II* (Springer, Berlin, 2004)
49. F.R. Abbott, J.E. Henderson, The range and validity of the field current equation. Phys. Rev. **56**, 113–118 (1939)
50. G.F. Vasilev, Influence of the shape and potential barrier at the emitter-vacuum interface and distribution of surface electric field on the type of current-voltage characteristics of field emission. Radio Eng. Electron. **5**, 1857–1861 (1960). (in Russian)
51. P.F. Bovey, 100 kV high resolution analytical STEM. Microsc. Spectrosc. Electron. **1**, 507–508 (1976)
52. N.N. Kalitkin, *Numerical Methods* (Nauka, Moscow, 1978). (in Russian)
53. O. Gröning, O.M. Küttel, Ch. Emmenberger, P. Gröning, L. Schlapbach, Field emission properties of carbon nanotubes. J. Vac. Sci. Technol., B **18**, 665–678 (2000)
54. R.G. Forbes, Physical electrostatics of small field emitter arrays/clusters. J. Appl. Phys. **120**, 054302 (2016)
55. H.G. Kosmahl, Analytic evaluation of field emission enhancement factors for ellipsoidal codes and elliptic cross-section wedges. IEEE Trans. Electron Dev. **38**, 1534–1537 (1991)
56. C.J. Edgcombe, U. Valdrè, Microscopy and computational modelling to elucidate the enhancement factor for field electron emitters. J. Microsc. **203**, 188–194 (2001)
57. T.A. de Assis, F.F. Dall'Agnol, Microscopy and computational modelling to elucidate the enhancement factor for field electron emitters. J. Phys.: Condens. Matter **30**, 195301 (2018)
58. R.G. Forbes, Physical explanation of the universal "(separation)$^{-3}$" law found numerically for the electrostatic interaction between two protruding nanostructures, arXiv:1803.031
59. J.R. Harris, K.L. Jensen, D.A. Shiffler, AIP Adv. **5**, 087182 (2015)
60. F.S. Baker, A.R. Osborn, J. Williams, The carbon-fiber field emitter. J. Phys. D Appl. Phys. **7**, 2105–2115 (1974)
61. V.D. Blank, G.A. Dybitsky, E.P. Sheshin, A.L. Shornikova, Field emission properties of fullerenes, Proc. 8th Intern. Vacuum Electron Sources Conf. and Nanocarbon, Nanjing, October 2010 (IEEE Explore, 2010), pp. 164–165
62. W.B. Choi, D.S. Chung, H.Y. Kim. J.H. Kang, J.E. Jun, J.M. Kim. Carbon nanotube based field emission displays, Technical Digest, 12th International Vacuum Microelectronics Conf. July, Darmstadt, Germany, July 1999 (ISBN 3-00-004512-0), pp. 310–311
63. A.L. Musatov, Yu.V. Gulyaev, N.A. Kiselev, E.F. Kukovitsky, A.I. Zhbanov, K.R. Izrael'yants, E.G, Chirkova, A.B. Ormont, A.V, Boykov, Low voltage field electron emitters based on nanotube carbon layers grown by CVD method: experiment and calculations, Proc. 4th International Vacuum Electron Sources Conf., July 2002 (IVESC'02), Saratov, Russia (ISBN: 5-99409-015-4), pp. 81–82
64. V.M. Lobanov, E.P. Sheshin, S.V. Lobanov, Field emission of coherent electrons from carbon nanotubes and fibers, in Proc. 10th International Vacuum Electron Sources Conf. & 2nd International Conf. on Emission Electronics, Saint Peterburg, June-July 2014 (IEEE, Piscataway, 2014) (ISBN: 978-1-4799-5770-5), ed. by N.V. Egorov, pp. 144–145
65. Y. Saito (ed.), *Carbon Nanotube and Related Field Emitters* (Wiley, Weinheim, 2010)

66. S.K. Gordeev, A.M. Lamanov, R.M. Ibragimov, K.N. Nikolskiy, E.P. Sheshin, Pyrolytic carbon cathodes prepared by low temperature vapor deposition, Technical Digest, 18th International Vacuum Nanoelectronics Conf., Oxford, July 2005 (IEEE, Piscataway, 2005) (ISBN: 0-7803-8397-4) pp. 176–177
67. A. Knápek, D. Sobola, P. Tománek, A. Pokorná, M. Urbánek, Field emission from the surface of highly ordered pyrolytic graphite. Appl. Surf. Sci. **395**, 157–161 (2017)
68. A.S. Baturin, E.P. Sheshin, Field emission characteristics of reticulated vitreous carbon, Technical Digest, 13th International Vacuum Microelectronics Conf., Guangzhou, China, August 2000, pp. 42–43
69. A.G. Chakhovskoi, C.E. Hunt, G. Forsberg, R.T. Nilsson, P. Persson, Reticulated vitreous carbon field emission cathodes for light source applications. J. Vac. Sci. Technol., B **21**, 571–575 (2003)
70. E.P. Sheshin, A.V. Anashchenko, S.G. Kuzmenko, Field emission characteristics research of some types of carbon fibers. Ultramicroscopy **79**, 109–114 (1999)
71. E.P. Sheshin, A.S. Baturin, K.N. Nikolskiy, R.G. Tchesov, V.R. Sharov, Field emission cathodes based on milled carbon fibers. Appl. Surf. Sci. **251**, 196–200 (2005)
72. H.W. Aung, E.P. Sheshin, W.Z. Hlaing, N.C. Kyaw, Field emission properties of polyacrylonitrile (PAN) carbon fibers of various processing temperatures, Proc. 2019 International Vacuum Electronics Conf, (IVEC), Busan, South Korea, April-May 2019 (IEEE Explore, 2019)
73. A.S. Baturin, I.N. Yeskin, A.I. Trufanov, N.N. Chadaev, E.P. Sheshin, R.G. Tchesov, Electron gun with field emission cathode of carbon fiber bundle. J. Vac. Sci. Technol., B **21**, 1–4 (2003)
74. M.S. Mousa, M.J. Hagmann, M. Brugat, E.P. Sheshin, Measurements of the self- sustained enhancement of field emission by carbon fiber microemitters. Ultramicroscopy **95**, 119–124 (2003)
75. W.W. Tang, D.A. Shiffler, J.R. Harris, K.L. Jensen, K. Golby, M. LaCour, T. Knowles, Field emission characteristics of a small number of carbon fiber emitters. AIP Adv. **6**, 095007 (2016)
76. N.V. Luparev, E.P. Sheshin, N.N. Chadaev, G.Z. Otarsvili, S.K. Gordeev, S.B. Korchagina, Diamond-carbon nanocomposites as material for cold cathode planar-type emitters, Proc. 8th Intern. Vacuum Electron Sources Conf. and Nanocarbon, Nanjing, October 2010 (IEEE Explore, 2010), pp. 213–214
77. S. Groznov, A. Leychenko, E.P. Sheshin, A. Schuka, Flat displays based on field emission cathodes, "Chipnews", , pp. 21-–25 (2008) (in Russian)
78. E.P. Sheshin, A.L. Suvorov, A.F. Bobkov, D.E. Dolin, Light source on the basis of carbon field electron cathodes: design and parameters, Abstracts of 7th International Vacuum Microelectronics Conf., Grenoble, France, July 1994 (Supplement to "Le Vide, les Couches Minces" No. **271**, Apri11994), pp. 423–426
79. A.S. Baturin, V.S. Kaftanov, S.G. Kuzmenko, E.P. Sheshin, Field electron emission device, Patent RF 2180145, class H01J/28, 15.02.2000
80. MYu. Leshukov, A.S. Baturin, N.N. Chadaev, E.P. Sheshin, Characterizations of light sources with carbon fiber cathodes. Appl. Surf. Sci. **215**, 260–264 (2003)
81. M.Yu. Leshukov, N. N. Chadaev, A. S. Baturin,, E. P. Sheshin, Vacuum cathodoluminescent lamps for information display systems, Proc. Conf. on « Modern Television » , Moscow 2004, pp. 36–38 (in Russian)
82. W. Knapp, O.F. Kieler, D. Schleussner, E.P. Sheshin, I.N. Yeskin, Feldemission von Kohlenstoff-Fasern und deren Anwendung in einem CRT-Lichtelement, Konferenzband Electronic Displays 2000, Berlin, pp. 92–98
83. W. Knapp, D. Schleussner, A.S. Baturin, I.N. Yeskin, E.P. Sheshin, CRT lighting element with carbon field emitters. Vacuum **69**, 339–344 (2003)
84. H. Murakami, M. Hirakawa, C. Tanaka, H. Yamakawa, Field emission from well-aligned, patterned, carbon nanotube emitters. Appl. Phys. Lett. **76**, 1776–1778 (2000)
85. Y. Saito, K. Hamaguchi, R. Mizushima, S. Uemura, T. Nagasako, J. Yotani, T. Shimojo, Field emission from carbon nanotubes and its application to cathode ray tube lighting elements. Appl. Surf. Sci. **146**, 305–311 (1999)

86. V.S. Kaftanov, A.L. Suvorov, E.P. Sheshin, Field emission cathode and methods in the production thereof, US patent No. 5588893, (classification H01J 9/02), appl. 06.06.1995, publ. 31.12.1996
87. V.S. Kaftanov, A.L. Suvorov, E.P. Sheshin, Field emission cathode and methods in the production thereof, US patent No. 5973446, (classification H01J 1/05), 15.02.1999
88. G. Forsberg, C.-H. Andersson, Method of producing a field emission cathode and a light source, Patent. PCT WO 00/77813 A1, 10.06.1999
89. V.S. Kaftanov, A.L. Suvorov, E.P. Shesin, J. Olsfors, Field emission cathode and a light source including a field emission cathode, US patent No. 5877588, 05.03.1999, (H01J 1/30)
90. A.A. Blyabli, A.V. Kandidiov, J.A. Ankelevich, A.A. Pilevskii, A.T. Rakhimov, V.A, Samorodov, Divergence of electrons emitted from a carbon cold cathode, Technical Digest, 12th International Vacuum Microelectronics Conf,, Darmstadt, Germany, July 1999 (ISBN 3-00-004512-0), pp. 346–347
91. J.-M. Bonard, T. Stockli, O. Noury, A. Chatelain, Field emission from cylindrical carbon nanotube cathodes: possibilities for luminescent tubes. Appl. Phys. Lett. **78**, 2775–2777 (2001)
92. X.X. Zhang, C.C. Zhu, X. Li, W.Z. Cui, The fabrication of novel structure of field emitting light tube with carbon nanotubes as cathode, Technical Digest, 18th International Vacuum Nanoelectronics Conf., Oxford, July 2005 (IEEE, Piscataway, 2005) (ISBN: 0-7803-8397-4), pp. 342–343
93. J.X. Huang, J. Chen, S.Z. Deng, J.C. She, N.S. Xu, Optimization of carbon nanotube cathode for a fluorescent lamp, Technical Digest, 18th International Vacuum Nanoelectronics Conf., Oxford, July 2005 (IEEE, Piscataway, 2005) (ISBN: 0-7803-8397-4), pp. 284–285
94. J. Kjellman, M. Lindmark, Light source, and a field emission cathode, US patent 6873095, 29.03.2005, (H01J 1/16)
95. A.N. Obraztsov, A.P. Volkov, A. Zakhidov et al., Field emission characteristics of nanostructured thin film carbon materials. Appl. Surf. Sci. **215**, 214–221 (2003)
96. A.N. Obraztsov, Cathodoluminescent light source, patent appl. US 005/0174059, 11.08.2005 (H01J 63/04)
97. A.S. Leychenko, M.Yu. Leshukov, N.N. Chadaev, E.P. Sheshin, Effective lamp for LCD-backlighting with the field emission cathode, Technical Digest, 19th International Vacuum Nanoelectromics Conf. & 50th International Field Emission Symp., Guilin, China (IEEE, Piscataway, 2006) (ISBN: 1-4244-0410-0), pp. 383–384
98. A.S. Leychenko, M.Yu. Leshukov, N.N. Chadaev, E.P. Sheshin, Field emission backlight for LCD, Proc. Conf. on “Modern Television”, Moscow, 2006, pp. 30–31 (in Russian)
99. P. Liu, Y. Wei, L.M. Sheng, et al., Field emission luminescent light source, US patent appl. 2006/0091782, 04.03.2006 (H01J 63/04)
100. A.I. Trufanov, A.S. Baturin, M.Yu. Leshukov, N.N. Chadaev, E.P. Sheshin, Emission characteristics of a light source with field cathode based on carbon fiber bundle “Microsystem Technics” pp. 32–35 (2004) (in Russian)
101. A.S. Leychenko, M.Yu. Leshukov, E.P. Sheshin, et al. Element of a large video screen with cathodoluminescent light sources as pixels, Proc. Conf. on “Modern Television”, Moscow, 2007, pp. 45–46 (in Russian)
102. A.V. Kudryashov, E.P. Sheshin, N.N. Chadaev, M.M. Kustikov, The element of a big size screen based on light emitters with field emission cathodes, 7th International Vacuum Electron Sources Conf. (IVESC 2008), London, August 2008
103. J. Cho, J.H. Park, J.K. Kim, E.F. Schubert, White light-emitting diodes: History, progress and future. Laser Photonics Rev. **11**, 1600147 (2017)
104. J. Lindén, C. Dam-Hansen, *OLEDs—State of the art report (DTU* (Depatment of Photonics Engineering, Roskilde, 2019)
105. S. Groznov, A. Leychenko, E.P. Sheshin, A. Schuka, Flat display screens based on field electron emission cathodes, “Chipnews”, **7**, pp. 21–25 (2008) (in Russian)
106. K.S. Choi, S.J. Lee, Jae Myung Kim, C.W. Kim, J.W. Nam, J.C. Cha, Y.R. Do, H.G. Yang, Jong Min Kim, FED devices containing a novel graphite cathode prepared by a screen printing process, Technical Digest, 12th International Vacuum Microelectronics Conf., Darmstadt, Germany, July 1999 (ISBN 3-00-004512-0), pp. 32–33

107. K.S. Choi, S.J. Lee, Jae Myung. Kim, C.W. Kim, J.W. Nam, J.C. Cha, Y.R. Do, H.G. Yang, Jong Min Kim, Field emission display devices containing a novel graphite cathode prepared by a screen printing process, SID Symp. Digest of Technical Papers **31(1)**, 671–673 (2000)
108. W.B. Choi, D.S. Chung, J.H. Kang, H.Y. Kim, Y.W. Jin, I.T. Han, Y.H.Lee, J.E. Jung, N.S. Lee. G.S. Park, J.M. Kim, Fully sealed, high-brightness carbon-nanotube field-emission display, Appl. Phys. Lett. **75**, 3129–3131 (1999)
109. J.M. Kim, W.B. Choi, N.S. Lee, J.E. Jung, Field emission from carbon nanotubes for displays. Diam. Relat. Mater. **9**, 1184–1189 (2000)
110. A.Y. Tcherepanov, A.G. Chakhovskoi, V.B. Sharov, Flat panel display prototype using low-voltage carbon field emitters. J. Vac. Sci. Technol., B **13**, 482–486 (1995)
111. N.S. Xu, Z.S. Wu, S.Z. Deng, J. Chen, High-voltage triode flat-panel display using field–emission nanotube-based thin films. J. Vac. Sci. Technol. B **19**, 1370–1372 (2001)
112. T. Yaguchi, T. Muneyoshi, M. Okai, N. Hayashi, T. Nakamura, Flat panel display device, US Patent appl. 2005/0057178, 17.03.2005, (G 09 G 3/10)
113. T. Oh, Field emission display, European Patent 1542258, disclosure 15.06.2005, classif.: H01j 31/12
114. K. Oono, Field emission display device and method of manufacturing same, US Patent appl. US 2004/0239235, 02.12.2004, (H01j 1/62)
115. J.H. Kang, Y.S. Choi, W.B. Choi, N.S. Lee, et al., Under-gate triode type field emission displays with carbon nanotube emitters, Mat. Res. Soc. Symp., Proc. **621**, R5.2.1–R5.2.5 (2000)
116. Y.S. Choi, J.H. Kang, Y.J. Park, W.B. Choi, C.J. Lee, S.H. Jo, C.G. Lee, J.H. You, J.E. Jung, N.S. Lee, J.M. Kim, An under-gate structure field emission display with carbon nanotube emitters. Diam. Relat. Mater. **10**, 1705–1708 (2001)
117. Y.S. Choi, J.H. Kang, H.Y. Kim, B.G. Lee, C.G. Lee, S.K. Kang, Y.W. Jin, J.W. Kim, J.E. Jung, J.M. Kim, A simple structure and fabrication of carbon-nanotube field emission display. Appl. Surf. Sci. **221**, 370–374 (2004)
118. V.P. Mammana, G.E. McGuire, O.A. Shenderova, Back-gated field emission electron source, US patent application 2005/0116214, 02. 06.2005, (H01 L 29/06)
119. V.I. Mahov, B.V. Bondarenko, M.F. Kopyilov, Microwave device of M-Type, Patent of Russian Federation № 2040821, 27.07.1995, classification: H01j 1/30 (in Russian)
120. J.E. Lilienfeld, The autoelectronic discharge and its application to the construction of a new form of X-ray tube. Amer. J. Roentgenology **9**, 172–179 (1922)
121. T. C. Cunningham, Field emission x-ray tube having a graphite fabric cathode, US Patent 3883760, 07.04.1971 (H01J 35/06)
122. E.P. Sheshin, N.N. Chadaev, A.S. Baturin, A.I. Trufanov, X-ray tube with field emission cathode, Patent of Russian Federation No. 8248643, 20.03.2005, classification H01J 35/02 (in Russian)
123. https://www.jeol.de/electronoptics-en/products/transmission-electron-microscopes-tem.php [observed: 12 Feb 2020]
124. A.V. Crewe, Scanning Electron Microscope, US patent No. 3191028, 22.6.1965
125. J.W. Butler, *Digital computer techniques in electron microscopy, 6th Internat* (Kyoto, Japan, Congress on Electron Microscopy, 1966), p. 191
126. M. Okai, K. Hidaka, M. Hayashibara, S. Watanabe, Field emission electron gun and electron beam applied device using the same", US Patent appl. 2008/0029700, 07.02.2008, (H01J 37/073)
127. P.W. Hawkes, E. Kasper, *Principles of Electron Optics, Vol. II: Applied Geometrical Optics* (Academic, London, 1996)
128. D.I. Swan, D. Кynastou, The development of a field emission SEM, Proc. 6th Annual Scanning Electron Microscope Symp., 1973, N1, p. 57
129. Y.A. Grigoriev, A.I. Petrosyan, V.V. Penzyakov, V.G. Pimenov, V.I. Rogovin, V.I. Shesterkin, V.P.Kudryashov. V.C. Semyonov, Experimental study of matrix carbon field-emission cathodes and computer aided design of electron guns for microwave power devices, exploring these cathodes, J. Vac. Sci. Technol. B **15**, 503–506 (1997)

130. B.V. Bondarenko, V.I. Makuha, E.P. Sheshin et al., Field electron emission gun, Certificate of Authorship, USSR Patent 1294188, (H01J 1/30), 11.03.1985 (in Russian)
131. V.A. Golubkov, A.S. Ivanov, V.A. Ilyin, V.V. Luchinin, S.A. Bogdanov, V.V. Chernov, A.L. Vikharev Stabilizing effect of diamond thin film on nanostructured silicon carbide field emission array, J. Vac. Sci. Technol. B **34**, 062202 (2016)
132. O.A. Ivanov, S.A. Bogdanov, A.L. Vikharev, V.V. Luchinin, V.A. Golubkov, A.S. Ivanov, V.A. Ilyin, Emission properties of undoped and boron-doped nanocrystalline diamond films coated silicon carbide field emitter arrays. J. Vac. Sci. Technol. B **36**, 021204 (2018)
133. K. Nikiforov, V. Trofimov, N. Egorov Field emission spectroscopy of silicon carbide: natural modeling, 2015 International Conference on "Stability and Control Processes" in Memory of V.I. Zubov, SCP 2015—Proceedings, 7342085, pp. 180–182 (2015)
134. N.I. Alekseev, V.V. Luchinin, N.A. Charykov, Evaporation of carbon atoms from the open surface of silicon carbide and through graphene cells: Semiempirical quantum-chemical modeling. Russ. J. Phys. Chem. A **87**, 1830–1837 (2013)
135. N.I. Alekseev, V.V. Luchinin, N.A. Charykov, Initial stage of the epitaxial assembly of graphene from silicon carbide and its simulation by semiemprical quantum chemical methods: Carbon face. Russ. J. Phys. Chem. A **87**, 1709–1720 (2013)
136. N.I. Alekseev, V.V. Luchinin, N.A. Charykov Simulating the conditions for the formation of graphene and graphene nanowalls by semiempirical quantum chemical methods, Russ. J. Phys. Chem. A **87**, 1721–1730 (2013)
137. N.I Alekseev, A.A. Kal'nin, D.D. Karmanov, V.V. Luchinin, S.A. Tarasov, N.A. Charykov, Epitaxial assembly of graphene on face (0001) of silicon carbide: Modeling by semi-empirical methods, Russ. J. Phys. Chem. A **87(**1739–1748 (2013)
138. J.-M. Bonard, H. Kind, T. Stöckli, L.-O. Nilsson, Field emission from carbon nanotubes: the first five years. Solid-State Electronics **45**, 893–914 (2001)
139. A. Mayer, N.M. Miskovsky, P.H. Cutler, Theoretical comparison between field-emission properties of carbon protrusions ranging from an isolated atom to multi-wall nanotubes, J.Phys.: Condens. Matter **15**, R177–R191 (2003)
140. N. de Jonge, J.-M. Bonard, Carbon nanotube electron sources and applications. Phil. Trans. R. Soc. Lond. A **363**, 2239–2266 (2004)
141. M.P. Anantram, F. Léonard, Physics of carbon nanotube electronic devices. Rep. Prog. Phys. **69**, 507–561 (2006)
142. F. Le Normand, C.S. Cojocaru, C. Fleaca, J.Q. Li, P. Vincent, G. Pirio, L. Gablof, Y. Nedellec, P. Legagneux, A comparative study of the field emission properties of aligned carbon nanostructures films, from carbon nanotubes to diamond. Eur. Phys. J. Appl. Phys. **38**, 115–127 (2007)
143. A.V. Eletskii, G.S. Bocharov, Emission properties of carbon nanotubes and cathodes on their basis. Plasma Sources Sci. Technol. **18**, 034103 (2009)
144. N. de Jonge, Carbon nanotube electron sources for electron microscopes, Chap. 3 in: Adv. Imaging Electron Phys., Vol. 156 (Elsevier, 2009) pp. 203–233
145. F. Léonard, *The Physics of Carbon Nanotube Devices* (William Andrew, 2009). See Chap. 6
146. A. Zhbanov, E. Pogolerov, Y.-C. Chang, Carbon nanotube field emitters, Book chapter downloadable from: www.intechopen.com (published 2010)
147. T. Zhai, L. Ma, M. Liao, X. Wang, X.-S. Fang, J. Yao, Y. Bando, D. Golberg, One-dimensional inorganic nanostructures: synthesis, field-emission and photodetection. Chem. Soc. Rev. **40**, 2986–3004 (2011)
148. W. Lu, M. Zu, J.-H. Byun, B.-S. Kim, T.-W. Chou, State of the art of carbon nanotube fibers: opportunities and challenges. Adv. Mater. **24**, 1805–1833 (2012)
149. G.S. Bocharov, A.V. Eletskii, Theory of carbon nanotube (CNT)-based electron field emitters. Nanomaterials **3**, 393–442 (2013)
150. A. Nojeh, Carbon nanotube electron sources: from electron beams to energy conversion and optophotonics. ISRN Nanomaterials **2014**, 879827 (2014)
151. G. Mittal, I. Lahiri, Recent progress in nanostructured next-generation field emission devices. J. Phys. D Appl. Phys. **47**, 323001 (2014)

152. Y. Li, Y. Sun, J.T.W. Yeow, Nanotube field electron emission: principles, development, and applications. Nanotechnology **26**, 242001 (2015)
153. R.J. Parmee, C.M. Collins, W.I. Milne, M.T. Cole, X-ray generation using carbon nanotubes. Nano Convergence **2**, 1 (2015)
154. M.T. Cole, M. Mann, K.B.K. Yeo, W.I. Milne, Engineered carbon nanotube field emission devices, Chap. 5 in: *Emerging Nanotechnologies for Manufacturing* (*2nd Edition*), ed. by W. Ahmed, J.M. Jackson (William Andrew, 2015)
155. M.T. Cole, M. Nakamoto, W.I. Milne, Field emission displays (FEDs) and surface-conduction electron-emitter displays (SEDs), in: *Handbook of Digital Imaging* (Wiley, 2015)
156. L. Chen, H. Yu, J. Zhong, L. Song, J. Wu, W. Su, Graphene field emitters: a review of fabrication, characterization and properties. Mater. Sci. Eng. B **220**, 44–58 (2017)
157. F. Giubileo, A. Di Bartolomeo, L. Iemmo, G. Luongo, F. Urban, Field emission from carbon nanostructures. Appl. Sci. **8**, 526 (2018)
158. M. Schulz, V. Shanov, Z.-Z. Yin, M. Cahay (editors) *Nanotube Superfiber Materials*, 2nd Edition, Elsevier, 2019; containing Chap. 21: M. Cahay, K.L. Jensen, R.G. Forbes, et al., Optimising the field-emission properties of carbon nanotube-based fibers; and Chap. 22: W. Zhu, M. Cahay, J. Ludwick, et al., Multiscale modelling of field emission properties of carbon nanotube based fibers